Infrared H2O absorption in massive protostars at high spectral resolution: full spectral survey results of AFGL 2591 and AFGL 2136

Barr, A.G.; Boogert, A.; Li, J.; DeWitt, C.N.; Montiel, E.; Richter, M.J.; ... ; Tielens, A.G.G.M.

The Astrophysical Journal, 935:165 (29pp), 2022 August 20 https://doi.org/10.3847/1538-4357/ac74b8

Infrared H_2O Absorption in Massive Protostars at High Spectral Resolution: Full Spectral Survey Results of AFGL 2591 and AFGL 2136

Andrew G. Barr[1], Adwin Boogert[2], Jialu Li[3], Curtis N. DeWitt[4], Edward Montiel[4], Matthew J. Richter[5], Nick Indriolo[6], Yvonne Pendleton[7], Jean Chiar[8], and Alexander G. G. M. Tielens[1,3]
[1] Leiden University, Niels Bohrweg 2, 2333 CA Leiden, The Netherlands; barr@strw.leidenuniv.nl
[2] Institute for Astronomy, University of Hawaii, 2680 Woodlawn Drive, Honolulu, HI 96822, USA
[3] Astronomy Department, University of Maryland, College Park, MD 20742, USA
[4] USRA, SOFIA, NASA Ames Research Center, MS 232-11, Moffett Field, CA 94035, USA
[5] University of California Davis, Phys 539, Davis, CA 95616, USA
[6] AURA for ESA, Space Telescope Science Institute, Baltimore, MD 21218, USA
[7] NASA Ames Research Center, Moffett Field, CA 94035, USA
[8] Diablo Valley College, 321 Golf Club Road, Pleasant Hill, CA 94523, USA
Received 2021 March 12; revised 2022 May 25; accepted 2022 May 27; published 2022 August 24

Abstract

We have performed a high-resolution 4–13 μm spectral survey of the hot molecular gas associated with the massive protostars AFGL 2591 and AFGL 2136. Here we present the results of the analysis of the ν_2 band of H_2O, detected with the Echelon Cross Echelle Spectrograph on board the Stratospheric Observatory for Infrared Astronomy between wavelengths of 5 and 8 μm. All lines are seen in absorption. Rotation diagrams indicate that the gas is optically thick and lines are observed to saturate at 40% and 15% relative to the continuum for AFGL 2136 and AFGL 2591, respectively. We applied two curve of growth analyses to derive the physical conditions, one assuming a foreground origin and one a circumstellar disk origin. We find temperatures of 400–600 K. A foreground origin would require the presence of externally heated clumps that are smaller than the continuum source. The disk analysis is based on stellar atmosphere theory, which takes into consideration the temperature gradient in the disk. We discuss the challenges with each model, taking into consideration the properties of other species detected in the spectral survey, and conclude that further modeling efforts are required to establish whether the absorption has a disk or foreground origin. The main challenge to the foreground model is that molecules are expected to be observed in emission. The main challenges to the disk model are the midplane heating mechanism and the presence of narrow absorption lines shifted from the systemic velocity.

Unified Astronomy Thesaurus concepts: Star formation (1569); Water vapor (1791); Circumstellar disks (235); Protoplanetary disks (1300); Stellar accretion disks (1579); Chemical abundances (224); Astrochemistry (75)

Supporting material: machine-readable tables

1. Introduction

Water is observed throughout the universe, from diffuse and translucent clouds to dense star-forming regions, shocks, protoplanetary disks and comets, evolved stars, and external galaxies (van Dishoeck et al. 2013). Its importance in the environment of star-forming regions is exhibited by it being one of the most abundant molecules in both the ice and gas phases. In warm regions, due to ice sublimation ($T > 100$ K) and gas-phase chemistry ($T > 250$ K), all of the available oxygen that is not locked up in CO or dust grains is driven into H_2O resulting in a jump in abundance from as low as 10^{-9} with respect to H in the cold envelope, to up to 10^{-4} in the hot gas close to the protostar (Boonman et al. 2003; Boonman & van Dishoeck 2003). It is one of the main carriers of oxygen and is readily detected toward low to high mass protostars; therefore, it is of fundamental importance to studies of star formation.

A massive protostar forms out of a gravitationally unstable core in a dark molecular cloud (Egan et al. 1998; Zinnecker & Yorke 2007). During this process, an accretion disk develops around the protostar through which material from the envelope can be channeled onto the forming star. Due to the high accretion rates, the disk is heated from the midplane by viscous processes (Dullemond et al. 2007; D'Alessio et al. 1998). The disk and protostar at this stage will still be deeply embedded in the parent molecular cloud, and will remain so until after the star reaches the main sequence (Beuther et al. 2007).

Water is very difficult to observe from the ground due to the large quantity of H_2O in the Earth's atmosphere. Ideally, observations would be carried out with space-based facilities, to study H_2O in-depth. This is reflected in the particular success of the Infrared Space Observatory (ISO; Cernicharo & Crovisier 2005) and the Herschel Space Observatory in observing H_2O in all of the astronomical objects previously mentioned (Melnick et al. 2010; Neufeld et al. 2011; Moreno et al. 2012; van der Tak et al. 2013; van Dishoeck et al. 2021). The Stratospheric Observatory for Infrared Astronomy (SOFIA) offers an alternative opportunity for studying H_2O, as it flies above most of the water in the Earth's atmosphere, vastly reducing interference, and allowing for the opportunity to observe hundreds of rovibrational H_2O lines, including low energy lines, and even lines tracing the ground level (Indriolo et al. 2015).

Gas-phase H_2O absorption toward massive protostars has been studied extensively with ISO's short wavelength spectrometer (SWS; van Dishoeck & Helmich 1996; Cernicharo et al. 1997;

van Dishoeck 1998; González-Alfonso et al. 1998; Wright et al. 2000; Boonman & van Dishoeck 2003; Boonman et al. 2003). The cold envelope and warm protostellar environment were distinguished by a *jump* in the H_2O abundance as the temperature transitioned from low to high (Boonman & van Dishoeck 2003; Boonman et al. 2003). The low resolution ($R \sim 1400$) of ISO/SWS, however, meant that the individual rovibrational H_2O transitions blended into each other, creating a single broad absorption feature. The result of this was that physical conditions had to be derived assuming a single absorbing slab model in local thermodynamic equilibrium (LTE) and adopting a simple line profile. Moreover, because of the low spectral resolution, no kinematic information could be obtained.

We have conducted the first full spectral survey of the mid-infrared (mid-IR) wavelength region at high spectral resolution of two massive protostars. Previous papers have focused on the simple organics detected, including HCN, C_2H_2, NH_3, CS, and ^{13}CO (Barr et al. 2018, 2020). All species are seen in absorption. Abundance/column density variations are observed in HCN and C_2H_2 with absorption bands tracing the same lower level exhibiting differences up to a factor of 10. The bands at 13 μm have a lower abundance compared to the bands at 7 μm, for both AFGL 2136 and AFGL 2591. This has been previously observed in Orion IRc2 (Evans et al. 1991) and NGC 7538 IRS1 (Barentine & Lacy 2012). If this absorption was due to foreground gas, this would imply a smaller covering factor of the continuum source at 13 μm compared to 7 μm. Knez et al. (2009) find that absorbing gas is optically thick and lines are saturated toward NGC 7538 IRS1; however, lines do not go to zero flux. They suggest that this could be due to partial covering of the continuum source; however, this is highly uncertain with covering factors ranging from a few percent to 100% across two absorbing components. Evans et al. (1991) proposed that the column density difference with wavelength could be due to larger extinction and continuum size at longer wavelengths, due to a cooler dust component invisible at the shorter wavelengths, which can account for a factor of up to 2 difference.

Here we discuss H_2O in the context of our spectral survey, where the fully resolved H_2O lines allow temperatures and abundances to be derived as well as the study of kinematics in these environments. The details of the survey and analysis techniques are outlined in Sections 2 and 3, respectively. In Section 4, we present the results for the H_2O lines in the contexts of both a foreground absorbing slab and a stellar atmosphere model assuming a disk origin, and in Section 5, we discuss these results elaborating on, and comparing, the two approaches.

2. Observations and Data Reduction

AFGL 2591 and AFGL 2136 were observed with the Echelon Cross Echelle Spectrograph (EXES) spectrometer (Richter et al. 2018) on board the SOFIA flying observatory (Young et al. 2012) as part of SOFIA programs 05_0041 and 06_0117. In this full spectral survey of AFGL 2591 and AFGL 2136, EXES covered the range of 5.3–8 μm and required 16 wavelength settings in its HIGH-LOW mode, where the high-resolution echelon grating is cross dispersed at the lowest practical order/angle so that the instantaneous wavelength coverage was maximized. AFGL 2591 was observed to completion in 2017 March, but AFGL 2136 was observed over three flight series which spanned 2017 March–2019 April. The slit width was 3.″2 for all settings, providing $R = 55{,}000$ resolution. The fixed slit lengths used were either 3.″1 or 2.″2, depending on the wavelength setting. In order to remove background night sky emission and telescope thermal emission, the telescope was nodded to an off-source position 15″ away from the target coordinates every 1–2 minutes. During the flight series, the precipitable water vapor (pwv) meter on board SOFIA was not working; therefore, the quantity of water in the atmosphere could not be measured. Our observation details are shown in Table 1.

The EXES data were reduced with the SOFIA Redux pipeline (Clarke et al. 2015), which has incorporated routines originally developed for the Texas Echelon Cross Echelle Spectrograph (Lacy et al. 2003). The science frames were de-spiked and sequential nod positions subtracted, to remove telluric emission lines and telescope/system thermal emission. An internal blackbody source was observed for flat fielding and flux calibration and then the data were rectified, aligning the spatial and spectral dimensions. The wavenumber solution was calibrated using sky emission spectra produced for each setting by omitting the nod-subtraction step. We used wavenumber values from HITRAN (Rothman et al. 2013) to set the wavelength scale. The resulting wavelength solutions are accurate to 0.3 km s^{-1}.

Standard star spectra were taken for several settings but were found to be of insufficient quality to be effective. In general, these spectra were too noisy such that they needed to be smoothed so much that the required telluric lines were also smoothed out, making them ineffective at dividing out the atmosphere. In some cases, the standard star exhibited emission features that resulted in spurious absorption features being divided into the final spectrum. One advantage of using a standard star spectrum is that, if taken immediately after the science target spectrum, the baseline is largely the same as that of the science target. This allows for efficient removal of the erratic baseline and fringing that were present. We found however that the use instead of an atmospheric model, in this case from ATRAN, proved to be much more effective in removing the atmosphere. While the ATRAN model provided a more governable way of removing the atmosphere, allowing line widths to be controlled, fringing was not removed from our data. Due to the fact that the pwv meter was not working, ATRAN models were constructed at a fixed observatory altitude of 43,000 feet, and the depths of the telluric model lines were then adapted to the observed telluric lines by multiplying the model to a power, denoted Z:

$$F = \frac{F_0}{F_m^{(AZ)}}, \tag{1}$$

where F, F_0, and F_m are the final, original, and model spectra, respectively, and A is the airmass, following the recommendations by the instrument team and outlined in Figure 1. The use of the telluric model in future studies would reduce the large amount of additional time required to observe a standard star spectrum.

2.1. Source Description

The mid-IR continuum of AFGL 2136 and AFGL 2591 is thought to originate from a disk around these massive protostars (Preibisch et al. 2003; Monnier et al. 2009; de Wit et al. 2011; Boley et al. 2013). In the case of AFGL 2136, the

Table 1
Summary of Observations

Source	Date (UT)	Time (UT)	Wavelength Range (μm)	V_{dop} (km s^{-1})	Integration Time (s)	Longitude (deg)	Latitude (deg)	Altitude (feet)	Zenith Angle (deg)
AFGL 2591	2017-03-23	10:06:16	7.83–8.01	25.8	120	−101.7	44.7	42,086	53.2
	2017-03-23	09:51:47	7.67–7.85	25.8	240	−102.6	45.8	42,066	55.0
	2017-03-17	10:34:18	7.51–7.69	24.4	420	−104.3	44.0	44,006	51.9
	2017-03-17	10:15:14	7.34–7.52	24.4	300	−106.5	46.9	43,043	57.1
	2017-03-22	11:47:14	7.19–7.37	25.6	390	−124.1	34.1	43,056	54.1
	2017-03-23	09:32:32	7.02–7.20	25.8	330	−104.2	47.6	42,069	56.9
	2017-03-21	10:14:38	6.87–7.05	25.3	270	−100.8	43.0	43,006	51.2
	2017-03-21	09:55:52	6.69–6.88	25.3	300	−102.5	45.3	41,998	54.4
	2017-03-23	10:14:17	6.53–6.71	25.8	300	−100.2	42.8	42,082	50.9
	2017-03-22	12:10:50	6.36–6.54	25.6	180	−122.8	32.4	43,058	51.3
	2017-03-22	11:23:00	6.18–6.37	25.6	420	−126.3	36.6	43,069	58.1
	2017-03-23	09:07:04	6.01–6.20	25.8	420	−106.7	50.1	42,065	60.6
	2017-03-22	10:50:37	5.82–6.02	25.6	600	−128.7	39.4	43,054	63.1
	2017-03-21	09:32:06	5.65–5.84	25.3	330	−105.0	48.4	42,001	58.6
	2017-03-21	08:45:11	5.48–5.67	25.3	660	−109.1	52.1	42,011	62.9
	2017-03-17	09:37:31	5.35–5.51	24.4	660	−108.9	49.7	42,996	59.2
AFGL 2136	2019-04-24	10:00:12	7.83–8.01	40.5	256	−104.4	36.3	43,014	51.8
	2017-03-23	11:55:34	7.67–7.85	43.8	1170	−117.6	34.5	43,063	51.3
	2017-03-17	11:13:03	7.51–7.69	43.5	840	−110.5	38.8	44,962	60.2
	2017-03-17	11:55:32	7.34–7.52	43.5	660	−114.7	36.0	45,008	55.7
	2017-05-25	09:57:59	7.19–7.37	30.0	810	−121.9	38.7	43,008	51.7
	2017-05-25	10:39:58	7.02–7.20	30.0	840	−128.8	39.4	45,012	53.1
	2017-03-21	10:47:40	6.87–7.05	43.7	1200	−109.3	36.5	43,008	56.8
	2017-03-21	11:54:08	6.69–6.88	43.7	1140	−117.0	32.7	43,008	50.0
	2017-03-23	10:46:19	6.53–6.71	43.8	1440	−110.0	37.4	43,083	56.3
	2017-03-16	11:34:59	6.36–6.54	43.4	1230	−122.4	37.2	43,995	60.9
	2019-04-17	10:01:58	6.18–6.37	41.9	256	−95.1	35.4	42,997	51.7
	2019-04-17	08:35:48	6.01–6.20	41.9	256	−83.7	39.2	43,006	56.5
	2019-04-17	11:10:48	5.82–6.02	41.9	256	−105.2	34.5	43,008	47.2
	2019-04-23	10:19:34	5.65–5.84	40.7	256	−101.1	35.9	43,011	49.7
	2019-04-19	10:01:54	5.48–5.67	41.5	256	−114.8	41.9	43012	61.4
	2019-04-23	11:29:01	5.35–5.51	40.7	256	−112.2	35.0	43015	48.2

Note. V_{dop} is the Earth's velocity relative to local standard rest (LSR) at the time of the observations in the direction of the YSOs. Integration time is the time spent on-source.

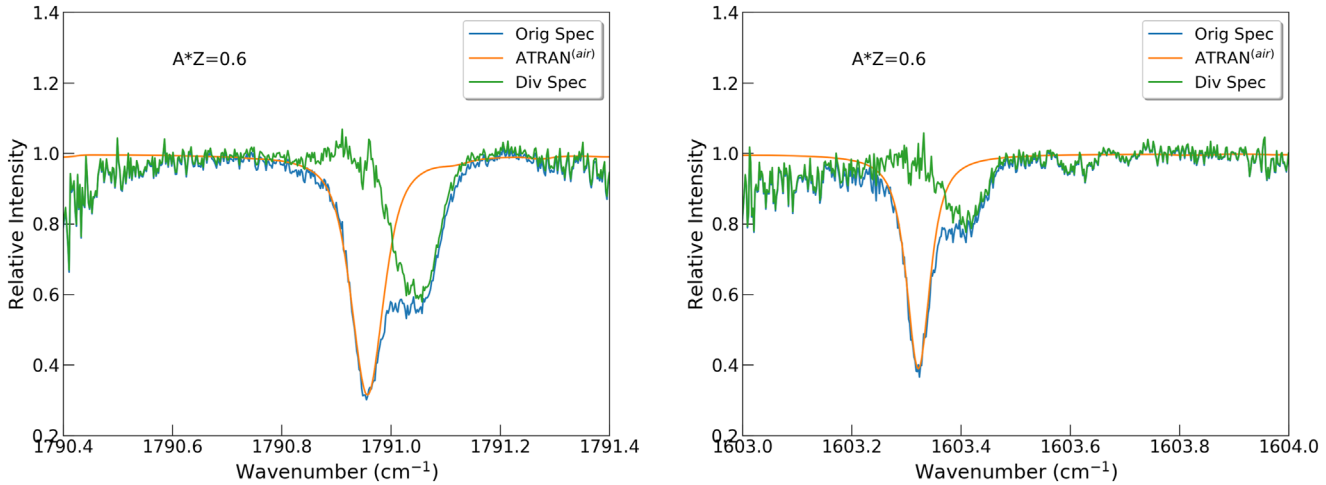

Figure 1. Two examples of absorption lines from AFGL 2136 from different wavelength settings illustrating the division of the telluric lines with the ATRAN model. The original spectrum is shown in blue, the ATRAN model is shown in orange, and the original spectrum divided by the ATRAN model is shown in green. The ATRAN model is scaled by multiplying the model by the power airmass to achieve a good match.

mid-IR continuum interferometry results have been interpreted in terms of an inner dust rim with a radius of >125 au. The absence of small dust grains in the inner 125 au has been attributed to excavation by photoevaporation (Monnier et al. 2009; de Wit et al. 2011; Frost et al. 2021). For AFGL 2591, a similar scenario is suggested with an absence of grains that contribute to the mid-IR continuum in the inner 65 au (Preibisch et al. 2003; Monnier et al. 2009), although the exact

radius is not well determined due to uncertainties in the adopted distance to this source.

The inner 130 au of AFGL 2136 is observed to be gaseous, with a Keplerian disk observed in vibrationally excited H_2O emission detected with the Atacama Large Millimeter Array (ALMA; Maud et al. 2019). As the emitting level is 3462 K above ground, this emission is associated with very hot gas. Coexisting with the H_2O disk are large grains (millimeter size or larger) that create the submillimeter continuum and have not been photoevaporated. The submillimeter continuum is observed to cover the same extent as the gas, of around 120 au in radius. This places the dust and gas observed at submillimeter wavelengths within the proposed dust rim responsible for the mid-IR continuum. There is evidence for a disk wind in AFGL 2136 from radial motion in the disk, which could be driven by the star, supported by the detection of very compact H30α emission potentially driving an ionized disk wind (Maud et al. 2018).

de Wit et al. (2011) and Frost et al. (2021) find that a hot zero-age main-sequence star is too faint to provide enough *N*-band flux to explain the visibilities of AFGL 2136 observed with the MIDI instrument on the Very Large Telescope Interferometer. To reconcile this they propose the presence of a bloated star, which contributes a few percent to the total *N*-band flux to match the observations, in any case implying that the main source of continuum is the disk and not the central protostar.

For AFGL 2591, bright rovibrational ($v_2 = 1$) HCN (4–3) lines with excitation temperatures of $\sim$1060 K and critical densities larger than 10^{10} cm^{-3} probe the warm and dense material in close proximity to the protostar. High-resolution observations with the Northern Extended Millimeter Array of these lines suggest a rotating disk structure in AFGL 2591 with a radius of $\sim$1000 au and a northeast-southwest velocity gradient, which is not in perfect Keplerian rotation. This disk has fragmented into three companion cores with separations of 800 and 1400 au (Suri et al. 2021).

Both young stellar objects (YSOs) are associated with elongated thermal radio emission coinciding with the protostar and elongated parallel to the outflow axis (Trinidad et al. 2003; Menten & van der Tak 2004; Sanna et al. 2012), indicative of photoionization of a jet-generated cone surface (Tan & McKee 2003; Tan 2008; Tanaka et al. 2016, 2017). Size estimates for these compact radio emission sources are 58×6 au (Menten & van der Tak 2004) for AFGL 2136 and 290×125 au for AFGL 2591 (Trinidad et al. 2003; Sanna et al. 2012).

Figure 2 provides a schematic illustration of the structure of AFGL 2136 derived from the literature cited above. While AFGL 2591 has not been studied at the same level of detail, we surmise that the Hot Core circumstellar disk environment of these two sources are very similar, albeit that the details (e.g., relative sizes of the different components; viewing angle) may be different.

3. Analysis

The data presented in this paper are part of a high-resolution spectral survey of the 4–13 μm region of two massive YSOs, AFGL 2591 VLA3 (hereafter, AFGL 2591) and AFGL 2136 IRS1 (hereafter, AFGL 2136). A limited set of water absorption lines in carefully selected, narrow, spectral windows has been analyzed by Indriolo et al. (2015) and Indriolo et al. (2020) for AFGL 2591 and AFGL 2136, respectively. In this work, we build on these studies using the H_2O data from the full 5–8 μm spectral survey, containing 209 H_2O lines in AFGL 2136, and 240 lines in AFGL 2591, in the $v_2 = 1$–0 and $v_2 = 2$–1 rovibrational transitions of the ν_2 band. These are the numbers of lines used in this study, with many more lines having to be discarded due to the reasons outlined below.

Due to many challenges with the data reduction, the absorption lines were analyzed on a line-by-line basis, instead of applying a global reduction to the spectrum as a whole. This involved normalizing the science target spectrum, matching the continuum of the science spectrum and atmospheric model, and dividing the atmosphere out from each echelle order where the given absorption line was present (Figure 1). A first-order polynomial representing the continuum was then fit over the absorption line, which was then divided by this continuum to achieve a flat baseline. Naturally, this introduced some systematic error in the continuum placement as not for every case was it clear where the continuum should go, and removing the baseline fluctuations was not possible since the orders could not be merged in this method. A further systematic uncertainty in the fit was poor removal of the telluric lines in places. The systematic uncertainties are estimated to be negligible to up to a factor of 0.75 of the error on the equivalent width (derived from the statistical noise) depending on the absorption line. Transitions that were blended with very deep telluric lines were discarded since it was not possible to recover the line profiles of these transitions. Likewise, lines that were blended with other hot core lines were discarded.

Lines were fitted in velocity space, with either one or two Gaussians depending on which was appropriate. The variables of the Gaussian model were the peak velocity, $v_{\rm LSR}$, velocity dispersion parameter, σ_v, and the line depth. For AFGL 2136, the $v_{\rm LSR}$ was constrained between 24 and 28 km s^{-1} for the first component and 32 and 36 km s^{-1} for the second component. For both components, σ_v was constrained between 1 and 6 km s^{-1}. In the case of AFGL 2591, the first component was constrained to a $v_{\rm LSR}$ between -18 and -7 km s^{-1}. It was not possible to set the $v_{\rm LSR}$ of the second component as a free parameter, due to the heavy blending of the velocity components. Instead, this was chosen such that it was, for all transitions, 14 km s^{-1} blueshifted with respect to the $v_{\rm LSR}$ of the first component. The value of 14 km s^{-1}, however, has a certain error associated with it. This will be discussed further in Section 4. Both components were fit with σ_v between 1 and 8 km s^{-1}. The line widths have been deconvolved with the instrument profile.

Rotation diagrams presented in Section 4 are created using the Boltzmann equation. The column density in the lower rovibrational level is calculated using the optically thin relation

$$N_i = \frac{g_l}{g_u} \frac{8\pi}{A_{ul} \lambda_{ul}^3} \int \frac{\tau_i(v)}{\phi_i(v)} dv, \quad (2)$$

where $i = 1$, 2 for the two velocity components. N_i is the column density of the lower level, g_l and g_u are the statistical weights for the lower and upper level respectively, A_{ul} is the spontaneous emission coefficient for the transition, λ_{ul} is the wavelength of the line, $\tau(v)$ is the optical depth profile of the line in velocity space, and $1/\phi(v)$ is equal to 1 for an integrated line. If the lines are optically thin and LTE is a valid

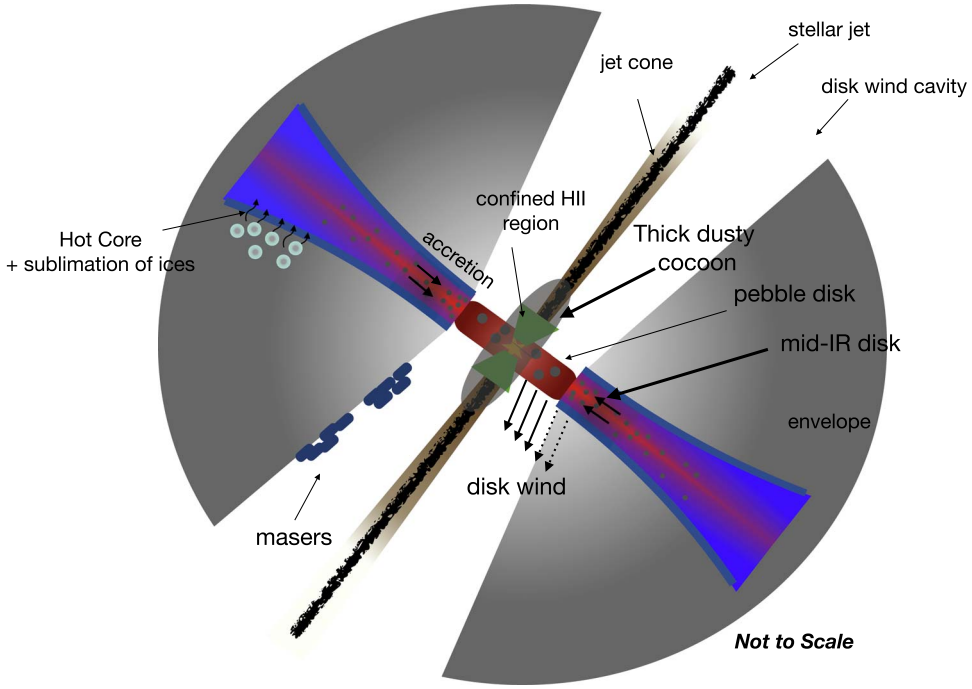

Figure 2. Cartoon illustration of the different physical components of the proposed disk and its surroundings (not to scale), and the mechanisms relevant to the discussion, based on observational evidence for AFGL 2136. A jet has carved a narrow channel (shown in brown) through the thick cocoon around the massive protostar, shown in transparent gray. The radiation from the central star escapes through this channel, creating a flashlight effect. Near the star, the gas in the channel walls is ionized by the stellar radiation, producing a confined H II region, indicated by the green region. A disk wind, represented by the solid lines, has removed gas and small dust grains in the disk within 125 au but leaving a thin pebble disk. The thin inner pebble disk is the source of the continuum and the vibrationally excited H_2O lines in the submillimeter, while the continuum and absorption lines in the mid-IR originate from the dust disk beyond 125 au. The disk is heated internally through viscous processes, leading to accretion. We see evidence for the wind from the mid-IR absorption lines in AFGL 2591, represented by the dotted lines. Outside of 125 au, the disk wind is not strong enough to excavate gas and (small) grains. On a scale of 1000 au, the disk is not warm enough to observe at mid-IR wavelengths; therefore, the mid-IR disk is only observed out to a limited portion of the whole disk. At around 1000 au, the gas is warmer than ∼100 K and ices evaporate, leading to the release of complex organic molecules (COMs) from grain surfaces as well as the gas-phase production of COMs. This is the hot core region. There is a lack of COMs detected in a disk-like structure in AFGL 2136, but rather CH_3OH is observed in a plume structure, suggesting that this object is late on it is evolution, consistent with the detection of unresolved H30α emission in a very compact region (Maud et al. 2018). AFGL 2591 on the other hand does show CH_3OH on scales of 1000 au in a disk-like structure (Jiménez-Serra et al. 2012). The location of maser emission is located, tracing the cavity walls. The temperature and density of the disk increase toward both the midplane and the central star, with the color scale representing the temperature where red is hot and blue cold. The large-scale gray color represents the surrounding envelope in which the disk is embedded. For AFGL 2591, the observer looks into the cone of the blueshifted outflow, whereas for AFGL 2136 the observer looks more into the plane of the disk (inclination of 40°).

assumption, data points on the rotation diagram follow a straight line with slope $-1/T$, with temperature T.

3.1. Foreground Absorption

In order to attend to the effects of optical depth, we introduce a curve of growth analysis that is based on the assumption of a background light source seen through a dust-free absorbing slab of gas. We assume that each velocity component of the absorption lines is caused by a single cloud. In principle, it is possible that each velocity component consists of a blend of multiple gas clouds. However, in the absence of other constraints, this would merely introduce additional free parameters. We stress that the derived level populations as a function of energy or as a function of optical depth do not reveal systematic behavior indicative of contributions by multiple components. Hence, if there were multiple components present, their physical conditions and column densities would have to be very similar. The theoretical curve of growth can be approximated by

$$\frac{W_\lambda}{bf_c\lambda} \sim \frac{\sqrt{\pi}}{c}\frac{\tau_p}{1+\tau_p/2\sqrt{2}} \tag{3}$$

for $\tau_p < 1.254$, and

$$\frac{W_\lambda}{bf_c\lambda} \sim \frac{2}{c}\sqrt{\ln[\tau_p/\ln 2] + \frac{\gamma\lambda}{4b\sqrt{\pi}}(\tau_p - 1.254)} \tag{4}$$

for $\tau_p > 1.254$, taken from Tielens (2021) with the additional factor $1/f_c$ to take into account a covering factor. Here W_λ is the equivalent width, λ is the wavelength, τ_p is the peak optical depth, b is the Doppler width, and γ is the damping factor. The Doppler parameter, b, is related to the velocity dispersion via $b = \sqrt{2}\,\sigma_v$. The expression for τ_p is given by

$$\tau_p = \frac{\sqrt{\pi}e^2 N_l f_l \lambda}{m_e c b}, \tag{5}$$

where N_l and f_l are the column density and oscillator strength in the lower level, respectively, e is the electron charge, m_e is the electron mass, and τ_p is integrated over wavelength. In the empirical curve of growth, we introduce an additional parameter, f_c, the covering factor of the absorbing gas, which is divided into the equivalent width (e.g., the left-hand side of Equations (3) and (4) become $W_\lambda/b\lambda f_c$). This parameter describes the covering of the background illuminating source, where a smaller covering factor will result in a smaller

Table 2
H_2O Absorption Physical Conditions

Source	Band	Number of Lines	Temperature (K)	Column Density (cm^{-2})	Temperature (K)	Abundance (w.r.t CO)	Allowed Values of σ_v (km s^{-1})
			Foreground Model		Atmosphere Model		
AFGL 2136	ν_2 $v_2 = 1-0$	154	457^{+13}_{-14}	$3.6^{+0.1}_{-0.1} \times 10^{18}$	470^{+24}_{-33}	$1.6^{+0.3}_{-0.1}$	1.0–3.2
	ν_2 $v_2 = 2-1$	55	585 ± 28	$3.9 \pm 0.1 \times 10^{16}$	585 ± 28	$9.2 \pm 0.4 \times 10^{-3}$	⋯
AFGL 2591	ν_2 $v_2 = 1-0$	177	541^{+1}_{-8}	$1.5^{+0.1}_{-0.1} \times 10^{19}$	625^{+27}_{-22}	$7.4^{+0.5}_{-0.4}$	1.0–4.0
	ν_2 $v_2 = 2-1$	63	418^{+28}_{-16}	$1.0^{+0.2}_{-0.2} \times 10^{17}$	403^{+27}_{-25}	$7.3^{+0.6}_{-0.4} \times 10^{-2}$	⋯

Note. The column density and temperature derived from the slab model curve of growth are presented as well as the abundances and temperatures from the stellar atmosphere curves of growth with $\epsilon = 0.5$. Parameters of the ν_2 $v_2 = 2$–1 band in AFGL 2136 are taken from the rotation diagram. The upper and lower subscripts denote the 1σ error from the contour plots.

Table 3
Chemical Abundance Ratios

	HCN/CO ($\times 10^{-2}$)	C_2H_2/CO ($\times 10^{-2}$)	NH_3/CO ($\times 10^{-3}$)	HCN/C_2H_2	CS/CO ($\times 10^{-3}$)	H_2O/CO	HCN/CO 13 μm ($\times 10^{-2}$)	C_2H_2/CO 13 μm ($\times 10^{-2}$)
AFGL 2591[a]	10.0	>1.1[b]	20	<9.1[b]	7.5	7.4[g]	2.0	1.1
AFGL 2136[a]	2.0	1.0	2	1.8	1.3	1.6[g]	0.6	0.3
Hot core[c]	0.009	⋯	0.004	⋯	0.004	8×10^{-4}	⋯	⋯
T Tauri disk[d]	3	2	<5	1.5	⋯	2	⋯	⋯
Herbig disk[e]	<2.2	<1.0	⋯	2.2	⋯	1.0	⋯	⋯
Shock[f]	<0.003	<0.004	⋯	⋯	⋯	≃0.02	⋯	⋯

Notes.
[a] In interpreting the observed abundance ratios, it should be recognized that they are measured at different wavelengths and may therefore (partially) originate from different regions in the disk with inherent somewhat different dust continuum properties in the mid-IR.
[b] Upper limits are placed on C_2H_2 because, while this species was detected at 13 μm in AFGL 2591, the undiluted band at 7 μm was not detected.
[c] Submillimeter observations of the hot core of AFGL 2591 (Kaźmierczak-Barthel et al. 2014)
[d] Observations of T Tauri disks by Carr & Najita (2008). NH_3 was not studied by Carr & Najita (2008); therefore, this upper limit was taken from Pontoppidan et al. (2019).
[e] Average of the sample of Herbig disks from Salyk et al. (2011).
[f] Values for HCN and C_2H_2 are taken from peak 1 in Orion (Boonman et al. (2003); their model 3). The H_2O abundance is taken from Goicoechea et al. (2015).
[g] Taking the H_2O abundance from Table 2.

observed equivalent width. To be precise, we fit f_{cb} in the curve of growth fitting, as these two parameters are degenerate. We do note that b is relatively well constrained by the observed line widths, but still could take a range of appropriate values.

The level populations are related as follows:

$$N_l = \frac{g_l N}{Q(T)} e^{-E_l/T}, \tag{6}$$

where $Q(T)$ is the partition function, N is the total column density of the species, E_l is the energy of the lower level in Kelvin, and T is a free parameter that will be of the order of the temperature derived from the rotation diagram. Physical conditions derived under the assumption of this model are summarized in Table 2, and chemical abundance ratios are given in Table 3.

3.2. Disk Atmosphere

Alternatively, we consider the stellar atmosphere model developed by Barr et al. (2020) and construct curves of growth in this regime also, following the stellar atmosphere theory of Mihalas (1978). Curves of growth in this approximation are constructed using the equation

$$\frac{W}{2Y\Delta\nu} = \int_0^\infty \frac{\eta_0 H(a, v)}{1 + \eta_0 H(a, v)} dv, \tag{7}$$

where W is the equivalent width of the absorption lines in frequency space, $\Delta\nu$ is the Doppler width in units of hertz, and Y takes into account the temperature gradient in the atmosphere. For the derivation and definition of Y, see Appendix A in Barr et al. (2020).$H(a, v)$ is the Voigt profile as a function of the frequency shift, v (in velocity space and normalized to the Doppler parameter), and a the damping parameter (in Doppler units). The latter only plays a role in the square root portion of the curve of growth and this is not relevant here. The right-hand side of this equation can be calculated as a function of η_0, resulting in a theoretical curve of growth. We have used the simple approximations to this provided by Mihalas (1978), assuming a gray opacity. η_0 is the opacity at the line center set relative to the continuum opacity given by

$$\eta_0 = \frac{\kappa_L(\nu = \nu_0)}{\kappa_c} = \alpha \frac{A_{ij}\lambda^3}{8\pi\sqrt{2\pi}\,\sigma_v} \frac{g_u}{g_l} \frac{X_l}{X_{CO}}, \tag{8}$$

where X_l is the abundance in the lower level and α is a parameter set by the requirement that the CO abundance, X_{CO}, is 10^{-4}, which results in $\alpha = 1.3 \times 10^{19}$ and 2.3×10^{18} H nucleus/cm^2 for AFGL 2136 and AFGL 2591, respectively. Here, the continuum opacity κ_c is equal to $\sigma_c N_H$, where σ_c is

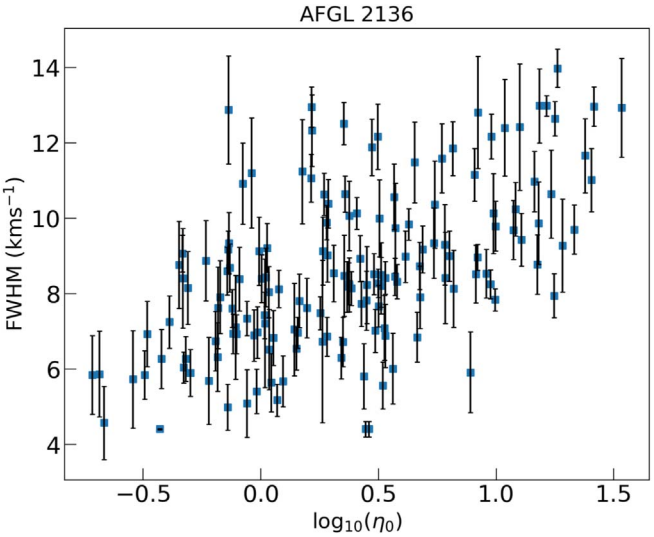

Figure 3. Trend between η_0 with the line width in AFGL 2136.

the dust cross section per H nucleus calculated as X_{CO}/α, in units of square centimeters per H nucleus In adjusting this parameter to a free parameter, we recognize that coagulation and settling of large grains and/or turbulent size sorting may have affected the dust abundance and opacity per H atom, and that this depends on the physical conditions and history of the disk (Dullemond & Dominik 2008; Cuzzi et al. 2008; Ormel et al. 2011).

As in the curve of growth for Equations (3)–(5), the level populations are related by Equation (6), with the difference that it is no longer the column density of the lower level but the abundance with respect to H nuclei; and thus N is replaced by the total abundance with respect to H, $X(H_2O)$. Adopting an abundance, temperature, and Doppler parameter for the absorbing gas, the left-hand side of Equation (7) as well as η_0 can be calculated for each line, resulting in an empirical curve of growth.

Empirical curves of growth are created for a range of different values of T and $X(H_2O)$ and these are fit to the theoretical curve of growth. This fit is quantified by a least square process where the best combination of T and N or $X(H_2O)$ is chosen such that the reduced chi-square is the lowest. The errors on these best-fit parameters are taken from the 1σ contour in the corresponding error plot. These contour plots have been normalized to the minimum reduced chi-square from the fitting procedure. Physical conditions derived for the disk model are also summarized in Table 2.

4. Results

4.1. AFGL 2136

For AFGL 2136 we only focus on the velocity component with peak velocity fit between 24 and 28 km s^{-1} since this is the main absorbing component seen also in HCN, C_2H_2, NH_3, and CS (Barr et al. 2020). For the $v_2 = 1$–0 band, all peak velocities are in agreement and there is no evidence for any velocity trends with opacity. We derive an average value of 25.5 ± 1.1 km s^{-1} for the v_{LSR}. There is however an overall increase of the line width with η_0, by a factor of 2, shown in Figure 3. Figure 4 illustrates that lines with high opacity are clearly broader.

As was noted by Indriolo et al. (2020), the rotation diagram shows a large scatter that cannot be accounted for by the error bars (Figure 5). This is evident by the underprediction of the column density of a number of lines, most prominent for those with high η_0 values, i.e., high Einstein A coefficients and/or high column densities. As a result of this, the temperature and column density derived from the rotation diagram do not reflect the true physical conditions. This effect is illustrated more clearly in Figure 6, which shows the column density of a number of levels for which we have multiple transitions. The individual transitions should yield the same column density but as this figure illustrates, lines with high η_0 systematically yield lower column densities.

The line profiles can provide further insight where, in Figure 7, we plot absorption lines from the $7_{2,5}$ level against LTE models that assume an absorbing slab of gas that is not mixed with the dust, with $f_c = 1$ and $f_c = 0.4$. The LTE models are generated at the physical conditions derived from the slab curve of growth. Five lines are shown with varying opacity. Observed absorption lines do not go to zero, as would be expected for very optically thick lines under the assumption of an absorbing slab that fully covers the source, but instead saturate at 40% relative to the continuum. With a covering factor of 0.4 for AFGL 2136, the LTE model matches the observed line profiles. The behavior presented in Figure 6 is a result of the lines saturating, as we have assumed that the absorbing gas fully covers the source in the rotation diagram analysis. Therefore, a curve of growth analysis is required.

We present the results of the curve of growth from the absorbing slab model for AFGL 2136 in Figure 8. We constrain f_c by the condition that this parameter must be equal to the depth of the deepest absorption line (on a continuum-normalized flux scale). From Figure 7, we fix f_c to 0.4 for AFGL 2136. We then carried out the chi-square fitting routine to find the best-fit combination of T and N, for a range of different Doppler widths, thus fitting three parameters. We find that a Doppler width of 3.75 km s^{-1} gives the best fit, and the minimum chi-square of the temperature/column density grid for this b corresponds to 457^{+13}_{-14} K and $3.6^{+0.1}_{-0.1} \times 10^{18}$ cm^{-2}. This value of b corresponds to a value of 2.7 km s^{-1} for σ_v. While this is the best-fit model, by eye the curve of growth does not fit well for the low opacity lines. A more linear behavior for the low opacity lines is obtained for an excitation temperature of 600 K and a column density of 2.3×10^{18} cm^{-2}, at the cost of an increased spread of the points around the theoretical curve of growth (and a larger chi-square). This does not depend strongly on the adopted line width. The intrinsic σ_v may vary between 1 km s^{-1}—appropriate for the thermal motion of this gas—and the observed line width of the narrowest lines (3.2 km s^{-1}); however, line widths below 2.5 km s^{-1} do not fit the theoretical curve of growth. The chosen Doppler parameter introduces an uncertainty of 20% and 30% in the derived temperature and column density, respectively, and does not noticeably improve the fit by eye, as shown in Figure 8. The rotation diagram is corrected for optical depth effects by extrapolating the equivalent width for the calculated τ_p of each optically thick absorption line to a linear relation in the curve of growth. The rotation diagram is recalculated; however, the correction still shows considerable scatter (Figure 8).

We also pursue a curve of growth analysis based on the stellar atmosphere model presented in Barr et al. (2020). We

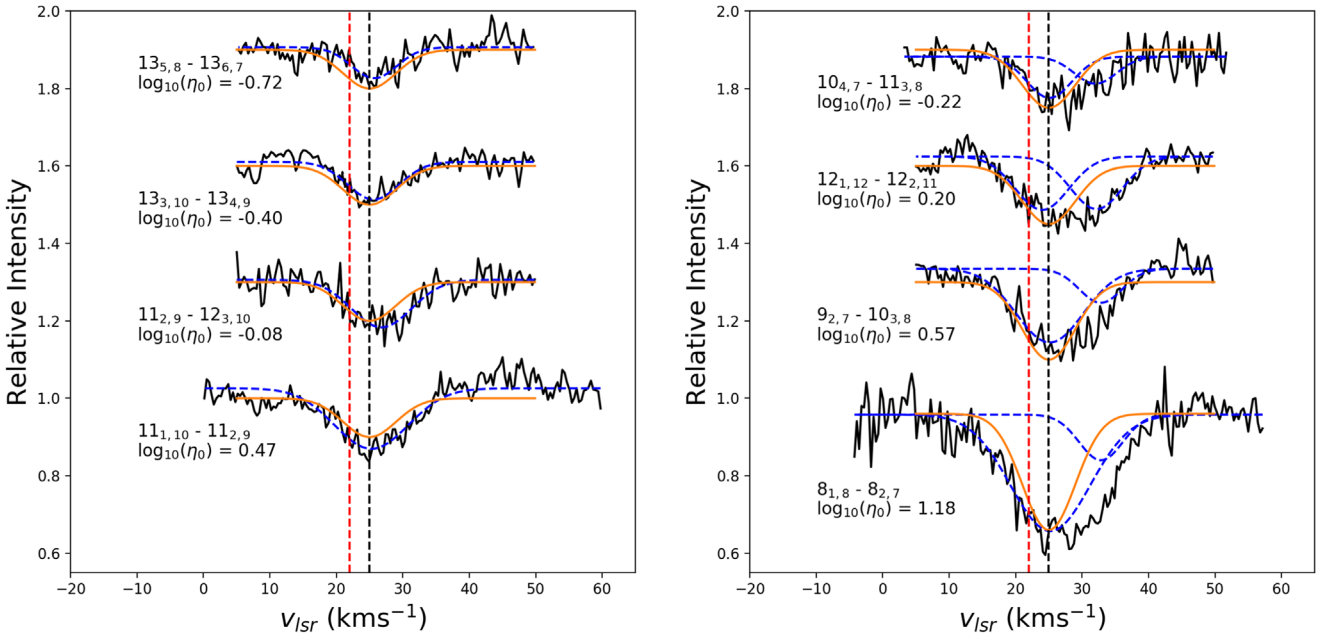

Figure 4. Line profiles of AFGL 2136 showing transitions of different opacity. Absorption lines are shown that exhibit one and two velocity components in the *left* and *right* panels, respectively. Shown in orange is a Gaussian with a $v_{\rm LSR}$ of 25 km s^{-1} and a σ_v of 4 km s^{-1}. The blue dashed lines denote the Gaussian fits to each velocity component. The black dashed line at 25 km s^{-1} is added for a reference and the red dashed line at 22 km s^{-1} indicates the velocity of the gaseous envelope as observed at submillimeter wavelengths.

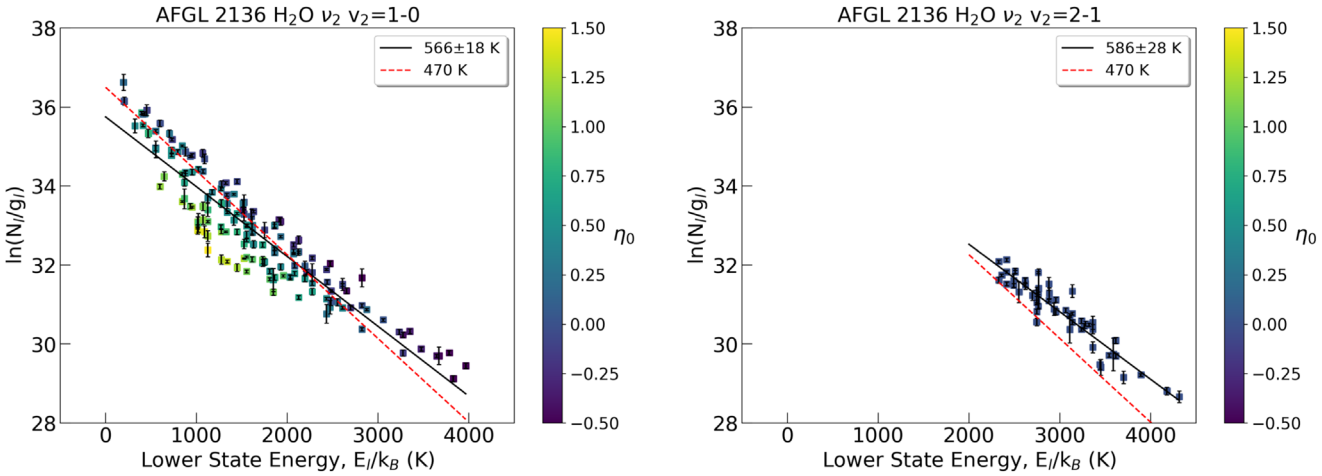

Figure 5. Rotation diagrams of the H_2O $v = 1$–0 (*left*) and vibrationally excited $v = 2$–1 (*right*) transitions of the ν_2 band in AFGL 2136. The color bar is a function of $\log_{10}(\eta_0)$. The dashed red line denotes the temperature of 470 K derived from the curve of growth (see section 5.1). The solid black lines denote the fit to the rotation diagrams, and the temperatures of these fits are given in the legend.

calculate empirical curves of growth with boundaries on the line width of $1 \lessapprox \sigma_v \lessapprox 3.2$ km s^{-1}. Figure 9 shows the curve of growth under the assumption that lines are formed through a combination of absorption and scattering ($\epsilon = 0.5$; see Barr et al. 2020 for details). We find that the best-fit value for the Doppler parameter is for $\sigma_v = 3.0$ km s^{-1}. The temperature and abundance with respect to CO are 470^{+24}_{-33} K and $1.6^{+0.3}_{-0.1}$, respectively. This temperature is very similar to those of CO, CS, and NH_3 in this source, whereas the temperatures of HCN and C_2H_2 are higher by 200 K (Barr et al. 2020). The cases of line formation in the approximation of pure scattering ($\epsilon = 0$) and pure absorption ($\epsilon = 1$) are also considered and shown in Figures 10 and 11, respectively. For all cases, we find that σ_v of 3.0 km s^{-1} provides the best fit. The derived temperature is not very dependent on the choice of ϵ; however, the abundance increases from $0.5^{+0.1}_{-0.1}$ for $\epsilon = 1$, to $1.3^{+0.1}_{-0.2}$ for $\epsilon = 0$, to $1.6^{+0.3}_{-0.1}$ for $\epsilon = 0.5$. The correction to the rotation diagram (Figure 9) is good for all ϵ, with a closer to linear result compared to the slab model.

The temperature obtained from the slab analysis agrees with the temperature from the stellar atmosphere analysis, within the errors. The best-fit value for σ_v in the stellar atmosphere model is 3.0 km s^{-1}, compared to 2.7 km s^{-1} for the slab model. We cannot directly compare the column density derived from the two methods. Goto et al. (2019) measured the ^{12}CO $v = 2$–0 band and derived a temperature and column density of 530 ± 80 K and $2.8 \pm 0.4 \times 10^{19}$ cm^{-2}, respectively. With this column density, we find a H_2O/CO ratio of 0.1. This is an order of magnitude lower than what we find for the H_2O abundance relative to CO from the stellar atmosphere model; however, the $v = 2$–0 band is at 2.3 μm and therefore differing

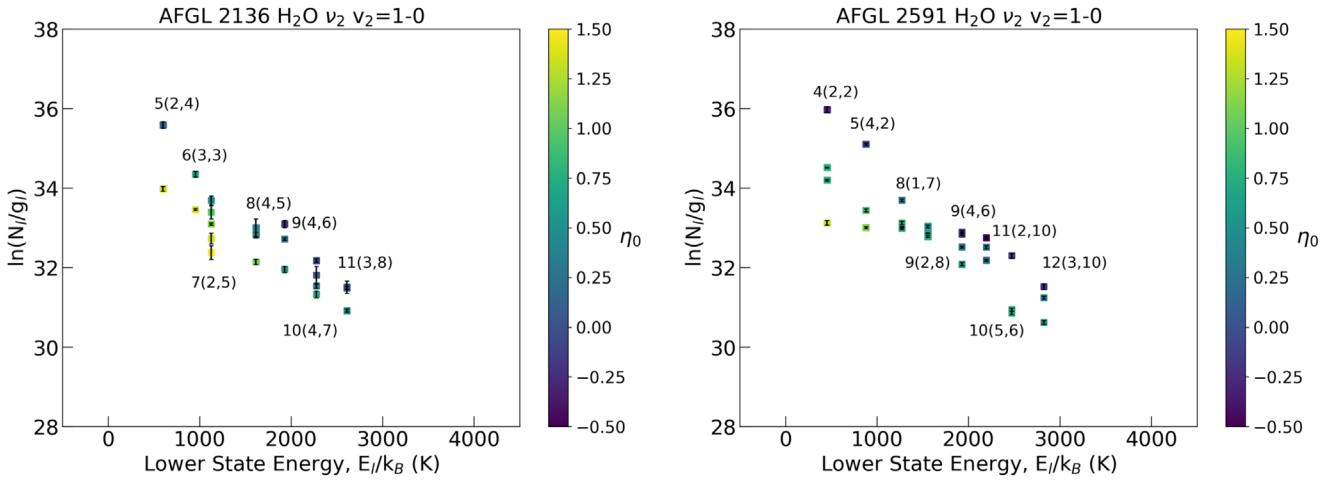

Figure 6. Rotation diagrams of AFGL 2136 and AFGL 2591 showing a selection of lines that have transitions out of the same lower level. These levels are indicated in the plots.

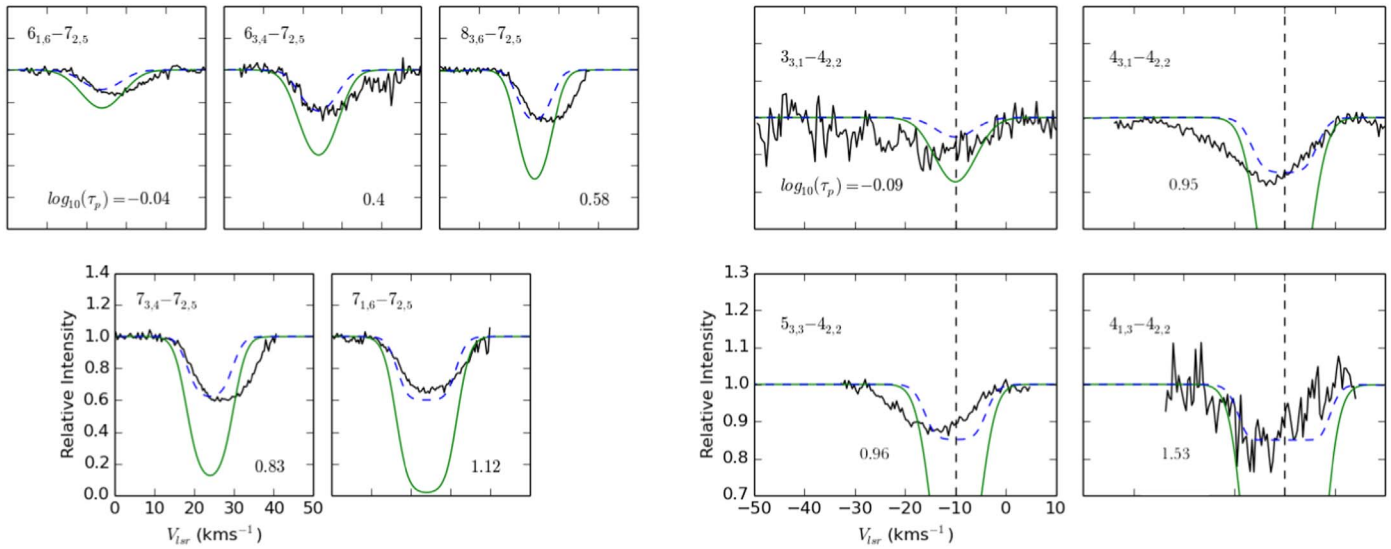

Figure 7. Absorption lines in AFGL 2136 of H_2O that trace the $7_{2,5}$ level (*left*) and the $4_{2,2}$ level in AFGL 2591 (*right*). The green solid line denotes a model of a background light source seen through a dust-free absorbing slab of gas, with $f_c = 1$, generated at the physical conditions derived from the slab curves of growth. The blue dashed line is the same as the green solid line but with a covering factor, f_c, of 0.4 applied. The opacities of each observed τ_p are indicated in the corresponding panels. The dashed vertical line in the plots for AFGL 2591 denotes -10 km s^{-1} for a reference.

source sizes at different wavelengths could have some effect. The derived physical conditions are summarized in Table 2 and all line parameters are given in Table 4. The full line parameters for the $v = 2$–1 transition are given in Table 5.

Although there is a large scatter, there is a trend of increasing line width with opacity (Figure 3). This is also true of AFGL 2591 (Section 4.2; Figure 14). This may be a consequence of the high opacity absorption lines moving onto the logarithmic part of the curve of growth, thus starting to broaden. There is no obvious cause for the large scatter in this trend, which may reflect the systematic error in the line fitting.

Four lines of $H_2^{18}O$ are detected in AFGL 2136 and curves of growth are shown in Figure 12 and summarized in Table 6. The temperature we derive is 252^{+7}_{-12} K and 260^{+11}_{-67}, for the stellar atmosphere and slab models, respectively. This is lower than the temperature for $H_2^{16}O$, which may reflect the fact that these lines have lower energy levels, and therefore probe colder gas. The abundance with respect to CO is $3.6^{+0.3}_{-0.3} \times 10^{-3}$, which results in a $^{16}O/^{18}O$ ratio of 444 ± 83, consistent with the standard interstellar medium (ISM) value of 500 (Wilson & Rood 1994).

For the vibrationally excited $v_2 = 2$–1 band, absorption line profiles are consistent with each other and no evidence for trends in peak velocity or line width is present. The average σ_v and $v_{\rm LSR}$ for the $v_2 = 2$–1 band are 3.1 ± 1.0 km s^{-1} and 25.7 ± 1.3 km s^{-1}, respectively. This is in good agreement with the $v_2 = 1$–0 band. In the rotation diagram, all transitions can be fit with a straight line. All lines have very low values for η_0 and therefore will lie in the linear part of the curve of growth. We therefore derive the temperature and abundance/column density for this band from the rotation diagram. These parameters are summarized in Table 2. Given the measured relative populations of the $v = 1$–0 and $v = 2$–1 vibrational states of H_2O, we derive a vibrational temperature of 452 ± 57 K for H_2O, very close to the rotational temperature. This similarity in excitation temperature implies that the gas is very dense and close to the critical density for the vibrational levels, 10^{11} cm^{-3} (Faure & Josselin 2008). As this is higher than the

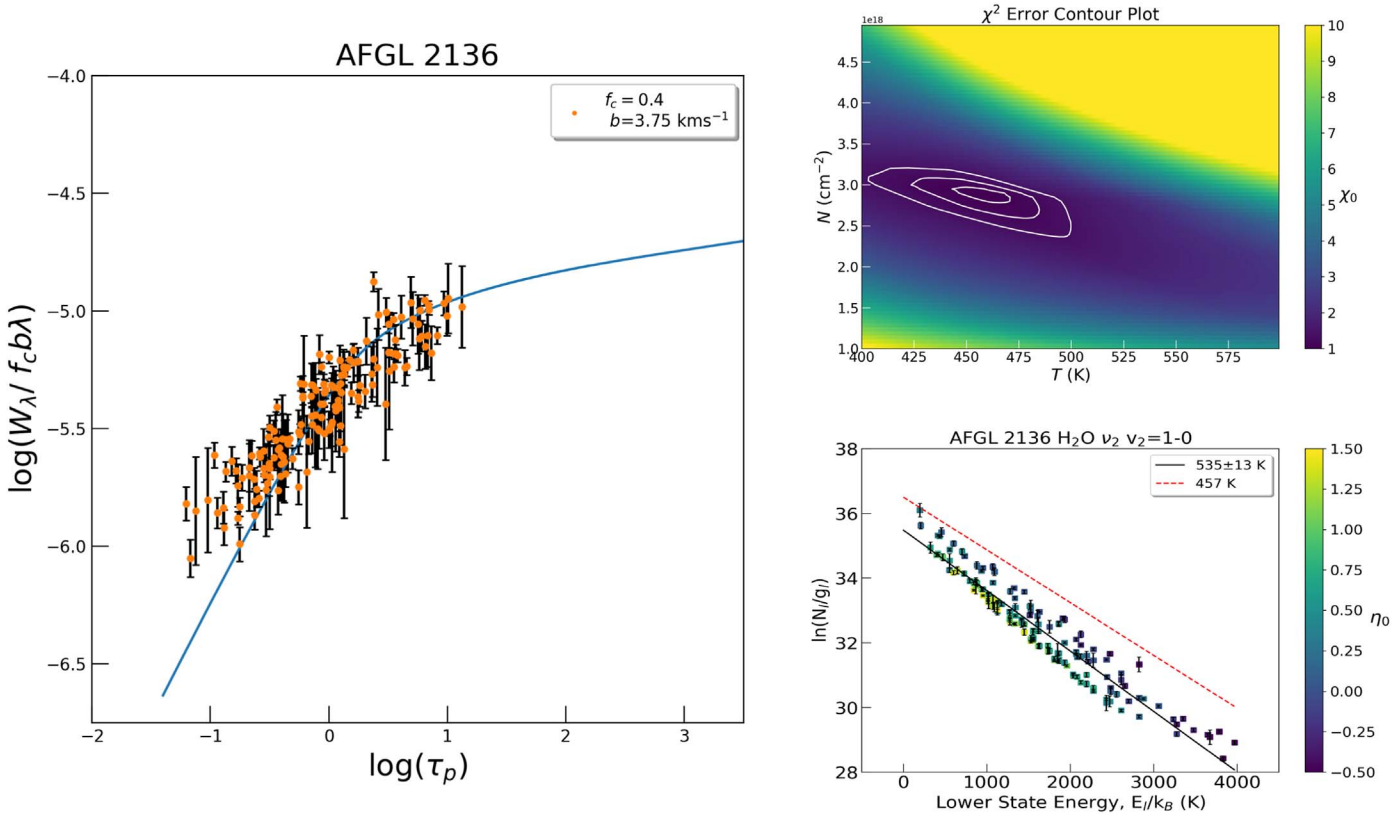

Figure 8. *Left*: the curve of growth for the $v = 1$–0 transition of AFGL 2136 for the slab model, taking a covering factor of 0.4 and $b = 3.75$ km s^{-1}. The best-fit empirical curve of growth is shown and the corresponding best-fit temperature and column density are indicated. *Upper right*: the error on the parameters is given in the contour plot where the color scale is the reduced chi-square value. The contours represent the 1σ, 2σ, and 3σ uncertainty levels. *Lower right*: the column densities for the optically thick lines were determined using the curve of growth. The best-fit temperature of 457 K from the slab curve of growth is represented by the red dashed line. The black solid lines are fits to the corrected data set and the corresponding temperatures are indicated for each case.

critical density for rotational excitation, 10^8 cm^{-3}, this implies that the kinetic temperature of gas is equal to the excitation temperature of the rotational population, 500 K.

The $\nu_3 = 1$–0 band at 2 μm was observed in absorption by Indriolo et al. (2020). All lines lie in a straight line in the rotation diagram indicative of optically thin gas; therefore this band likely gives a reliable handle on the temperature, 502 ± 12 K.

4.2. AFGL 2591

The absorption line profiles in AFGL 2591 are complex. The systemic velocity of the envelope of this source is $v_{\rm LSR} = -5.5$ km s^{-1} (van der Tak et al. 1999; Wang et al. 2012; Gieser et al. 2019). The presence of two velocity components is obvious in several examples, one at -10 km s^{-1} and one at -25 km s^{-1} (Figure 13) and we refer to these as the major and minor components, respectively. There is no consistent trend in Einstein A or energy level, E_l, for the presence and/or strength of the minor velocity component; e.g., some strong lines show only one component, whereas some show two, and some lines with equivalent energies show both one and two components (Figure 13). This may reflect different excitation conditions in the minor component compared to the major one. Due to the heavy blending of the two velocity components, in order to achieve reasonable fits the $v_{\rm LSR}$ of the minor component could not be left a free parameter in the fitting routine, and instead had to be fixed to a certain velocity.

In contrast to AFGL 2136, the $v_2 = 1$–0 band reveals variations in the peak velocity, with some lines appearing shifted with respect to each other. There is a general trend between the peak velocity and the opacity of the transition (Figures 13 and 14). This is the case for all lines, whether the minor component is present or not. As a result of this trend, the $v_{\rm LSR}$ of the minor component also changes, since it is the composite line profile that shifts. In order to minimize the uncertainty of the placement of the minor component, we applied a constraint that the two velocity components should be separated by the same amount; 14 km s^{-1} for all transitions. However, it is not possible to achieve this exactly, as we fix the velocity of the minor component and allow the velocity of the major component to vary. Thus, the peak velocity of the major component prefitting was estimated by eye, looking at the composite line profile. Then the peak velocity for the minor component to be used in the fitting was chosen based on this estimate. Naturally, this leads to some uncertainties in the placement of the minor velocity component, and therefore, most importantly, the integrated line strength of the major velocity component. A separation of 14 ± 1 km s^{-1} between the two components is more accurate, and this constraint gives a good fit to the line profiles and curves of growth. Not accounting for the shift of the minor component introduces a large scatter in the curve of growth. Furthermore, the lines show an overall variation in line width, as illustrated in Figure 14. Referring to the results below, we note that this line width increases with increasing η_0. This trend was noted previously by Indriolo et al. (2015). Combined with the trends

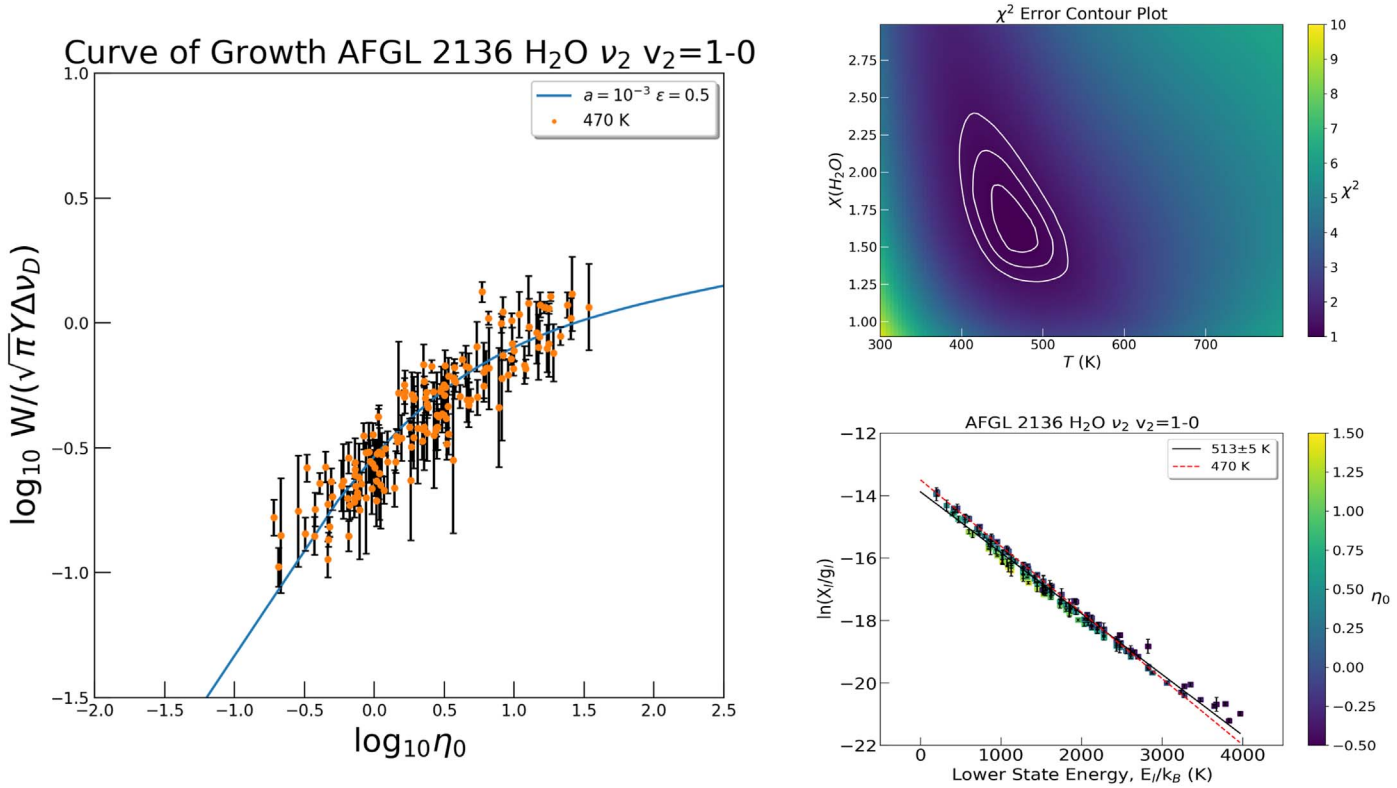

Figure 9. *Left*: the curve of growth for the $v = 1$–0 transition of AFGL 2136 for the stellar atmosphere model. The theoretical curve is for the case of a mixture of absorption and scattering, with a damping factor, a, of 10^{-3}. The best-fit empirical curve of growth is shown and the corresponding best-fit temperature is indicated. *Upper right*: the error on the parameters is given in the contour plot where the color scale is the reduced chi-square value. The contours represent the 1σ, 2σ, and 3σ uncertainty levels. The H_2O abundance is quoted relative to CO. *Lower right*: the rotation diagram is a function of η_0 and the abundances for the optically thick lines were determined using the curve of growth. The best-fit temperature of 470 K from the curve of growth is represented by the red dashed line. The black solid lines are fits to the corrected data set and the corresponding temperatures are indicated for each case. Note that the y-axis is the abundance in the lower level based on the stellar atmosphere theory.

in peak velocity and line width, we are limited in terms of the line fitting. It is not possible to accurately determine the physical conditions of the minor component since it is too weak and difficult to disentangle from the major component.

The rotation diagrams for the $v_2 = 1$–0 and $v_2 = 2$–1 bands are shown in Figure 15. For the $v_2 = 1$–0 band, the scatter is far more accentuated compared to that seen in AFGL 2136. Figure 6 illustrates this point for levels that trace the same lower level across a range of energies.

As in AFGL 2136, Figure 7 shows that absorption lines do not go to zero flux, even when they have very large opacities. Four lines from the $4_{2,2}$ level are shown. These lines should have the same column density as they originate from the same lower level; however, this is not the case as shown in Figure 6. Absorption lines saturate at 15% relative to the continuum, and therefore lines with larger and larger opacity exhibit a greater discrepancy with the absorbing slab model. Saturation occurs at a lower flux than in AFGL 2136 and hence the more extreme scatter in the rotation diagram compared to AFGL 2136.

We show the results of the curve of growth analysis in the approximation of an absorbing slab for AFGL 2591 in Figure 16. As a result of the complexity of the line profiles, the scatter in the curve of growth for AFGL 2591 is dominated by systematic error. Therefore, we determine the fit to the curve based only on lines that show a single velocity component and then apply the derived physical conditions to the data set as a whole. Again we fix the value for f_c from Figure 7. This sets a value of approximately 0.15 for AFGL 2591. We find a best-fit temperature and column density of 541^{+1}_{-8} K and $1.5^{+0.1}_{-0.1} \times 10^{19}$ cm^{-2}, respectively. The value for b, which gave the lowest chi-square value, was 5.25 km s^{-1}. This value for b corresponds to a value of 3.7 km s^{-1} for σ_v. For AFGL 2591, we fix σ_v between 1 and 4 km s^{-1}.

The curve of growth in Figure 17 for the stellar atmosphere model gives a temperature and abundance with respect to CO of 625^{+27}_{-22} and $7.4^{+0.5}_{-0.4}$, respectively, assuming $\epsilon = 0.5$. The best-fit value for σ_v in this case is 2.75 km s^{-1}. For the other processes of line formation, we find different values of σ_v fit better, with 2.0 and 1.5 km s^{-1} for $\epsilon = 0$ and 1, respectively. These curves of growth are shown in Figures 18 and 19. We also find that the abundances are different with $7.9^{+0.6}_{-0.5}$ and $4.2^{+0.3}_{-0.2}$ for ϵ of 0 and 1, respectively, while the temperature varies by only 25 K.

Comparing the slab analysis to the stellar atmosphere analysis, we find that for AFGL 2591, the temperatures are significantly different, but agree within the 3σ error bars, with 541^{+11}_{-21} K and 625^{+82}_{-70} K, respectively. Taking the column density of 9.3×10^{16} cm^{-2} for ^{13}CO (Mitchell et al. 1990) and a $^{12}C/^{13}C$ ratio of 60, we find a H_2O/CO ratio of 2.7, using the water column density derived from the slab model. This is a factor of 2–4 lower than that we derive from the stellar atmosphere curve of growth, depending on the value of ϵ. The corrected rotation diagrams for the stellar atmosphere approach are better than those for the slab model, although the slab model still does a good correction. The physical conditions are summarized in Table 2.

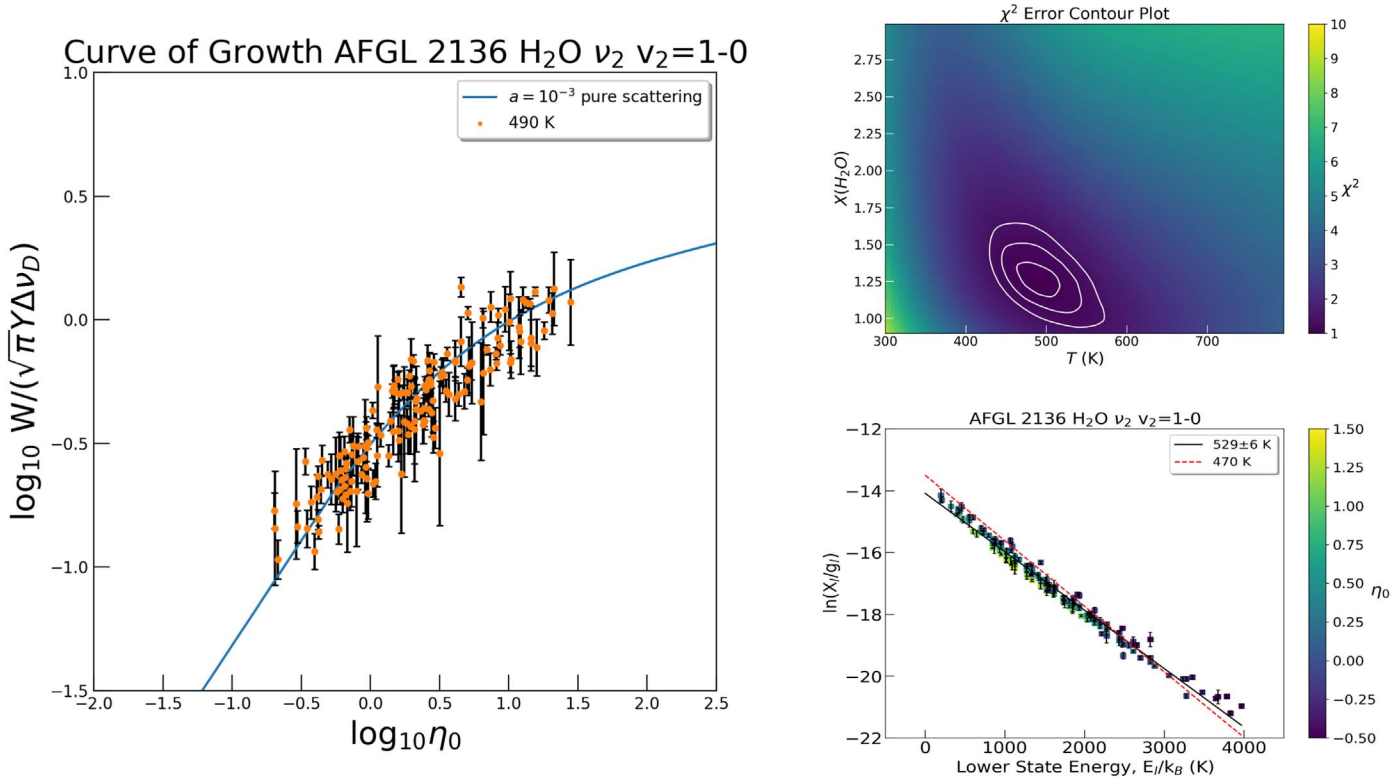

Figure 10. L*eft*: the curve of growth best fit for the case of pure scattering. *Upper right*: the error on the parameters is given in the contour plot where the color scale is the reduced chi-square value. The contours represent the 1σ, 2σ, and 3σ uncertainty levels. The H_2O abundance is quoted relative to CO. *Lower right*: the rotation diagram is a function of η_0 and the abundances for the optically thick lines were determined using the curve of growth. The best-fit temperature of 470 K from Table 2 is represented by the red dashed line. The black solid lines are fits to the corrected data set and the corresponding temperatures are indicated for each case.

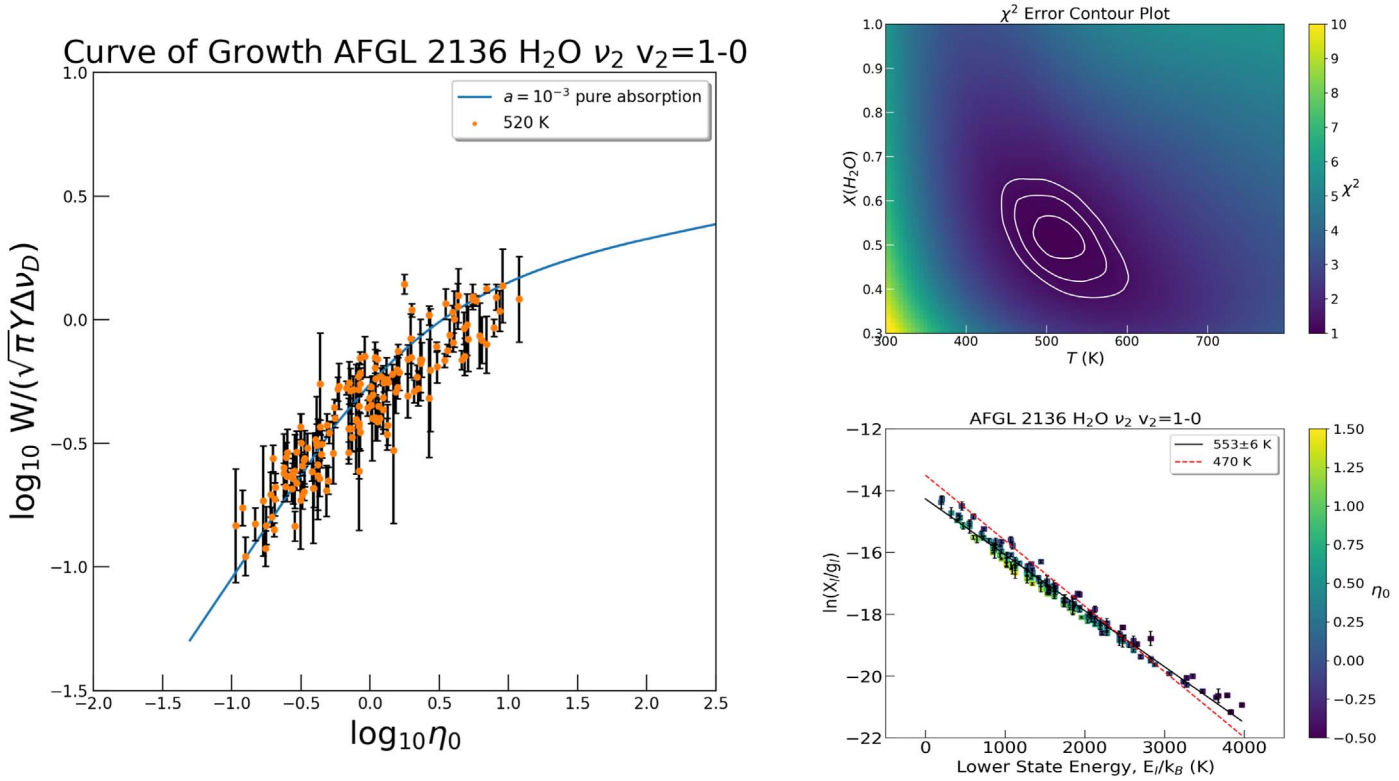

Figure 11. *Left*: the curve of growth best fit for the case of pure absorption in AFGL 2136. *Upper right*: the error on the parameters is given in the contour plot where the color scale is the reduced chi-square value. The contours represent the 1σ, 2σ, and 3σ uncertainty levels. The H_2O abundance is quoted relative to CO. *Lower right*: the rotation diagram is a function of η_0 and the abundances for the optically thick lines were determined using the curve of growth. The best-fit temperature of 470 K from Table 2 is represented by the red dashed line. The black solid lines are fits to the corrected data set and the corresponding temperatures are indicated for each case.

Table 4
Line Parameters for the $v = 1$–0 Transition of AFGL 2136

Transition	λ (μm)	E_l (K)	g_l	g_u	A_{ul} (s^{-1})	v_{LSR} (km s^{-1})	FWHM (km s^{-1})	W (10^8 Hz)	$\log_{10}(\eta_0)$	$\log_{10}(\tau_p)$
$12_{2,11}-11_{1,10}$	5.3719	2194	69	75	10.9	24.1 ± 1.8	11.2 ± 1.2	4.83 ± 0.80	0.57	0.12
$12_{1,11}-11_{2,10}$	5.3737	2194	23	25	10.9	26.1 ± 0.7	7.9 ± 0.7	2.29 ± 0.66	0.09	−0.36
$11_{3,8}-10_{4,7}$	5.3772	2275	63	69	3.3	26.0 ± 2.1	7.5 ± 0.9	1.64 ± 0.84	−0.06	−0.51
$9_{3,7}-8_{2,6}$	5.3806	1414	17	19	5.0	27.2 ± 0.6	12.0 ± 0.5	4.80 ± 0.24	0.36	−0.07
$8_{3,6}-7_{2,5}$	5.4119	1125	45	51	4.3	25.2 ± 0.6	9.6 ± 0.3	5.36 ± 0.35	1.00	0.58
$7_{6,1}-7_{5,2}$	5.4183	1525	45	45	1.3	25.7 ± 1.8	7.9 ± 0.8	1.83 ± 0.74	0.04	−0.39
$9_{3,6}-9_{5,4}$	5.4238	2125	57	57	1.9	26.4 ± 1.9	10.4 ± 1.1	1.82 ± 0.43	−0.23	−0.68
$11_{2,10}-10_{1,9}$	5.4248	1860	21	23	10.2	26.7 ± 1.6	13.7 ± 0.6	5.53 ± 1.06	0.35	−0.09
$7_{3,5}-6_{2,4}$	5.4431	867	13	15	3.9	25.6 ± 1.4	8.8 ± 0.7	3.97 ± 0.80	0.66	0.26
$10_{1,9}-9_{2,8}$	5.4862	1554	19	21	9.5	26.7 ± 0.8	10.0 ± 0.5	4.63 ± 0.42	0.58	0.15
$10_{3,7}-9_{4,6}$	5.4904	1929	19	21	2.6	24.9 ± 0.9	10.6 ± 0.5	1.51 ± 0.31	−0.33	−0.78
$11_{4,7}-10_{5,6}$	5.5031	2473	63	69	1.7	25.4 ± 1.1	8.0 ± 0.6	1.14 ± 0.17	−0.49	−0.95
$9_{2,7}-8_{3,6}$	5.5179	1447	51	57	4.6	24.3 ± 1.4	10.5 ± 0.7	5.24 ± 0.84	0.80	0.37
$11_{1,10}-11_{0,11}$	5.5290	1909	69	69	0.8	25.2 ± 0.9	8.1 ± 0.6	1.60 ± 0.20	−0.30	−0.74
$12_{4,9}-12_{3,10}$	5.5298	2824	75	75	2.2	24.0 ± 0.6	7.2 ± 1.0	1.12 ± 0.59	−0.67	−1.14
$10_{5,6}-10_{4,7}$	5.5496	2275	63	63	2.7	25.2 ± 0.3	10.8 ± 0.8	1.94 ± 0.18	−0.14	−0.59
$8_{5,4}-8_{4,5}$	5.5651	1615	51	51	2.5	25.5 ± 1.1	8.4 ± 0.6	2.65 ± 0.46	0.34	−0.09
$7_{5,3}-7_{4,4}$	5.5670	1335	15	15	2.2	26.0 ± 0.2	9.2 ± 0.6	1.82 ± 0.15	0.02	−0.41
$5_{5,0}-5_{4,1}$	5.5685	878	33	33	1.1	24.1 ± 1.2	8.9 ± 0.6	3.39 ± 0.57	0.49	0.08
$7_{5,2}-7_{4,3}$	5.5775	1340	45	45	2.2	25.0 ± 0.6	9.9 ± 0.4	3.35 ± 0.24	0.50	0.07
$8_{2,7}-7_{1,6}$	5.5836	1013	45	51	7.9	24.4 ± 2.0	12.3 ± 0.8	10.38 ± 0.71	1.40	0.99
$10_{2,9}-10_{1,10}$	5.5870	1603	63	63	1.0	25.3 ± 2.3	8.5 ± 1.1	1.94 ± 0.82	0.03	−0.40
$8_{5,3}-8_{4,4}$	5.5917	1628	17	17	2.6	26.2 ± 0.2	9.4 ± 0.5	1.63 ± 0.11	−0.12	−0.55
$9_{3,6}-8_{4,5}$	5.6118	1615	51	57	2.0	26.0 ± 1.4	10.2 ± 0.8	2.94 ± 1.51	0.31	−0.12
$10_{4,7}-10_{3,8}$	5.6230	2081	63	63	2.8	25.5 ± 0.8	7.6 ± 0.4	1.65 ± 0.21	0.07	−0.38
$9_{2,8}-9_{1,9}$	5.6485	1324	19	19	1.2	26.5 ± 0.2	10.3 ± 0.6	1.71 ± 0.13	−0.13	−0.56
$9_{1,9}-8_{0,8}$	5.6551	1070	17	19	13.2	24.0 ± 1.8	12.3 ± 0.8	7.02 ± 2.01	1.16	0.75
$9_{4,6}-9_{3,7}$	5.6590	1750	19	19	3.0	25.0 ± 0.8	8.8 ± 0.5	1.37 ± 0.62	−0.10	−0.54
$10_{2,8}-10_{1,9}$	5.6645	1860	21	21	2.1	26.1 ± 0.2	8.3 ± 0.6	1.17 ± 0.11	−0.32	−0.76
$8_{4,5}-8_{3,6}$	5.6864	1447	51	51	3.1	24.9 ± 0.7	11.3 ± 0.4	5.45 ± 0.34	0.63	0.20
$7_{4,4}-7_{3,5}$	5.7051	1175	15	15	3.1	24.9 ± 1.1	8.7 ± 0.7	2.84 ± 0.38	0.35	−0.07
$11_{3,8}-11_{2,9}$	5.7131	2432	69	69	3.2	28.7 ± 0.2	10.7 ± 0.5	1.95 ± 0.11	−0.14	−0.60
$6_{4,3}-6_{3,4}$	5.7162	933	39	39	2.9	24.5 ± 4.0	10.2 ± 0.6	4.68 ± 0.71	0.96	0.55
$5_{4,2}-5_{5,3}$	5.7217	725	11	11	2.4	24.6 ± 1.1	10.1 ± 0.4	4.61 ± 0.79	0.53	0.12
$10_{4,7}-9_{5,4}$	5.7233	2125	57	63	1.2	26.0 ± 0.2	8.2 ± 0.4	1.03 ± 0.07	−0.33	−0.78
$8_{1,7}-8_{0,8}$	5.7264	1070	17	17	1.4	24.1 ± 1.0	9.6 ± 0.7	2.53 ± 0.27	0.16	−0.25
$4_{4,0}-4_{3,1}$	5.7281	552	9	9	1.6	24.5 ± 0.9	9.5 ± 0.6	2.67 ± 1.30	0.43	0.03
$8_{3,6}-8_{2,7}$	5.7320	1274	51	51	2.7	25.2 ± 2.0	10.8 ± 0.9	6.04 ± 1.39	0.73	0.31
$9_{2,7}-9_{1,8}$	5.7494	1552	57	57	2.6	24.6 ± 1.6	9.9 ± 0.8	3.11 ± 0.70	0.51	0.08
$6_{4,2}-6_{3,3}$	5.7550	951	13	13	3.2	24.7 ± 1.5	10.1 ± 0.8	4.13 ± 0.70	0.51	0.10
$7_{2,6}-7_{1,7}$	5.7735	843	15	15	1.7	25.6 ± 0.7	11.5 ± 0.4	4.99 ± 0.30	0.41	−0.01
$7_{3,5}-7_{2,6}$	5.7792	1021	15	15	3.1	24.9 ± 1.7	11.4 ± 1.0	5.00 ± 0.73	0.50	0.09
$10_{3,7}-10_{2,8}$	5.7995	2069	21	21	4.1	27.5 ± 0.3	8.7 ± 0.8	1.46 ± 0.17	−0.19	−0.64
$7_{1,6}-7_{0,7}$	5.8022	843	45	45	1.8	25.0 ± 1.2	12.4 ± 0.7	7.38 ± 0.66	0.91	0.50
$11_{4,7}-11_{3,8}$	5.8050	2609	69	69	5.3	24.7 ± 0.7	9.2 ± 0.5	2.23 ± 0.19	−0.06	−0.52
$8_{4,4}-8_{3,5}$	5.8088	1511	17	17	4.5	26.0 ± 0.9	11.3 ± 0.5	3.65 ± 0.77	0.28	−0.15
$9_{4,5}-9_{3,6}$	5.8280	1846	57	57	5.2	25.6 ± 0.8	8.2 ± 0.9	2.08 ± 1.40	0.56	0.12
$10_{4,6}-10_{3,7}$	5.8289	2213	21	21	5.6	27.6 ± 0.3	8.4 ± 0.9	1.03 ± 0.14	−0.18	−0.64
$6_{2,5}-6_{1,6}$	5.8342	643	39	39	2.1	24.0 ± 1.8	10.9 ± 0.7	7.07 ± 1.85	1.11	0.71
$8_{2,6}-8_{1,7}$	5.8380	1270	17	17	3.3	25.1 ± 1.0	9.9 ± 0.6	3.87 ± 0.38	0.37	−0.05
$6_{2,4}-5_{3,3}$	5.8575	725	11	13	1.8	24.2 ± 0.8	9.4 ± 0.6	3.75 ± 0.33	0.50	0.10
$8_{4,5}-7_{5,2}$	5.8656	1525	45	51	0.9	25.9 ± 1.1	9.8 ± 0.7	2.21 ± 0.96	0.03	−0.40
$9_{3,6}-9_{2,7}$	5.8729	1729	57	57	5.2	25.0 ± 1.3	10.3 ± 0.6	4.82 ± 0.66	0.67	0.24
$8_{3,6}-7_{4,3}$	5.8860	1340	45	51	1.0	24.9 ± 1.2	8.8 ± 0.5	2.52 ± 0.72	0.28	−0.14
$5_{2,4}-5_{1,5}$	5.8909	470	11	11	2.5	25.6 ± 1.8	13.1 ± 0.7	7.47 ± 1.87	0.82	0.42
$7_{2,5}-7_{1,6}$	5.9228	1013	45	45	4.4	24.5 ± 2.0	10.4 ± 0.8	5.75 ± 1.73	1.17	0.76
$8_{3,5}-8_{2,6}$	5.9246	1414	17	17	6.1	24.5 ± 1.8	9.0 ± 0.9	3.33 ± 0.99	0.53	0.10
$7_{4,3}-6_{5,2}$	5.9399	1278	39	45	0.6	25.1 ± 1.4	8.8 ± 0.7	2.13 ± 0.42	0.05	−0.37
$7_{3,5}-6_{4,2}$	5.9447	1090	13	15	0.9	25.8 ± 3.0	12.5 ± 1.5	2.17 ± 0.59	−0.04	−0.46
$7_{3,4}-7_{2,5}$	5.9507	1125	45	45	6.5	24.5 ± 1.5	9.7 ± 0.6	5.90 ± 1.79	1.25	0.83
$6_{3,3}-6_{2,4}$	5.9530	867	13	13	6.0	24.5 ± 2.0	10.1 ± 0.8	4.28 ± 2.45	0.91	0.50
$6_{3,3}-5_{4,2}$	5.9792	878	11	13	0.8	25.7 ± 1.1	10.0 ± 0.6	1.87 ± 0.49	0.01	−0.41
$6_{3,4}-5_{4,1}$	6.0191	878	33	39	0.7	24.0 ± 0.5	7.1 ± 0.2	2.96 ± 0.22	0.46	0.05

Table 4
(Continued)

Transition	λ (μm)	E_l (K)	g_l	g_u	A_{ul} (s^{-1})	v_{LSR} (km s^{-1})	FWHM (km s^{-1})	W (10^8 Hz)	$\log_{10}(\eta_0)$	$\log_{10}(\tau_p)$
$7_{2,6}-6_{3,3}$	6.0350	951	13	15	0.6	25.2 ± 0.3	10.0 ± 0.8	1.59 ± 0.17	−0.09	−0.50
$6_{4,3}-5_{5,0}$	6.0375	1067	33	39	0.3	25.2 ± 2.6	14.0 ± 1.4	1.94 ± 0.43	−0.14	−0.55
$5_{3,2}-4_{4,1}$	6.0887	702	27	33	0.4	25.7 ± 1.2	12.0 ± 0.6	3.56 ± 0.76	0.27	−0.14
$5_{2,4}-4_{3,1}$	6.0964	552	9	11	0.7	24.4 ± 0.7	9.3 ± 0.4	2.63 ± 0.22	0.25	−0.15
$4_{2,2}-3_{3,1}$	6.1062	410	7	9	0.5	24.1 ± 0.6	8.9 ± 0.4	2.42 ± 0.16	0.16	−0.24
$4_{2,3}-3_{3,0}$	6.1630	410	21	27	0.4	24.7 ± 0.8	10.1 ± 0.5	4.50 ± 0.35	0.57	0.18
$4_{4,1}-5_{3,2}$	6.1698	732	33	27	0.2	24.0 ± 0.3	8.9 ± 0.5	1.37 ± 0.12	−0.12	−0.52
$3_{3,0}-4_{2,3}$	6.2218	432	27	21	0.3	24.6 ± 1.2	10.6 ± 0.7	3.35 ± 0.38	0.28	−0.11
$3_{1,3}-2_{2,0}$	6.2371	195	5	7	0.4	24.0 ± 3.4	12.5 ± 1.4	3.64 ± 0.55	0.18	−0.21
$5_{4,1}-6_{3,4}$	6.2388	933	39	33	0.3	27.2 ± 0.2	9.8 ± 0.5	2.09 ± 0.13	0.08	−0.33
$2_{2,0}-3_{1,3}$	6.2453	204	7	6	0.4	24.0 ± 1.1	7.7 ± 0.6	1.45 ± 0.34	−0.02	−0.41
$3_{2,1}-4_{1,4}$	6.2716	323	27	21	0.3	24.0 ± 1.8	9.6 ± 0.8	2.83 ± 1.13	0.45	0.06
$3_{3,1}-4_{2,2}$	6.2827	454	9	7	0.4	25.3 ± 2.5	9.0 ± 1.4	1.59 ± 0.50	−0.11	−0.50
$4_{3,1}-5_{2,4}$	6.2905	598	11	9	0.5	25.9 ± 1.4	8.8 ± 0.7	1.84 ± 0.36	−0.03	−0.43
$5_{3,2}-6_{2,5}$	6.3388	795	39	33	0.5	25.3 ± 1.2	9.9 ± 0.7	3.25 ± 0.42	0.37	−0.04
$7_{4,3}-8_{3,6}$	6.3856	1447	51	45	0.5	24.0 ± 1.5	12.2 ± 1.1	2.28 ± 0.27	−0.08	−0.50
$6_{2,4}-6_{3,3}$	6.4531	951	13	13	11.3	24.2 ± 1.0	14.1 ± 0.3	7.35 ± 0.39	1.21	0.80
$13_{4,9}-13_{5,8}$	6.4737	3783	81	81	15.0	25.3 ± 0.3	8.9 ± 0.9	1.66 ± 0.21	−0.48	−0.98
$9_{3,6}-9_{4,5}$	6.4749	1957	57	57	12.7	24.4 ± 0.9	13.4 ± 0.6	6.48 ± 0.43	0.98	0.54
$3_{2,2}-4_{1,3}$	6.5007	396	9	7	2.3	24.3 ± 0.9	12.8 ± 0.9	8.38 ± 0.77	0.77	0.37
$11_{4,7}-11_{5,6}$	6.5067	2876	69	69	12.6	25.2 ± 1.2	14.1 ± 0.5	3.54 ± 0.24	0.22	−0.26
$9_{2,7}-9_{3,6}$	6.5126	1846	57	57	12.2	24.0 ± 1.7	11.1 ± 0.8	4.26 ± 0.74	1.07	0.63
$7_{3,4}-7_{4,3}$	6.5290	1340	45	45	9.5	24.3 ± 0.9	11.2 ± 0.7	5.55 ± 0.45	1.33	0.91
$13_{5,8}-13_{6,7}$	6.5392	3966	81	81	12.5	25.7 ± 0.4	8.0 ± 1.0	1.04 ± 0.17	−0.72	−1.22
$10_{4,6}-10_{5,5}$	6.5401	2482	21	21	11.1	25.9 ± 0.7	9.1 ± 1.7	1.21 ± 0.29	0.02	−0.44
$7_{1,6}-7_{2,5}$	6.5474	1125	45	45	9.5	24.5 ± 3.4	14.1 ± 1.3	7.20 ± 2.86	1.53	1.12
$7_{4,4}-8_{3,5}$	6.5818	1511	17	15	0.9	24.7 ± 0.5	10.1 ± 1.3	0.70 ± 0.12	−0.33	−0.76
$13_{3,10}-13_{4,9}$	6.5832	3646	81	81	13.2	25.6 ± 0.2	9.1 ± 0.7	1.41 ± 0.14	−0.39	−0.89
$6_{3,4}-6_{4,3}$	6.6007	1088	39	39	7.5	24.6 ± 3.0	14.1 ± 0.5	8.05 ± 2.75	1.42	1.00
$11_{2,9}-11_{3,8}$	6.6594	2609	69	69	10.7	26.1 ± 0.9	10.5 ± 0.6	3.23 ± 0.28	0.42	−0.04
$9_{3,7}-9_{4,6}$	6.6642	1929	19	19	9.4	24.8 ± 1.4	8.0 ± 0.9	2.24 ± 0.40	0.44	−0.01
$12_{4,9}-12_{5,8}$	6.6867	3274	75	75	10.9	25.6 ± 1.1	7.4 ± 0.6	1.20 ± 0.21	−0.14	−0.63
$10_{3,8}-10_{4,7}$	6.7052	2275	63	63	9.6	24.6 ± 2.3	12.7 ± 1.1	4.04 ± 0.76	0.65	0.20
$6_{3,4}-7_{2,5}$	6.7146	1125	45	39	2.0	25.0 ± 2.4	9.8 ± 1.0	3.95 ± 1.49	0.82	0.40
$8_{2,7}-8_{3,6}$	6.7157	1447	51	51	7.7	24.2 ± 2.4	12.0 ± 1.2	4.74 ± 1.03	1.23	0.81
$9_{1,8}-9_{2,7}$	6.7288	1729	57	57	7.9	24.8 ± 2.3	13.6 ± 1.3	6.48 ± 1.37	1.04	0.60
$7_{0,7}-7_{1,6}$	6.7731	1013	45	45	4.7	24.7 ± 1.6	12.9 ± 1.0	6.99 ± 0.83	1.38	0.97
$9_{2,8}-9_{3,7}$	6.7826	1750	19	19	7.5	24.6 ± 1.4	8.8 ± 0.8	2.12 ± 0.40	0.53	0.09
$7_{1,7}-7_{2,6}$	6.7959	1021	15	15	4.6	24.0 ± 0.9	8.1 ± 1.1	2.71 ± 1.49	0.89	0.48
$12_{3,10}-12_{4,9}$	6.8144	3058	75	75	9.6	25.8 ± 0.2	10.7 ± 0.7	2.48 ± 0.19	0.03	−0.45
$10_{1,9}-10_{2,8}$	6.8251	2069	21	21	7.6	26.5 ± 0.2	11.8 ± 0.6	2.93 ± 0.19	0.29	−0.16
$13_{2,11}-13_{3,10}$	6.8382	3475	81	81	9.8	26.1 ± 0.4	9.8 ± 1.0	1.36 ± 0.17	−0.31	−0.80
$4_{1,3}-5_{2,4}$	6.8528	598	11	9	6.0	24.2 ± 1.8	11.3 ± 1.1	5.14 ± 0.77	1.18	0.78
$6_{0,6}-7_{1,7}$	6.8714	843	15	13	8.1	24.9 ± 0.6	13.8 ± 0.5	6.63 ± 0.32	1.25	0.84
$8_{1,8}-8_{2,7}$	6.8867	1274	51	51	4.4	25.2 ± 1.7	14.1 ± 1.0	6.85 ± 0.80	1.18	0.76
$11_{1,10}-11_{2,9}$	6.9199	2432	69	69	7.3	25.3 ± 0.3	13.1 ± 0.7	3.06 ± 0.22	0.47	0.01
$11_{2,10}-11_{3,9}$	6.9380	2439	23	23	7.2	25.8 ± 1.1	8.9 ± 0.7	1.56 ± 0.20	−0.01	−0.47
$7_{1,7}-8_{0,8}$	6.9588	1070	17	15	7.8	25.8 ± 3.5	13.6 ± 1.7	6.83 ± 1.72	1.10	0.69
$7_{2,6}-8_{1,7}$	6.9655	1270	17	15	5.7	25.1 ± 0.3	10.8 ± 1.1	3.19 ± 0.37	0.78	0.36
$9_{0,9}-9_{1,8}$	6.9774	1552	57	57	4.2	24.0 ± 0.5	9.9 ± 0.4	4.08 ± 0.22	0.98	0.55
$9_{1,9}-9_{2,8}$	6.9833	1554	19	19	4.2	27.1 ± 0.3	13.3 ± 0.9	3.20 ± 0.25	0.50	0.07
$8_{3,6}-9_{2,7}$	7.0015	1729	57	51	3.4	25.7 ± 1.5	9.6 ± 0.8	2.65 ± 0.54	0.68	0.24
$7_{1,6}-8_{2,7}$	7.0218	1274	51	45	5.9	24.5 ± 2.4	10.8 ± 1.2	4.27 ± 1.13	1.28	0.86
$12_{2,11}-12_{3,10}$	7.0231	2824	75	75	7.1	24.4 ± 0.8	8.6 ± 0.6	1.56 ± 0.16	0.15	−0.32
$8_{0,8}-9_{1,9}$	7.0559	1324	19	17	7.4	24.0 ± 0.4	10.5 ± 0.3	4.15 ± 0.19	0.92	0.50
$8_{2,7}-9_{1,8}$	7.0617	1552	57	51	5.8	24.0 ± 1.0	11.6 ± 0.7	3.66 ± 0.32	1.08	0.65
$10_{0,10}-10_{1,9}$	7.0818	1860	21	21	4.1	24.3 ± 1.4	10.7 ± 0.9	1.78 ± 0.23	0.26	−0.18
$10_{1,10}-10_{2,9}$	7.0846	1861	63	63	4.1	24.6 ± 1.9	11.7 ± 1.2	2.80 ± 0.46	0.74	0.30
$10_{4,7}-11_{3,8}$	7.0855	2609	69	63	2.2	25.1 ± 2.2	7.9 ± 1.2	1.29 ± 0.45	−0.22	−0.68
$8_{1,7}-9_{2,8}$	7.0924	1554	19	17	5.9	24.1 ± 1.1	10.5 ± 0.7	2.82 ± 0.30	0.61	0.18
$13_{1,12}-13_{2,11}$	7.1065	3233	81	81	7.0	25.8 ± 0.4	9.4 ± 1.1	1.59 ± 0.23	−0.18	−0.67
$9_{3,7}-10_{2,8}$	7.1252	2069	21	19	4.0	24.5 ± 1.2	10.1 ± 0.8	1.65 ± 0.21	0.02	−0.43
$9_{2,8}-10_{1,9}$	7.1552	1860	21	19	5.8	25.9 ± 0.7	9.8 ± 0.4	2.52 ± 0.18	0.38	−0.06

Table 4
(Continued)

Transition	λ (μm)	E_l (K)	g_l	g_u	A_{ul} (s^{-1})	v_{LSR} (km s^{-1})	FWHM (km s^{-1})	W (10^8 Hz)	$\log_{10}(\eta_0)$	$\log_{10}(\tau_p)$
$11_{0,11}-11_{1,10}$	7.1889	2194	69	69	4.0	24.7 ± 1.3	10.1 ± 0.5	2.98 ± 0.61	0.48	0.03
$14_{2,13}-14_{3,12}$	7.2028	3671	87	87	6.9	25.9 ± 2.8	7.9 ± 1.3	0.96 ± 0.49	−0.54	−1.04
$10_{3,8}-11_{2,9}$	7.2356	2432	69	63	4.3	25.4 ± 3.9	8.7 ± 2.2	1.26 ± 0.69	0.26	−0.20
$9_{2,7}-10_{3,8}$	7.2872	2081	63	57	4.5	25.1 ± 1.4	11.9 ± 0.9	3.21 ± 0.39	0.57	0.12
$12_{1,12}-12_{2,11}$	7.3002	2554	75	75	3.9	24.0 ± 2.9	9.4 ± 0.8	1.84 ± 0.39	0.20	−0.27
$11_{2,9}-12_{3,10}$	7.3945	2824	75	69	4.6	26.8 ± 0.3	10.7 ± 0.9	1.87 ± 0.20	−0.01	−0.48
$3_{0,3}-4_{3,2}$	7.4108	550	27	21	0.2	26.3 ± 0.4	8.9 ± 1.2	1.13 ± 0.19	0.14	−0.26
$7_{3,4}-8_{4,5}$	7.4618	1615	51	45	5.2	24.1 ± 1.6	11.5 ± 1.1	4.26 ± 0.63	0.99	0.56
$6_{4,2}-7_{5,3}$	7.4654	1524	15	13	9.2	24.0 ± 2.3	10.1 ± 1.2	3.27 ± 0.89	0.78	0.35
$6_{4,3}-7_{5,2}$	7.4708	1525	45	39	9.2	27.7 ± 0.2	15.0 ± 0.5	6.57 ± 0.26	1.26	0.83
$8_{3,5}-9_{4,6}$	7.5193	1929	19	17	4.4	26.2 ± 0.2	12.4 ± 0.6	2.57 ± 0.16	0.21	−0.23
$13_{1,12}-14_{2,13}$	7.5407	3350	87	81	5.1	26.3 ± 0.4	10.4 ± 1.2	1.35 ± 0.19	−0.35	−0.83
$9_{3,6}-10_{4,7}$	7.5567	2275	63	57	3.9	24.4 ± 1.4	11.5 ± 0.9	2.39 ± 0.30	0.38	−0.08
$10_{3,7}-11_{4,8}$	7.5802	2652	23	21	3.7	24.5 ± 0.8	7.1 ± 0.0	0.71 ± 0.12	−0.43	−0.89
$7_{4,3}-8_{5,4}$	7.5932	1806	51	45	7.5	24.4 ± 0.9	11.2 ± 0.7	3.88 ± 0.34	1.00	0.56
$7_{4,4}-8_{5,3}$	7.6127	1807	17	15	7.4	24.7 ± 1.0	7.8 ± 0.6	1.64 ± 0.24	0.52	0.08
$7_{5,2}-8_{6,3}$	7.6187	2031	51	45	10.1	24.4 ± 1.6	13.9 ± 1.5	5.53 ± 0.79	0.92	0.48
$7_{5,3}-8_{6,2}$	7.6196	2031	17	15	10.1	24.0 ± 0.4	7.1 ± 0.2	1.91 ± 0.15	0.44	−0.01
$7_{3,5}-8_{4,4}$	7.6442	1628	17	15	4.3	25.0 ± 1.8	9.9 ± 1.0	1.91 ± 0.41	0.45	0.02
$8_{4,4}-9_{5,5}$	7.7118	2122	19	17	6.2	26.0 ± 2.0	13.5 ± 0.9	2.60 ± 0.51	0.22	−0.23
$8_{4,5}-9_{5,4}$	7.7676	2125	57	51	6.0	25.1 ± 1.0	10.7 ± 0.6	2.38 ± 0.25	0.69	0.24
$9_{4,5}-10_{5,6}$	7.8122	2473	63	57	5.1	25.2 ± 2.6	10.1 ± 1.1	1.84 ± 0.73	0.35	−0.11
$15_{0,15}-16_{1,16}$	7.8331	3829	99	93	5.1	25.1 ± 0.4	8.0 ± 1.1	0.51 ± 0.09	−0.69	−1.19
$9_{5,5}-10_{6,4}$	7.9113	2698	21	19	7.1	24.0 ± 0.4	9.6 ± 1.0	0.88 ± 0.11	−0.17	−0.64
$11_{4,7}-12_{5,8}$	7.9334	3274	75	69	3.7	25.0 ± 1.2	8.3 ± 0.8	0.84 ± 0.13	−0.42	−0.91
$6_{1,6}-7_{2,5}$	7.9343	1125	45	39	0.4	24.7 ± 1.6	9.9 ± 0.7	1.71 ± 0.44	0.37	−0.04
$9_{4,6}-10_{5,5}$	7.9452	2482	21	19	4.7	27.3 ± 0.2	10.2 ± 0.6	0.90 ± 0.07	−0.14	−0.60

Note. E_l is the energy of the lower level of the transition, g_l and g_u are the statistical weights of the lower and upper levels, respectively, A_{ul} is the Einstein A coefficient of the transition, v_{LSR} is the peak velocity of the line, FWHM is the full width at half maximum of the line, W is the equivalent width in units of hertz, and τ_p is the peak optical depth of the transition. η_0 is the opacity in the lower level of the transition calculated for $\epsilon = 0.5$. Line data were taken from the HITRAN database (Gordon et al. 2017).

(This table is available in machine-readable form.)

In the $v_2 = 2$–1 band of AFGL 2591, the rotation diagram suggests that these lines are also optically thick with $\log_{10}(\eta_0)$ approaching 1. This is confirmed by the fact that there is an overall increase in the line width with η_0. We therefore carry out a curve of growth analysis using the stellar atmosphere model on this band as well to determine the physical conditions. The results are shown in Figure 20. There is no evidence for a velocity trend with opacity in this band and an average value of -10.2 ± 0.4 km s^{-1} is derived for v_{LSR}. We derive a vibrational temperature of 504 ± 61 K, for $\sigma_v = 2$ km s^{-1}. We did not consider $H_2{}^{18}O$ detected in our spectra of AFGL 2591. Two lines are present however and were blended with other source lines, and most strong lines that should have been detected were not. All line parameters for the $v = 1$–0 and $v = 2$–1 band are given in Table 7 and Table 8 respectively. As for AFGL 2136, the similarity in vibrational and rotational excitation temperature implies very high densities, 10^{11} cm^{-3}, and that the kinetic temperature of gas is equal to the excitation temperature of the rotational population, ∼500 K.

The H_2O line profiles agree well with those of the other molecules in this source. In a previous analysis, all species were fit with only one Gaussian, assuming that absorption originated from one velocity component (Barr et al. 2020). A number of H_2O lines clearly reveal the presence of two velocity components, which is not obvious in the other molecules. If the other species were fit with two velocity components instead of one, the equivalent width of the lines would be lower and thus the abundances calculated would be reduced. We find that this is only a small effect, however, not more than a factor of 1.3. The HCN opacities are of the order of the optically thin H_2O lines. This is reflected in the rotation diagram where the data lie along a straight line indicative of optically thin gas in LTE. Therefore, the HCN lines could not have broadened after saturating at nonzero flux.

5. Discussion

We have presented two scenarios to explain the absorption line data obtained from the spectral survey—absorption by foreground material and absorption in a disk atmosphere—that can both provide reasonable fits to the observed behavior of the equivalent width of the H_2O lines (Sections 5.1 and 5.2). Here, we will place each of these interpretations within the context of these sources and assess their relative merits and challenges. Summarizing the observational characteristics of these two sources that have to be accounted for (1) the presence of absorption rather than emission lines with nonzero saturated lines, which are narrow (∼10 km s^{-1}) and offset from the systemic velocity. In addition, for AFGL 2591, the peak velocity reveals a systematic shift with increasing line opacity. (2) The derived excitation temperatures and column densities/abundances and their variations with wavelength (Table 2). (3)

Table 5
Line Parameters for the $v = 2$–1 Transition of AFGL 2136

Transition	λ (μm)	E_l (K)	g_l	g_u	A_{ul} (s^{-1})	v_{LSR} (km s^{-1})	FWHM (km s^{-1})	W (10^8 Hz)	$\log_{10}(\eta_0)$	$\log_{10}(\tau_p)$
$4_{4,1}-3_{3,0}$	5.4373	2745	21	27	9.8	27.5 ± 1.2	7.1 ± 3.2	1.11 ± 0.55	−0.20	−0.54
$5_{3,2}-4_{2,3}$	5.5105	2745	27	33	6.2	24.0 ± 0.5	7.1 ± 0.5	0.73 ± 0.10	−0.31	−0.66
$6_{3,4}-5_{2,3}$	5.5218	2955	33	39	6.9	26.6 ± 0.4	9.5 ± 1.1	1.04 ± 0.15	−0.37	−0.71
$11_{0,11}-10_{1,10}$	5.6670	3892	63	69	27.6	27.2 ± 0.2	9.9 ± 0.6	1.18 ± 0.09	−0.32	−0.65
$3_{3,0}-2_{2,1}$	5.6872	2507	15	21	10.9	24.9 ± 1.0	9.5 ± 1.3	1.86 ± 0.30	−0.01	−0.36
$10_{1,10}-9_{0,9}$	5.7202	3615	57	63	26.5	26.3 ± 0.4	10.4 ± 1.1	1.64 ± 0.22	−0.13	−0.45
$6_{2,5}-5_{1,4}$	5.7627	2879	33	39	10.9	25.5 ± 1.4	11.9 ± 3.2	2.61 ± 1.01	−0.06	−0.40
$9_{0,9}-8_{1,8}$	5.7769	3364	51	57	25.2	27.0 ± 1.0	11.0 ± 2.8	2.83 ± 0.75	0.04	−0.29
$7_{1,6}-6_{2,5}$	5.8206	3110	39	45	11.8	26.4 ± 0.4	11.9 ± 1.1	1.54 ± 0.18	−0.14	−0.48
$8_{1,8}-7_{0,7}$	5.8322	3138	45	51	23.9	27.4 ± 0.2	10.7 ± 0.7	3.64 ± 0.28	0.18	−0.16
$7_{1,6}-7_{0,7}$	5.8869	3138	45	45	3.7	26.0 ± 0.8	7.1 ± 2.2	0.90 ± 0.34	−0.68	−1.02
$7_{1,7}-6_{0,6}$	5.8902	2938	13	15	22.4	25.2 ± 1.3	7.3 ± 2.3	1.15 ± 0.42	−0.19	−0.5
$6_{1,6}-5_{0,5}$	5.9485	2764	33	39	20.7	25.7 ± 0.7	11.4 ± 0.7	4.25 ± 0.32	0.36	0.01
$6_{0,6}-5_{1,5}$	5.9622	2767	11	13	20.6	25.1 ± 4.6	10.2 ± 9.2	1.58 ± 1.82	−0.12	−0.47
$4_{2,3}-4_{1,4}$	6.0224	2621	27	27	5.9	25.0 ± 1.3	7.8 ± 2.2	1.09 ± 0.36	−0.21	−0.56
$7_{2,5}-7_{1,6}$	6.0322	3323	45	45	9.4	26.7 ± 0.3	9.2 ± 0.7	1.04 ± 0.10	−0.38	−0.72
$4_{1,4}-3_{0,3}$	6.0613	2492	21	27	16.7	24.7 ± 0.8	10.1 ± 0.9	2.88 ± 0.33	0.36	0.01
$5_{1,4}-5_{0,5}$	6.0802	2764	33	33	6.4	26.5 ± 0.2	11.7 ± 0.6	1.99 ± 0.12	−0.20	−0.54
$2_{2,1}-2_{1,2}$	6.1010	2413	15	15	5.9	26.0 ± 0.3	10.0 ± 0.7	1.16 ± 0.11	−0.26	−0.62
$3_{2,1}-3_{1,2}$	6.1716	2550	21	21	12.5	25.8 ± 2.5	8.7 ± 3.8	1.56 ± 0.95	0.11	−0.24
$2_{1,2}-1_{0,1}$	6.1753	2329	9	15	13.9	26.1 ± 0.8	10.4 ± 0.2	2.65 ± 0.25	0.19	−0.16
$3_{0,3}-2_{1,2}$	6.2028	2413	15	21	11.9	25.0 ± 0.5	8.0 ± 0.7	1.78 ± 0.19	0.21	−0.15
$1_{1,0}-1_{0,1}$	6.3157	2329	9	9	21.3	25.4 ± 0.5	7.1 ± 0.9	1.55 ± 0.29	0.19	−0.17
$1_{0,1}-1_{1,0}$	6.5149	2360	9	9	24.9	26.7 ± 0.2	10.5 ± 0.6	2.19 ± 0.17	0.27	−0.08
$3_{1,2}-3_{2,1}$	6.5994	2618	21	21	19.1	24.0 ± 1.0	12.8 ± 1.5	3.49 ± 0.46	0.33	−0.02
$5_{1,4}-5_{2,3}$	6.6160	2955	33	33	23.3	25.1 ± 1.5	11.1 ± 1.7	3.00 ± 0.63	0.32	−0.02
$2_{1,2}-3_{0,3}$	6.6400	2492	21	15	13.5	24.5 ± 2.0	9.8 ± 3.3	1.76 ± 0.67	0.13	−0.22
$7_{2,5}-7_{3,4}$	6.6462	3544	45	45	24.4	25.9 ± 0.3	8.4 ± 0.7	1.49 ± 0.16	−0.01	−0.35
$6_{2,4}-6_{3,3}$	6.6574	3284	13	13	21.6	26.6 ± 0.3	11.0 ± 1.3	0.88 ± 0.12	−0.38	−0.72
$4_{0,4}-4_{1,3}$	6.6674	2698	9	9	15.1	25.0 ± 1.0	7.4 ± 1.9	0.86 ± 0.26	−0.21	−0.56
$1_{0,1}-2_{1,2}$	6.6739	2413	15	9	22.9	26.2 ± 0.2	10.4 ± 0.7	2.32 ± 0.19	0.22	−0.14
$9_{3,6}-9_{4,5}$	6.6888	4315	57	57	23.9	24.4 ± 2.7	8.7 ± 1.9	0.69 ± 0.24	−0.56	−0.88
$9_{2,7}-9_{3,6}$	6.6895	4180	57	57	25.5	24.5 ± 1.2	8.4 ± 1.6	0.84 ± 0.20	−0.43	−0.75
$7_{1,6}-7_{2,5}$	6.7261	3443	45	45	20.3	24.2 ± 0.9	7.2 ± 1.8	1.02 ± 0.29	−0.01	−0.34
$3_{2,1}-3_{3,0}$	6.7334	2745	21	21	9.2	27.7 ± 0.6	13.1 ± 2.0	1.33 ± 0.25	−0.06	−0.40
$5_{0,5}-5_{1,4}$	6.7653	2879	33	33	12.5	26.5 ± 0.2	11.3 ± 0.7	2.33 ± 0.18	0.14	−0.21
$4_{1,4}-4_{2,3}$	6.7857	2745	27	27	11.2	24.8 ± 0.4	9.9 ± 1.1	1.28 ± 0.18	0.13	−0.22
$5_{3,2}-5_{4,1}$	6.7987	3240	33	33	12.1	25.6 ± 0.4	10.3 ± 1.2	1.39 ± 0.20	−0.13	−0.47
$3_{0,3}-4_{1,4}$	6.8136	2621	27	21	17.1	25.3 ± 0.3	13.2 ± 0.9	2.98 ± 0.25	0.31	−0.04
$6_{2,5}-6_{3,4}$	6.8285	3269	39	39	15.4	26.7 ± 0.5	11.6 ± 1.3	1.86 ± 0.26	0.01	−0.33
$4_{1,4}-5_{0,5}$	6.8449	2764	33	27	16.0	25.5 ± 0.5	8.7 ± 1.2	2.17 ± 0.34	0.27	−0.08
$1_{1,0}-2_{2,1}$	6.8512	2507	15	9	26.0	26.4 ± 0.3	12.1 ± 0.8	2.75 ± 0.23	0.24	−0.11
$3_{1,2}-4_{2,3}$	7.0096	2745	27	21	13.2	24.3 ± 1.1	9.6 ± 1.6	1.79 ± 0.34	0.13	−0.21
$6_{1,6}-7_{0,7}$	7.0362	3138	45	39	15.7	24.7 ± 0.6	10.1 ± 1.2	2.15 ± 0.28	0.13	−0.21
$2_{2,1}-3_{3,0}$	7.0996	2745	21	15	26.7	24.3 ± 0.5	7.1 ± 0.9	1.39 ± 0.29	0.33	−0.02
$5_{1,4}-6_{2,5}$	7.1217	3110	39	33	11.1	26.0 ± 2.0	7.6 ± 5.4	1.08 ± 0.85	−0.04	−0.38
$7_{1,7}-8_{0,8}$	7.1324	3363	17	15	15.1	24.3 ± 1.6	7.6 ± 2.0	0.84 ± 0.33	−0.48	−0.82
$7_{0,7}-8_{1,8}$	7.1381	3364	51	45	15.1	26.0 ± 1.5	9.4 ± 2.7	1.33 ± 0.43	−0.01	−0.34
$3_{2,1}-4_{3,2}$	7.2050	2885	27	21	18.3	25.3 ± 1.2	13.3 ± 4.0	2.89 ± 0.89	0.21	−0.13
$7_{1,6}-8_{2,7}$	7.2245	3590	51	45	11.1	25.7 ± 4.8	9.2 ± 6.2	0.82 ± 0.78	−0.30	−0.63
$8_{1,8}-9_{0,9}$	7.2308	3615	57	51	14.5	26.4 ± 1.4	10.4 ± 1.4	1.75 ± 0.32	−0.17	−0.50
$3_{3,0}-4_{4,1}$	7.2937	3064	27	21	28.4	26.8 ± 0.9	13.8 ± 1.5	3.05 ± 0.37	0.29	−0.06
$4_{3,2}-5_{4,1}$	7.4294	3240	33	27	20.9	26.1 ± 0.3	11.4 ± 0.9	1.83 ± 0.18	0.13	−0.21
$5_{3,2}-6_{4,3}$	7.5509	3451	39	33	16.2	24.5 ± 2.3	7.9 ± 3.0	0.69 ± 0.32	−0.05	−0.39
$6_{3,4}-7_{4,3}$	7.7350	3701	45	39	12.3	25.8 ± 1.1	7.1 ± 2.3	0.51 ± 0.19	−0.29	−0.61

Note. E_l is the energy of the lower level of the transition, g_l and g_u are the statistical weights of the lower and upper levels respectively, A_{ul} is the Einstein A coefficient of the transition, v_{LSR} is the peak velocity of the line, FWHM is the full width at half maximum of the line, W is the equivalent width in units of hertz, and τ_p is the peak optical depth of the transition. η_0 is the opacity in the lower level of the transition calculated for $\epsilon = 0.5$. Line data were taken from the HITRAN database (Gordon et al. 2017).

(This table is available in machine-readable form.)

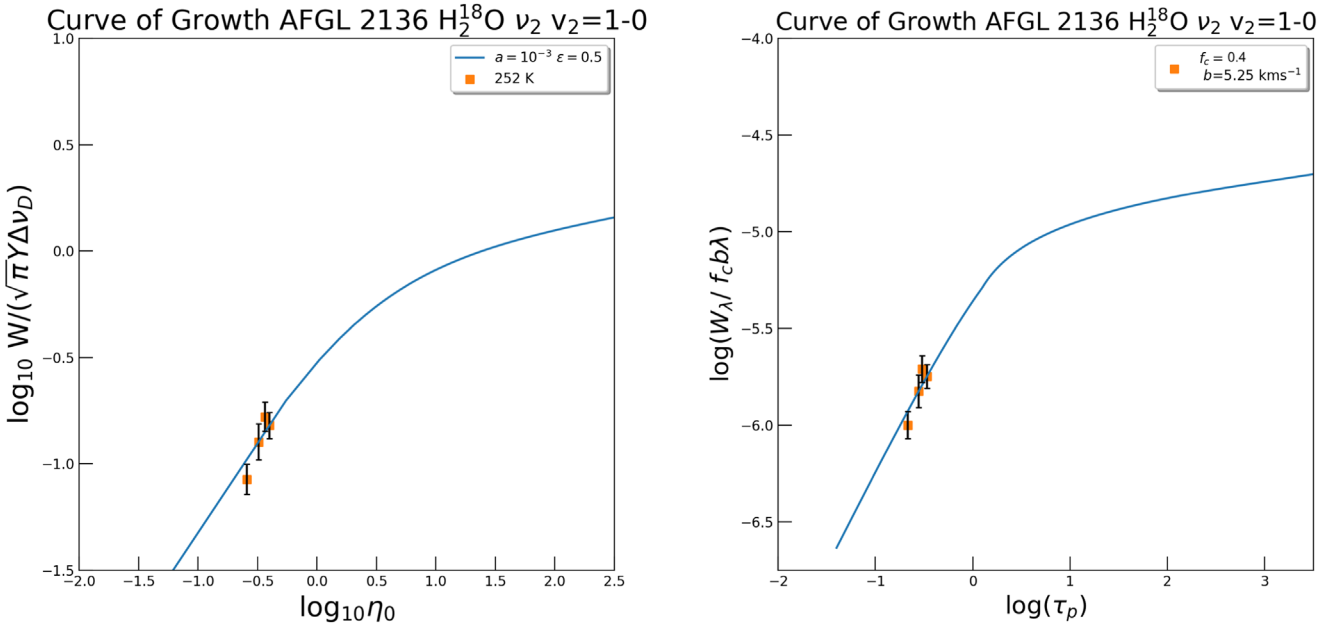

Figure 12. The curve of growth for $H_2{}^{18}O$ in AFGL 2136. The stellar atmosphere curve of growth assumes line formation by a combination of absorption and scattering.

Table 6
Line Parameters for the $v = 1$–0 of the $H_2^{18}O$ Transition of AFGL 2136

Transition	λ (μm)	E_l (K)	g_l	g_u	A_{ul} (s^{-1})	v_{LSR} (km s^{-1})	FWHM (km s^{-1})	W (10^8 Hz)	$\log_{10}(\eta_0)$	$\log_{10}(\tau_p)$
$2_{1,2}$–$1_{0,1}$	6.0743	34	9	15.0	7.0	26.2 ± 0.6	14.3 ± 1.8	1.44 ± 0.16	−0.43	−0.52
$4_{1,4}$–$3_{0,3}$	5.9604	196	21	27.0	8.6	25.2 ± 0.4	12.7 ± 1.5	1.35 ± 0.14	−0.39	−0.47
$5_{0,5}$–$4_{1,4}$	5.9200	322	27	33.0	9.5	27.6 ± 0.5	8.9 ± 1.4	1.14 ± 0.19	−0.49	−0.56
$2_{2,1}$–$1_{1,0}$	5.9095	60	9	15.0	5.9	26.3 ± 0.4	10.5 ± 1.4	0.76 ± 0.16	−0.58	−0.67

Note. E_l is the energy of the lower level of the transition, g_l and g_u are the statistical weights of the lower and upper levels respectively, A_{ul} is the Einstein A coefficient of the transition, v_{LSR} is the peak velocity of the line, FWHM is the full width at half maximum of the line, W is the equivalent width in units of Hz and τ_p is the peak optical depth of the transition. η_0 is the opacity in the lower level of the transition calculated for $\epsilon = 0.5$. Line data were taken from the HITRAN database (Gordon et al. 2017).

The chemical composition as derived from all mid-IR absorption line studies.

5.1. Foreground Absorbing Gas

We consider here foreground absorption against the mid-IR continuum from the extended (∼125 au radius; Monnier et al. 2009; de Wit et al. 2011; Frost et al. 2021) disk. It seems reasonable to relate these clumps to the region that is also responsible for the H_2O maser emission observed toward these sources, if we take into account that maser emission only occurs in directions with enough velocity coherence. Observationally, for AFGL 2136, the strongest maser emission occurs at 27.1 km s^{-1} (Menten & van der Tak 2004) very similar to one of the absorption components seen in the mid-IR. For AFGL 2591, the H_2O maser emission has been attributed to the outflow cavity walls where the outflow interacts with the ambient cloud material, and for this source too, the measured masers velocities (∼−31 to −10 km s^{-1}; Trinidad et al. 2003; Torrelles et al. 2014) encompass the H_2O absorption line velocities. The presence of nonzero saturated mid-IR absorption lines requires that the foreground gas only partially covers the source. Within this scenario, as the spatial distribution of the H_2O masers (600 × 1000 au; Menten & van der Tak 2004) in AFGL 2136 covers an extent that is larger than the size of the mid-IR continuum, the presence of multiple velocity components is most intuitively interpreted as several blobs of size ∼100 au along the line of sight (Knez et al. 2009; Barentine & Lacy 2012; Indriolo et al. 2015; Rangwala et al. 2018). For AFGL 2591, we have to conclude that the outflow cavity wall only partially covers the mid-IR emitting disk surface. The observed HCN and C_2H_2 column density variations between vibrational bands at 7 and 13 μm originating from the same lower level (Barr et al. 2020) would then point toward wavelength-dependent covering factors, possibly related to variation in the source size with wavelength. This has to be in such a way that the HCN/C_2H_2 gas covers the source more than H_2O (Barr et al. 2022). Likewise, the presence of emission rather than absorption lines at 3 μm implies resonant scattering of 3 μm continuum emission by (cool) foreground gas. This scattering material cannot be in front of the 3 μm source. However, this gas has to be quite close to the continuum source—in or near the disk—in order to explain the observed strength of the emission lines (Barr et al. 2020, Barr et al. 2022), and yet share the same velocity as the absorbing gas seen at other wavelengths. In short, the geometry of the system is quite constrained, where the absorbing gas

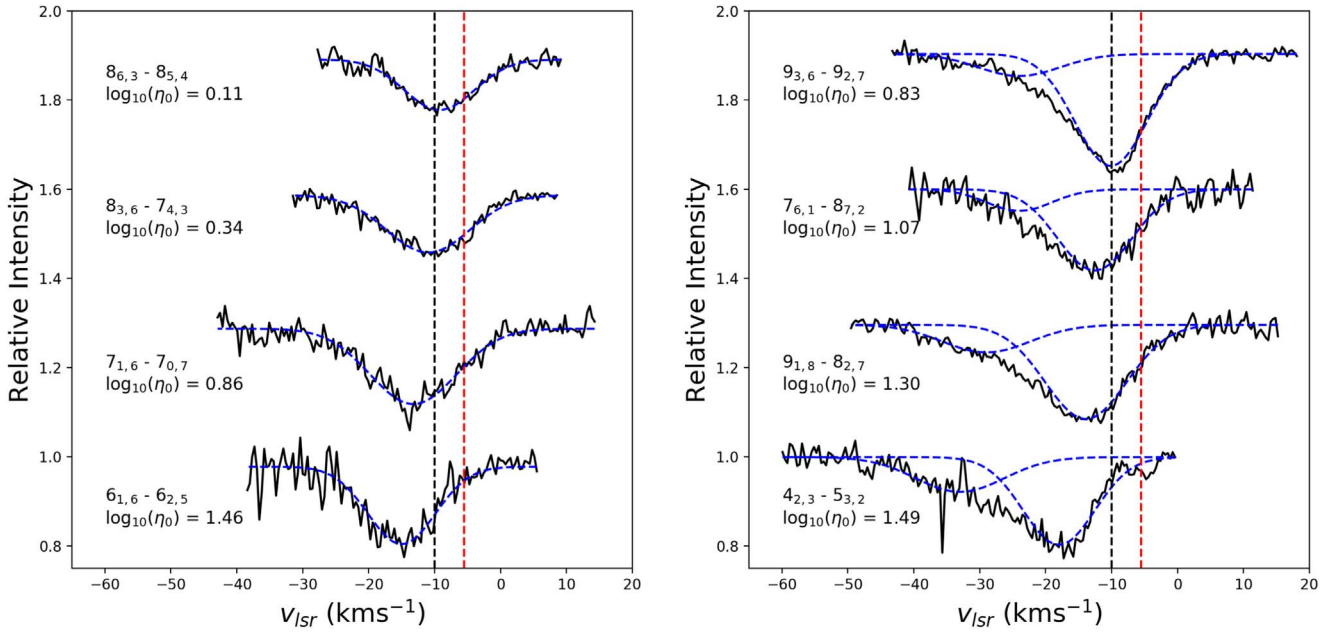

Figure 13. Line profiles of AFGL 2591 showing the trend in peak velocity with η_0. Transitions are shown that exhibit one and two velocity components in the *left* and *right* panels, respectively. The blue dashed lines denoted the Gaussian fits to each velocity component. The black dashed line at -10 km s^{-1} is added for reference and the red dashed line at -5.5 km s^{-1} indicates the velocity of the gaseous envelope as observed at submillimeter wavelengths.

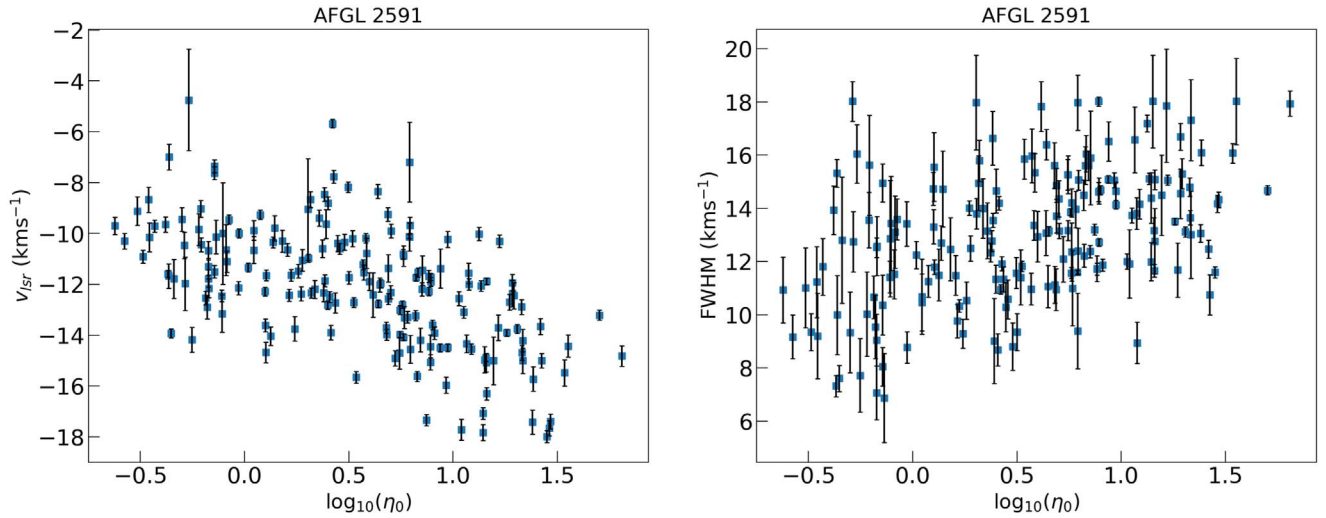

Figure 14. Plots illustrating the relationship between η_0 and the peak velocity and line width in AFGL 2591 on the *left* and *right*, respectively.

partially covers the background source at 13 μm, but not at all at 3 μm.

The derived physical conditions (Table 2) present somewhat of a challenge for the foreground absorption scenario. The observed high temperature implies shock heating as radiative heating would have to go through the dust and this dust would dominate the mid-IR emission of the region. Moreover, it would have to be at a distance of $\simeq$100 au from the illuminating source to be this hot (see the Appendix). Both J shocks and C shocks propagating into dense gas can produce large column densities ($>5 \times 10^{18}$ cm^{-2}) of warm H_2O. However, molecular gas in J shocks is calculated to be typically 300–400 K while C shocks heat gas to typically $\simeq$2000 K (Kaufman & Neufeld 1996; Hollenbach et al. 2013) compared to observed temperatures of $\simeq$500 K. Hence, in either case, the shock parameters have to be finely tuned to explain the observations. As an aside, we note that the high densities inferred ($>10^{10}$ cm^{-3}) from the similarity in the rotational and vibrational H_2O excitation temperatures would suppress H_2O maser emission (Kaufman & Neufeld 1996; Hollenbach et al. 2013). Submillimeter observations of AFGL 2591 have revealed emission of vibrationally excited HCN but this emission was associated with the disk rather than foreground material (Suri et al. 2021).

The observed chemical abundances in the absorbing gas pose also an issue for foreground shocked gas (Table 3). As observations of the plateau source in Orion demonstrate, shocks will also not produce the high abundances (Boonman et al. 2003; Burkhardt et al. 2016; Kristensen et al. 2017) observed in our study (Table 3). Likewise, the HCN/CO abundances in the different shock components associated with the outflow in L1448 (2×10^{-4}–2×10^{-3}; Tafalla et al. 2010) are an order of magnitude less than observed in the mid-IR absorption lines.

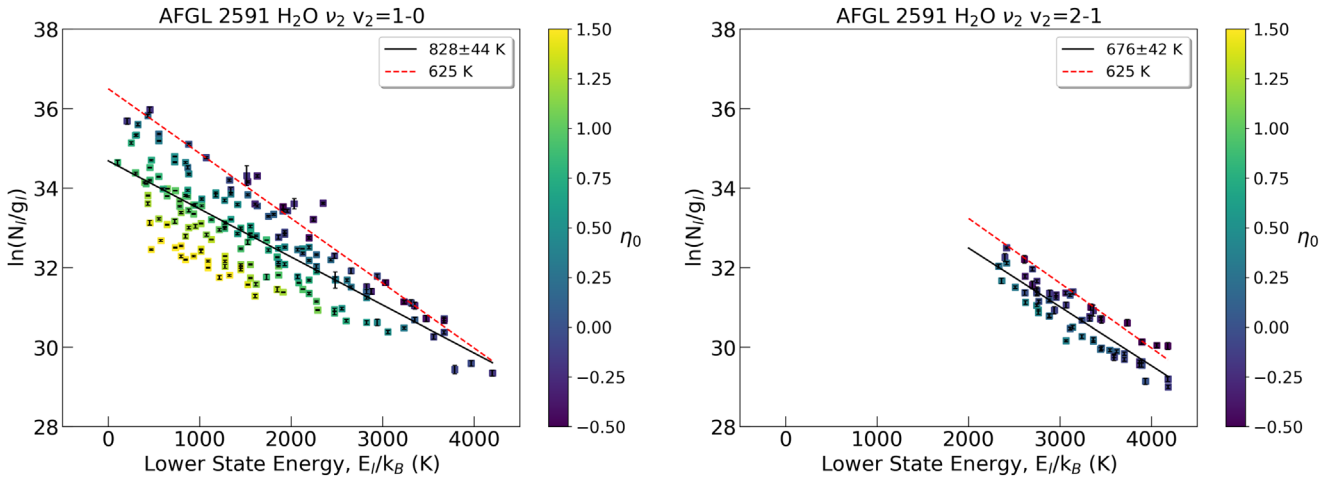

Figure 15. Rotation diagrams of the H_2O $v = 1$–0 (*left*) and vibrationally excited $v = 2$–1 (*right*) transitions of the ν_2 band in AFGL 2591. The color bar is a function of $\log_{10}(\eta_0)$. The dashed red line denotes the temperature of 625 K derived from the curve of growth. The solid black lines denote the fit to the rotation diagrams, and the temperature of this fit is given in the legend.

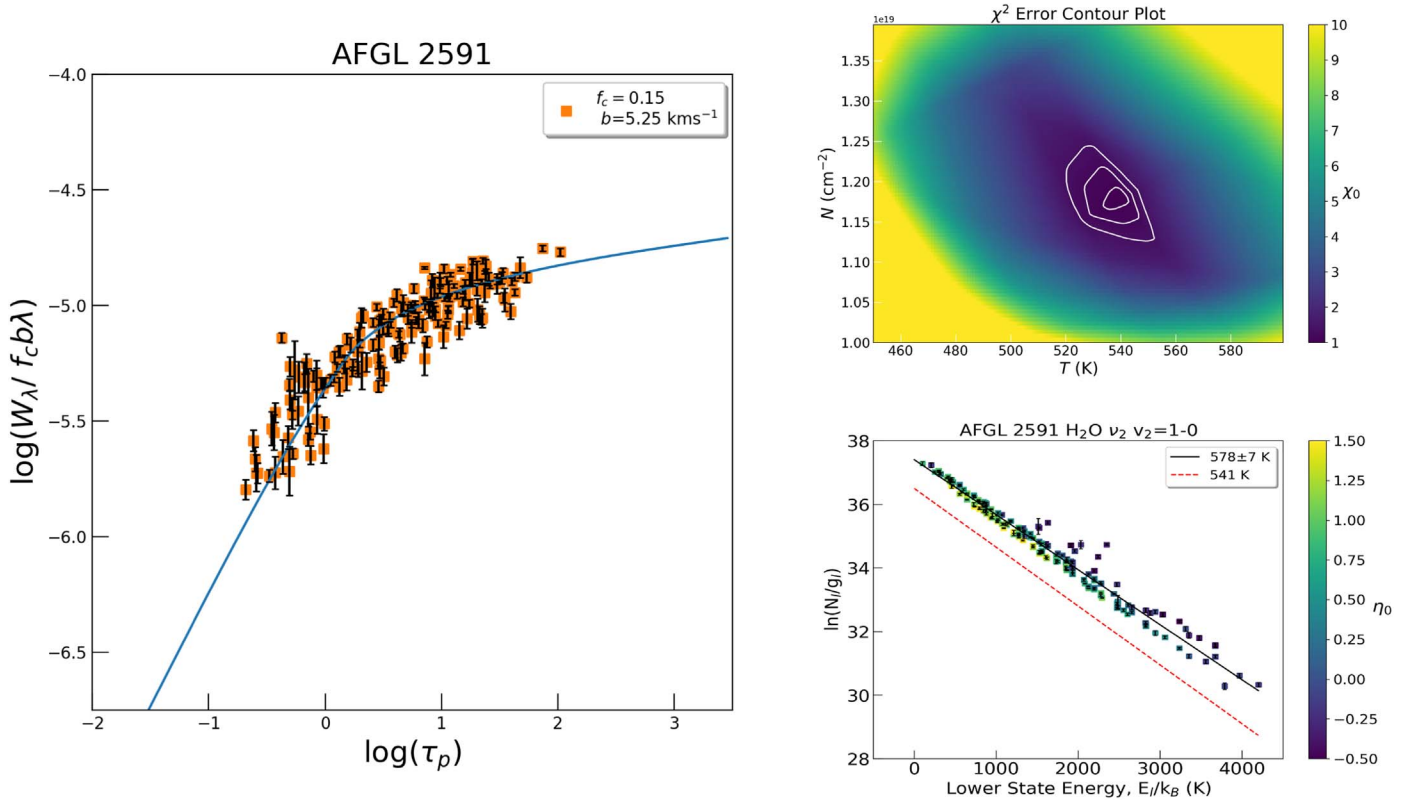

Figure 16. *Left*: the curve of growth for the $v = 1$–0 transition of AFGL 2591 for the slab model, taking a covering factor of 0.15 and $b = 5.25$ km s^{-1}. The best-fit empirical curve of growth is shown and the corresponding best-fit temperature and column density are indicated. All lines are included here calculated at the conditions derived from the lines with one velocity component. *Upper right*: the error on the parameters is given in the contour plot where the color scale is the reduced chi-square value. The contours represent the 1σ, 2σ, and 3σ uncertainty levels. *Lower right*: the best-fit temperature of 541 K from the curve of growth is represented by the red dashed line. The black solid lines are fits to the corrected data set and the corresponding temperatures are indicated for each case.

5.2. Disk Atmosphere Model

Similar to a stellar photosphere (Mihalas 1978), a disk atmosphere will show absorption lines in its mid-IR spectrum if the temperature decreases with height in the disk (Barr et al. 2020). If these lines are predominantly due to absorption rather than scattering, strong lines will all saturate at the same nonzero intensity level that is set by the temperature gradient in the disk (Mihalas 1978; Barr et al. 2020). The observed high density and high temperature are a natural consequence of locating the absorbing gas in the upper layers of the disk, commingled with the warm ($T_d \sim$600 K) dust causing the mid-IR continuum.

The observations severely constrain the geometry and structure of the absorbing region. ALMA observations of AFGL 2136 in a high energy, rotational transition in the vibrationally excited state of H_2O reveal a broad emission line profile associated with a Keplerian rotating disk (Maud et al. 2019). The mid-IR H_2O absorption profile shows two narrow peaks at 25 and 33 km s^{-1} that are slightly to the red of the

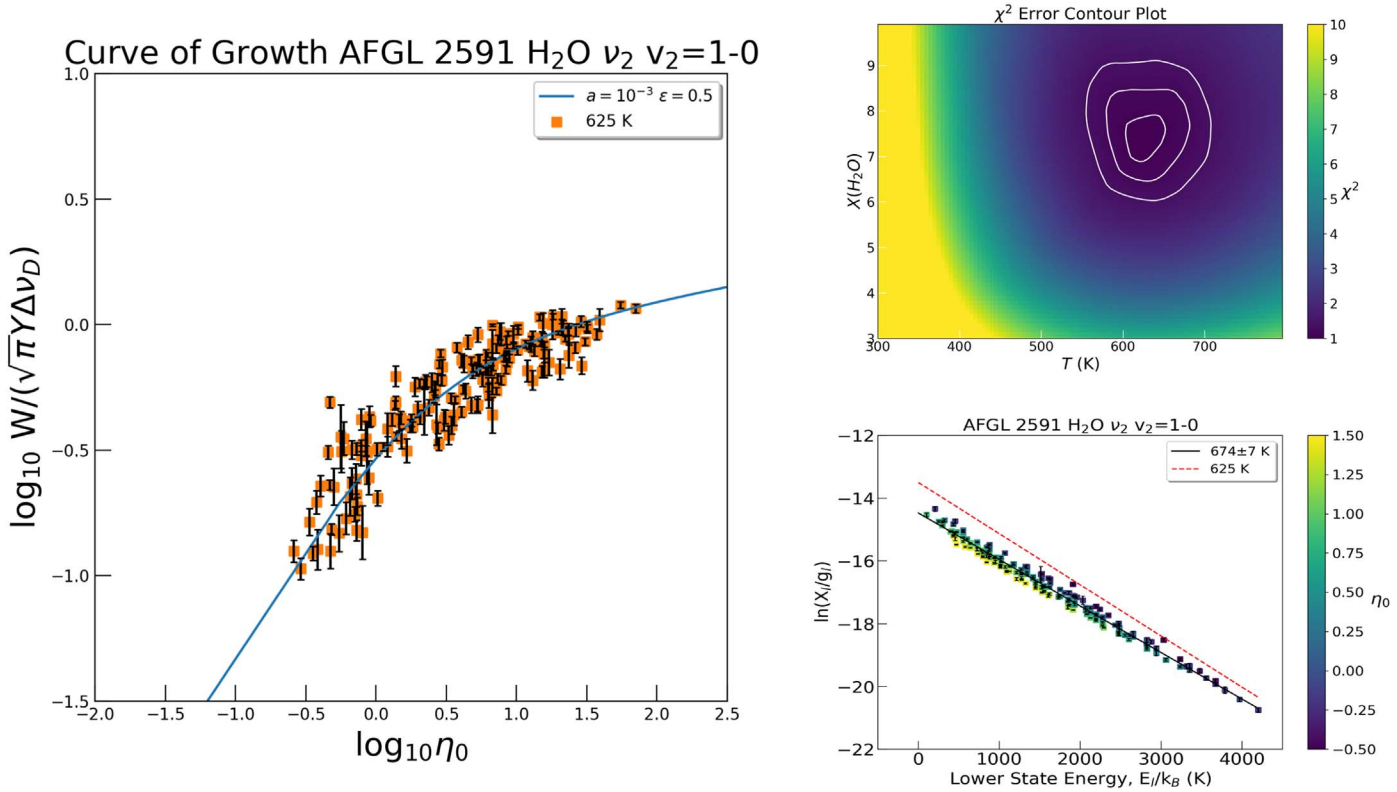

Figure 17. *Left*: the curve of growth for the $v = 1$–0 transition of AFGL 2591. The theoretical curve is for the case of $\epsilon = 0.5$. The empirical curve of growth is calculated based on the physical conditions given in Table 2. *Upper right*: the error on the parameters is given in the contour plot where the color scale is the reduced chi-square value. The contours represent the 1σ, 2σ, and 3σ uncertainty levels. The H_2O abundance is quoted relative to CO. *Lower right*: the rotation diagram is a function of η_0 and the abundances for the optically thick lines were determined using the curve of growth. The best-fit temperature of 625 K from the curve of growth is represented by the red dashed line. The black solid line is a fit to the corrected data set and the corresponding temperature is indicated. Note that the *y*-axis is the abundance in the lower level based on the stellar atmosphere theory.

centroid (23 km s^{-1}) of the submillimeter emission line (Indriolo et al. 2020). Hence, the mid-IR absorption has to arise in blobs of limited size in the disk. As their velocity is close to the systemic velocity and they are at ∼125 au (Frost et al. 2021) from a 45 $M_\odot$ star (Maud et al. 2019), the motion of these blobs is mainly transverse; e.g., either in the front or the back of the disk. On a 1000 au scale, AFGL 2591 also shows a complex dynamical environment with a Keplerian rotating disk containing multiple cores that could evolve into companions (Suri et al. 2021). In general, the complex morphology with spiral arms and subcondensations revealed by submillimeter observations of disks around massive protostars may reflect Toomre instability (Maud et al. 2019; Johnston et al. 2020; Suri et al. 2021). This large-scale structure likely persists into the inner disk, and in this scenario, mid-IR absorption lines would be attributed to bright (dust emission) spots therein. The presence of HCN and C_2H_2 emission—rather than absorption—lines in the *L*-band of AFGL 2591 implies that these molecules are absent in the region producing the 3 μm continuum. The low (∼200 K) excitation temperatures and narrow line width suggest that these emission lines are due to resonant scattering by lukewarm gas high up in the disk photosphere exposed to—but not in front of—the 3 μm continuum source (Barr et al. 2020). Within this context, we would interpret the observed blueshift of the H_2O lines in AFGL 2591 with increasing η_0 (Figures 13 and 14) as evidence for a disk wind at the top of the photosphere, as lines with higher opacity probe higher layers in the disk atmosphere.

Warm gas in (or in front of) an externally heated disk will show emission lines because, while the mid-IR optical depth is very high, the continuum emitting layer in the disk surface will be optically thin. The Appendix delineates this issue based upon a simplified model for such a system. We note that, for this reason, T Tauri stars and Herbig AeBe stars show mid-IR molecular emission lines (Blake & Boogert 2004; Salyk et al. 2011, 2019; Adams et al. 2019). Hence, our analysis is based upon an internally heated disk, resulting in a decreasing temperature gradient with height and this internal heating source poses a challenge for this scenario. Dissipation of gravitational energy requires an accretion rate given by $\dot{M} = 8\pi\sigma_{sb}T^4r^3/3GM_\star$. With $M_\star = 40$ $M_\odot$, $T = 600$ K, and $r = 125$ au, the required accretion rate ($\dot{M} = 1.2$ $M_\odot$ yr^{-1}) is orders of magnitude above the accretion rate expected for massive protostars ($\dot{M}$ $\sim 3 \times 10^{-3}$ $M_\odot$ yr^{-1}; McKee & Tan 2003; Hosokawa et al. 2010; Kuiper et al. 2011; Caratti o Garatti et al. 2017). Hence, an additional source of heating has to be invoked, such as heating by dissipation of turbulence or magnetic fields inherited from the parent molecular core, or local gravitational energy dissipation in the disk associated with fragmentation and subcondensation formation. Such structures are prevalent in these high mass systems (Ilee et al. 2018; Maud et al. 2019; Johnston et al. 2020; Suri et al. 2021) and the dominance of this dissipation may reflect the young age of hot cores ($\leqslant 10^5$ yr) inferred from gravitational collapse and hot core chemical clock considerations (Charnley et al. 1992; Wilner et al. 2001; Doty et al. 2002; McKee & Tan 2003; Furuya et al. 2005).

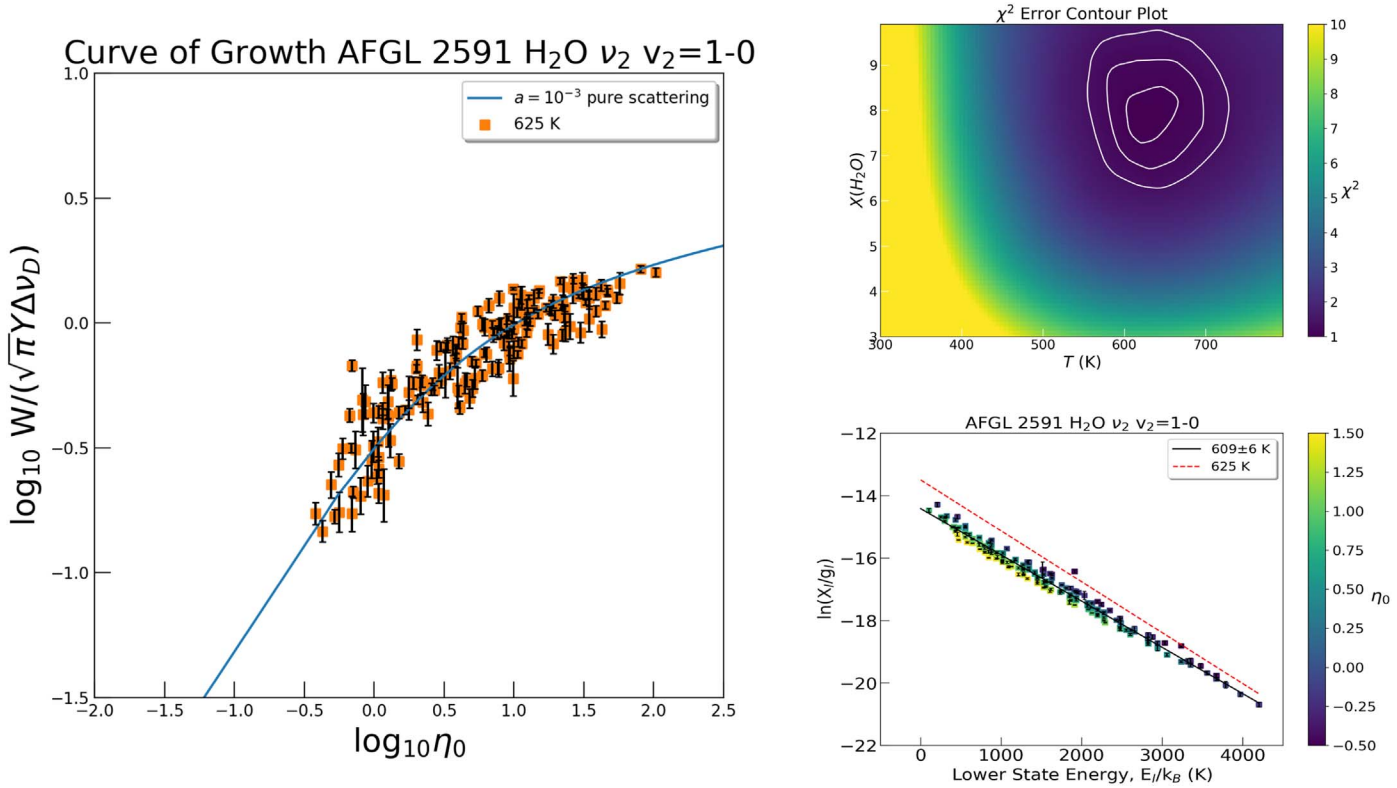

Figure 18. *Left*: the curve of growth for the $v = 1$–0 transition of AFGL 2591. The theoretical curve is for the case of $\epsilon = 0$. The empirical curve of growth is calculated based on the physical conditions given in Table 2. *Upper right*: the error on the parameters is given in the contour plot where the color scale is the reduced chi-square value. The contours represent the 1σ, 2σ, and 3σ uncertainty levels. The H_2O abundance is quoted relative to CO. *Lower right*: the rotation diagram is a function of η_0 and the abundances for the optically thick lines were determined using the curve of growth. The best-fit temperature of 625 K from the curve of growth is represented by the red dashed line. The black solid line is a fit to the corrected data set and the corresponding temperature is indicated. Note that the y-axis is the abundance in the lower level based on the stellar atmosphere theory.

As a corollary to this, external illumination of the disk by the central protostar cannot be important and we attribute this to the flashlight effect (Nakano 1989; Yorke & Bodenheimer 1999; Kuiper et al. 2010). In the flashlight effect, disk density stratification directs the stellar radiative energy in the vertical direction, and as a result, radiation pressure does not influence the gas flow in the disk plane allowing massive stars to keep accreting. Models show that this focusing of the radiative energy into a *vertical* cone happens in a region with a scale size of a few disk scale heights (typically some 5% of the radius; Kuiper et al. 2016; Tanaka et al. 2016, 2017). The ionizing radiation from the star creates then a hypercompact H II region confined to the flashlight region. AFGL 2136 has an associated, highly elongated, highly collimated (half cavity opening angle of 11.25°; Frost et al. 2021) hypercompact H II region with a diameter (in the disk) of ∼6 au (Menten & van der Tak 2004) deep inside the region from which the mid-IR emission originates (125 au radius; Frost et al. 2021). For AFGL 2591, the diameter of this hypercompact H II region is already somewhat larger (∼125 au; Trinidad et al. 2003). Eventually, the ionizing flux will break out from the confined hypercompact H II region and create an ultracompact H II region. At that point, the disk will start to be externally irradiated and will dissipate.

In terms of chemistry, the H_2O abundance is expected to be high in warm gas. The observations, indeed, reveal high H_2O/CO ratios (Table 3). The observed high HCN/CO and C_2H_2/CO ratios are also found for disks around Herbig AeBe stars and T Tauri stars (Table 3). Chemical models show that, provided there is a mechanism to break C out of CO and N out of N_2, high abundances of C_2H_2 and HCN are produced (Walsh et al. 2015; Agúndez et al. 2018) but, in the absence of UV photons from the central star, the mechanism releasing C and N from their main reservoirs is unknown for disks around massive protostars. The observed HCN and C_2H_2 column density variations derived from 7 and 13 μm vibrational bands that probe the same lower level have been attributed to strong radial abundance gradients in these molecules, resulting in a filling in of the absorption lines at a longer wavelength by (unabsorbed) continuum emission (Barr et al. 2020). Strong radial abundance gradients in the disk are also implied by the L-band HCN and C_2H_2 emission lines (see above). We note that the mid-IR observations imply much higher abundance ratios than those derived from submillimeter studies of the AFGL 2591 hot core (Table 3; Kaźmierczak-Barthel et al. 2014). The submillimeter observations refer to much larger (12–4000 au) scale sizes and those abundances are thought to reflect the effects of grain mantle evaporation in the envelope (Doty et al. 2002).

6. Conclusions

We have analyzed the spectral features of H_2O in the 5–8 μm SOFIA/EXES spectral survey of the massive protostars AFGL 2136 and AFGL 2591 at a resolving power of $R = 50{,}000$ (6 km s^{-1}). Our conclusions are as follows:

1. Hundreds of rotational transitions of H_2O are detected in the ground and first vibrational states, as well as several

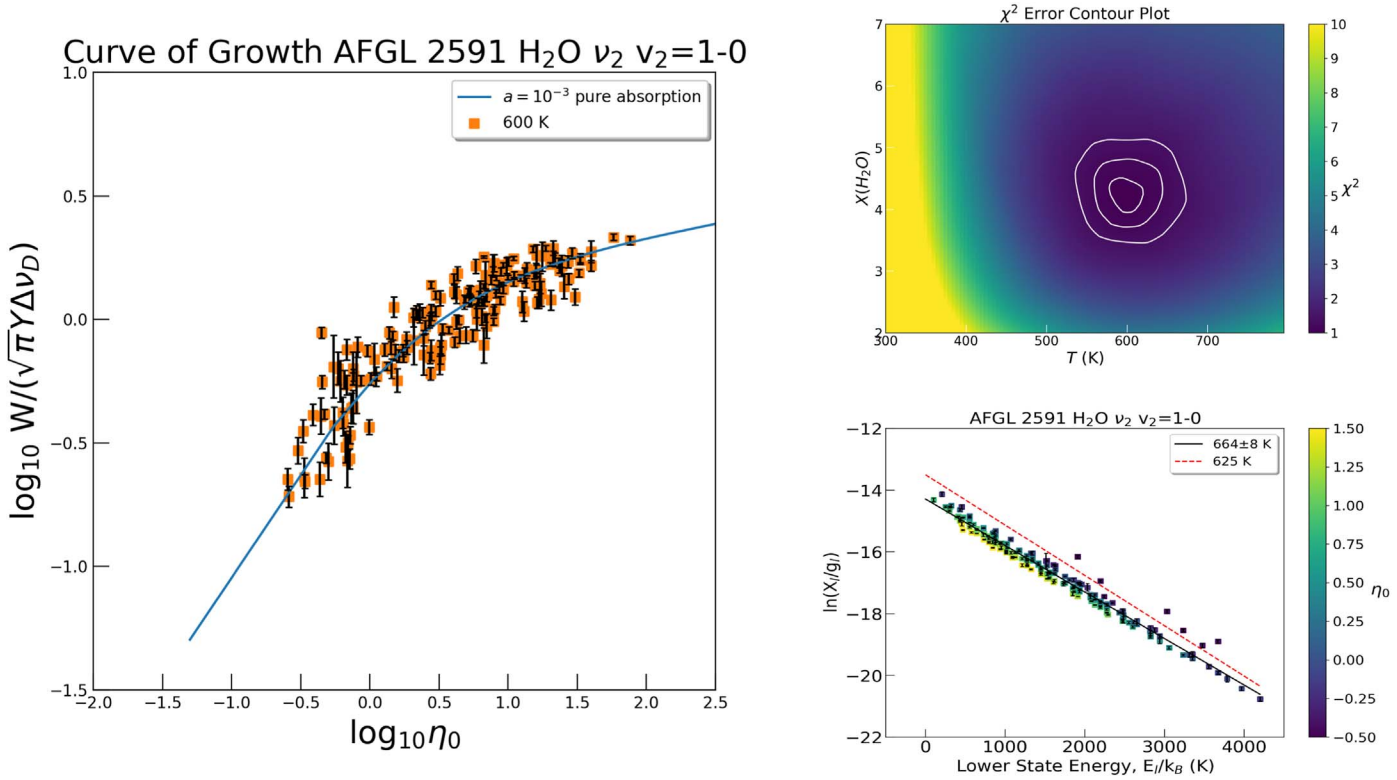

Figure 19. *Left*: the curve of growth for the $v = 1$–0 transition of AFGL 2591. The theoretical curve is for the case of $\epsilon = 1$. The empirical curve of growth is calculated based on the physical conditions given in Table 2. *Upper right*: the error on the parameters is given in the contour plot where the color scale is the reduced chi-square value. The contours represent the 1σ, 2σ, and 3σ uncertainty levels. The H_2O abundance is quoted relative to CO. *Lower right*: the rotation diagram is a function of η_0 and the abundances for the optically thick lines were determined using the curve of growth. The best-fit temperature of 625 K from the curve of growth is represented by the red dashed line. The black solid line is a fit to the corrected data set and the corresponding temperature is indicated. Note that the y-axis is the abundance in the lower level based on the stellar atmosphere theory.

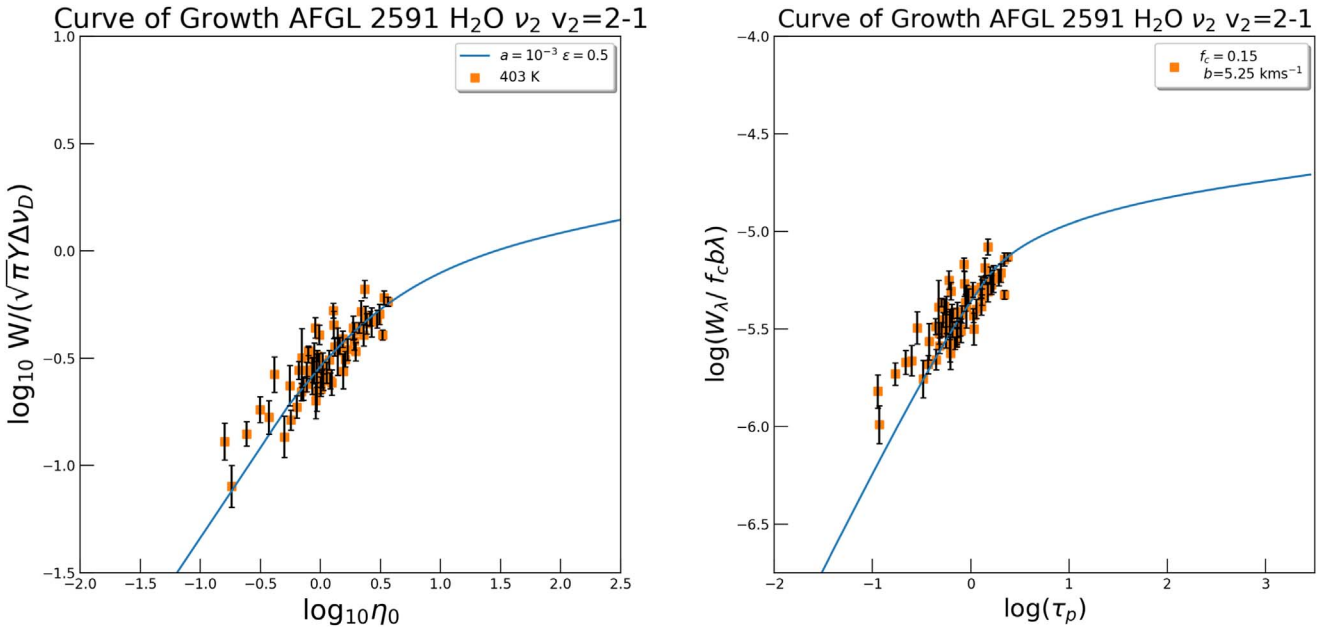

Figure 20. Curve of growth for AFGL 2591 $v_2 = 2$–1 band for the absorbing slab and stellar atmosphere models in the *right* and *left* panels, respectively. The best-fit temperature and abundance are shown for both cases.

lines of $H_2^{18}O$ lines. All transitions are observed in absorption.

2. Two main origins for the H_2O lines are investigated: foreground absorption against the mid-IR continuum source and an origin in the photosphere of an internally heated circumstellar disk. Using curve of growth analysis, H_2O temperatures of 457^{+13}_{-14} K and 470^{+24}_{-33} K are derived for the foreground and disk models respectively for

Table 7
Line Parameters for the $v = 1$–0 Transition of AFGL 2591

Transition	λ (μm)	E_l (K)	g_l	g_u	A_{ul} (s^{-1})	v_{LSR} (km s^{-1})	FWHM (km s^{-1})	W (10^8 Hz)	$\log_{10}(\eta_0)$	$\log_{10}(\tau_p)$
$12_{2,11}-11_{1,10}$	5.3719	2194	69	75	10.9	-9.7 ± 0.3	13.6 ± 0.9	3.69 ± 0.29	0.83	0.80
$12_{1,11}-11_{2,10}$	5.3737	2194	23	25	10.9	-8.7 ± 0.3	15.9 ± 1.0	3.95 ± 0.26	0.35	0.33
$11_{3,8}-10_{4,7}$	5.3772	2275	63	69	3.3	-10.3 ± 0.4	13.6 ± 1.2	2.08 ± 0.23	0.22	0.18
$9_{3,7}-8_{2,6}$	5.3806	1414	17	19	5.0	-8.8 ± 0.3	15.7 ± 0.8	4.04 ± 0.21	0.44	0.50
$8_{6,3}-8_{5,4}$	5.4172	1806	51	51	1.6	-9.3 ± 0.2	12.5 ± 0.6	2.79 ± 0.16	0.11	0.13
$4_{4,0}-3_{3,1}$	5.4218	410	7	9	5.4	-11.7 ± 0.1	13.4 ± 0.4	3.57 ± 0.11	0.86	1.03
$9_{6,3}-9_{5,4}$	5.4238	2125	57	57	1.9	-10.0 ± 0.2	10.4 ± 0.6	1.40 ± 0.10	0.01	−0.01
$11_{2,10}-10_{1,9}$	5.4248	1860	21	23	10.2	-8.2 ± 0.2	12.8 ± 0.6	3.38 ± 0.15	0.54	0.54
$11_{1,10}-10_{2,9}$	5.4285	1861	63	69	10.2	-10.2 ± 0.3	15.6 ± 0.4	6.31 ± 0.26	1.01	1.02
$7_{3,5}-6_{2,4}$	5.4431	867	13	15	3.9	-10.2 ± 0.2	14.5 ± 0.6	3.61 ± 0.14	0.62	0.74
$11_{6,5}-11_{5,6}$	5.4521	2876	69	69	2.4	-7.0 ± 0.5	11.4 ± 1.5	0.83 ± 0.13	−0.32	−0.43
$5_{3,2}-4_{2,3}$	5.4641	432	27	33	3.1	-12.1 ± 0.2	16.1 ± 0.2	5.51 ± 0.14	1.17	1.34
$12_{2,11}-12_{1,12}$	5.4689	2241	75	75	0.7	-9.7 ± 0.2	13.0 ± 1.1	1.54 ± 0.15	−0.39	−0.43
$10_{1,9}-9_{2,8}$	5.4862	1554	19	21	9.5	-12.0 ± 0.2	14.2 ± 0.2	4.26 ± 0.12	0.69	0.73
$10_{3,7}-9_{4,6}$	5.4904	1929	19	21	2.6	-12.2 ± 0.4	13.7 ± 1.1	1.24 ± 0.10	−0.13	−0.13
$12_{1,12}-11_{0,11}$	5.5022	1909	69	75	15.0	-11.9 ± 0.1	16.1 ± 0.4	5.42 ± 0.15	1.20	1.20
$11_{4,7}-10_{5,6}$	5.5031	2473	63	69	1.7	-10.4 ± 0.3	16.6 ± 1.9	1.49 ± 0.21	−0.17	−0.23
$9_{2,7}-8_{3,6}$	5.5179	1447	51	57	4.6	-12.2 ± 0.3	13.5 ± 0.2	3.83 ± 0.15	0.89	0.94
$5_{3,3}-4_{2,2}$	5.5229	454	9	11	3.9	-14.1 ± 0.1	15.2 ± 0.5	3.59 ± 0.13	0.80	0.96
$11_{2,10}-11_{1,11}$	5.5270	1909	23	23	0.8	-9.7 ± 0.3	12.2 ± 1.2	0.80 ± 0.08	−0.58	−0.58
$11_{1,10}-11_{0,11}$	5.5290	1909	69	69	0.8	-11.5 ± 0.2	15.9 ± 0.7	2.16 ± 0.12	−0.11	−0.10
$12_{4,9}-12_{3,10}$	5.5298	2824	75	75	2.2	-9.4 ± 0.5	10.8 ± 1.5	0.97 ± 0.16	−0.26	−0.36
$9_{2,8}-8_{1,7}$	5.5319	1270	17	19	8.8	-13.3 ± 0.2	15.0 ± 0.7	4.22 ± 0.19	0.82	0.89
$13_{3,10}-13_{2,11}$	5.5373	3233	81	81	2.1	-10.3 ± 0.3	10.7 ± 0.8	0.68 ± 0.07	−0.54	−0.68
$9_{1,8}-8_{2,7}$	5.5479	1274	51	57	8.7	-13.9 ± 0.1	14.6 ± 0.1	5.95 ± 0.10	1.30	1.37
$10_{5,6}-10_{4,7}$	5.5496	2275	63	63	2.7	-11.6 ± 0.2	13.0 ± 0.3	2.26 ± 0.09	0.14	0.11
$4_{3,1}-3_{2,2}$	5.5567	296	7	9	4.3	-15.6 ± 0.2	16.6 ± 0.7	3.86 ± 0.17	0.87	1.04
$9_{5,5}-9_{4,6}$	5.5599	1929	19	19	2.7	-12.5 ± 0.3	12.0 ± 0.8	1.12 ± 0.08	−0.15	−0.15
$11_{3,9}-11_{2,10}$	5.5613	2194	23	23	1.7	-10.9 ± 0.2	10.9 ± 0.7	0.79 ± 0.05	−0.45	−0.48
$7_{5,2}-7_{4,3}$	5.5775	1340	45	45	2.2	-12.7 ± 0.2	13.0 ± 0.2	3.17 ± 0.10	0.56	0.63
$10_{1,9}-10_{0,10}$	5.5909	1603	21	21	1.0	-13.9 ± 0.2	9.4 ± 0.5	0.97 ± 0.05	−0.32	−0.28
$8_{5,3}-8_{4,4}$	5.5917	1628	17	17	2.6	-12.1 ± 0.3	14.5 ± 0.8	2.00 ± 0.12	0.01	0.04
$9_{3,6}-8_{4,5}$	5.6118	1615	51	57	2.0	-12.8 ± 0.2	12.6 ± 0.5	2.45 ± 0.12	0.44	0.47
$8_{2,6}-7_{3,5}$	5.6208	1175	15	17	3.5	-7.8 ± 0.3	13.1 ± 0.3	3.75 ± 0.18	0.47	0.55
$7_{2,6}-6_{1,5}$	5.6318	781	13	15	6.9	-14.5 ± 0.2	16.1 ± 0.1	5.16 ± 0.11	0.98	1.10
$9_{2,8}-9_{1,9}$	5.6485	1324	19	19	1.2	-12.4 ± 0.2	12.7 ± 0.6	1.94 ± 0.09	−0.07	−0.01
$9_{4,6}-9_{3,7}$	5.6590	1750	19	19	3.0	-11.3 ± 0.2	13.4 ± 0.5	2.05 ± 0.08	0.05	0.08
$10_{2,8}-10_{1,9}$	5.6645	1860	21	21	2.1	-11.8 ± 0.3	10.6 ± 1.0	0.95 ± 0.09	−0.14	−0.13
$13_{4,9}-13_{3,10}$	5.6840	3475	81	81	3.7	-10.2 ± 0.6	10.7 ± 1.6	0.84 ± 0.15	−0.42	−0.58
$8_{4,5}-8_{3,6}$	5.6864	1447	51	51	3.1	-13.7 ± 0.2	16.5 ± 0.9	4.20 ± 0.26	0.72	0.77
$7_{4,4}-7_{3,5}$	5.7051	1175	15	15	3.1	-12.2 ± 0.4	15.0 ± 1.1	2.86 ± 0.21	0.38	0.46
$10_{5,6}-9_{6,3}$	5.7081	2347	57	63	1.0	-11.7 ± 0.5	16.3 ± 0.5	3.05 ± 0.16	−0.33	−0.37
$8_{1,8}-7_{0,7}$	5.7096	843	45	51	12.5	-13.2 ± 0.2	15.7 ± 0.2	7.26 ± 0.22	1.74	1.86
$11_{3,8}-11_{2,9}$	5.7131	2432	69	69	3.2	-10.3 ± 0.2	13.8 ± 0.7	2.66 ± 0.15	0.18	0.12
$6_{4,3}-6_{3,4}$	5.7162	933	39	39	2.9	-15.1 ± 0.3	15.6 ± 0.4	5.28 ± 0.21	0.93	1.04
$5_{2,4}-4_{1,3}$	5.7187	396	9	11	5.2	-16.0 ± 0.3	16.0 ± 0.3	4.74 ± 0.19	1.01	1.17
$5_{4,2}-5_{3,3}$	5.7217	725	11	11	2.4	-13.9 ± 0.3	15.2 ± 0.3	4.30 ± 0.17	0.45	0.58
$4_{4,1}-4_{3,2}$	5.7238	550	27	27	1.6	-14.0 ± 0.1	14.3 ± 0.4	4.21 ± 0.13	0.78	0.93
$4_{4,0}-4_{3,1}$	5.7281	552	9	9	1.6	-12.4 ± 0.3	15.0 ± 0.3	3.52 ± 0.15	0.31	0.46
$8_{3,6}-8_{2,7}$	5.7320	1274	51	51	2.7	-13.0 ± 0.2	16.2 ± 0.7	4.16 ± 0.22	0.78	0.86
$7_{2,5}-6_{3,4}$	5.7352	933	39	45	2.6	-13.9 ± 0.2	13.1 ± 0.2	4.39 ± 0.16	0.95	1.06
$5_{4,1}-5_{3,2}$	5.7371	732	33	33	2.5	-13.6 ± 0.2	15.7 ± 0.2	5.57 ± 0.11	0.94	1.07
$9_{2,7}-9_{1,8}$	5.7494	1552	57	57	2.6	-10.8 ± 0.6	16.3 ± 0.7	4.15 ± 0.33	0.62	0.67
$7_{2,6}-7_{1,7}$	5.7735	843	15	15	1.7	-12.3 ± 0.2	16.7 ± 0.8	3.61 ± 0.17	0.36	0.48
$7_{3,5}-7_{2,6}$	5.7792	1021	15	15	3.1	-10.6 ± 0.2	11.9 ± 0.7	2.63 ± 0.16	0.49	0.59
$9_{5,4}-8_{6,3}$	5.7822	2031	51	57	0.7	-10.5 ± 0.5	18.8 ± 0.8	2.14 ± 0.62	−0.25	−0.26
$7_{1,6}-7_{0,7}$	5.8022	843	45	45	1.8	-13.2 ± 0.2	15.5 ± 0.6	4.87 ± 0.22	0.86	0.98
$11_{4,7}-11_{3,8}$	5.8050	2609	69	69	5.3	-11.5 ± 0.3	11.9 ± 0.7	2.72 ± 0.20	0.30	0.22
$6_{3,4}-6_{2,5}$	5.8180	795	39	39	3.4	-11.6 ± 0.4	14.9 ± 0.6	5.21 ± 0.32	1.11	1.24
$6_{1,6}-5_{0,5}$	5.8227	468	33	39	10.8	-14.8 ± 0.4	18.8 ± 0.5	6.61 ± 0.27	1.85	2.01
$9_{4,5}-9_{3,6}$	5.8280	1846	57	57	5.2	-9.9 ± 0.3	14.3 ± 0.3	3.95 ± 0.15	0.74	0.75
$6_{2,5}-6_{1,6}$	5.8342	643	39	39	2.1	-14.5 ± 0.2	15.2 ± 0.2	5.86 ± 0.11	1.01	1.15
$8_{2,6}-8_{1,7}$	5.8380	1270	17	17	3.3	-8.5 ± 0.3	17.5 ± 1.0	3.19 ± 0.18	0.42	0.49

Table 7
(Continued)

Transition	λ (μm)	E_l (K)	g_l	g_u	A_{ul} (s^{-1})	v_{LSR} (km s^{-1})	FWHM (km s^{-1})	W (10^8 Hz)	$\log_{10}(\eta_0)$	$\log_{10}(\tau_p)$
$10_{3,8}-9_{4,5}$	5.8394	1957	57	63	0.7	-9.0 ± 0.3	14.6 ± 1.0	1.89 ± 0.16	−0.17	−0.17
$8_{4,4}-7_{5,3}$	5.8410	1524	15	17	0.9	-11.6 ± 0.1	9.2 ± 0.4	1.37 ± 0.06	−0.33	−0.28
$5_{3,3}-5_{2,4}$	5.8473	598	11	11	3.5	-14.0 ± 0.2	12.4 ± 0.7	2.85 ± 0.16	0.72	0.86
$9_{3,7}-8_{4,4}$	5.8491	1628	17	19	0.9	-9.6 ± 0.3	15.0 ± 0.9	1.83 ± 0.11	−0.34	−0.31
$6_{2,4}-5_{3,3}$	5.8575	725	11	13	1.8	-11.9 ± 0.2	14.6 ± 0.3	3.45 ± 0.14	0.42	0.56
$8_{4,5}-7_{5,2}$	5.8656	1525	45	51	0.9	-13.6 ± 0.3	14.4 ± 0.6	2.86 ± 0.16	0.14	0.18
$4_{3,2}-4_{2,3}$	5.8670	432	27	27	3.2	-15.1 ± 0.4	12.9 ± 0.2	4.41 ± 0.40	1.20	1.36
$9_{3,6}-9_{2,7}$	5.8729	1729	57	57	5.2	-10.1 ± 0.1	12.8 ± 0.1	5.83 ± 0.07	0.83	0.85
$3_{3,1}-3_{2,2}$	5.8784	296	7	7	2.4	-15.7 ± 0.2	16.8 ± 0.8	4.73 ± 0.21	0.57	0.75
$8_{3,6}-7_{4,3}$	5.8860	1340	45	51	1.0	-11.0 ± 0.2	14.9 ± 0.6	3.44 ± 0.16	0.34	0.41
$5_{2,4}-5_{1,5}$	5.8909	470	11	11	2.5	-12.8 ± 0.1	17.3 ± 0.6	4.27 ± 0.14	0.68	0.84
$4_{3,1}-4_{2,2}$	5.9167	454	9	9	3.9	-12.8 ± 0.1	14.9 ± 0.1	4.45 ± 0.10	0.79	0.95
$7_{2,5}-7_{1,6}$	5.9228	1013	45	45	4.4	-10.0 ± 0.3	18.1 ± 0.3	6.21 ± 0.18	1.16	1.26
$8_{3,5}-8_{2,6}$	5.9246	1414	17	17	6.1	-11.2 ± 0.2	12.3 ± 0.6	2.60 ± 0.13	0.61	0.66
$5_{3,2}-5_{2,3}$	5.9383	642	33	33	5.0	-13.7 ± 0.2	14.2 ± 0.2	5.04 ± 0.12	1.35	1.49
$7_{3,4}-7_{2,5}$	5.9507	1125	45	45	6.5	-10.3 ± 0.2	16.0 ± 0.2	6.12 ± 0.16	1.26	1.35
$6_{3,3}-6_{2,4}$	5.9530	867	13	13	6.0	-11.5 ± 0.2	17.0 ± 0.7	4.94 ± 0.20	0.87	0.99
$6_{3,3}-5_{4,2}$	5.9792	878	11	13	0.8	-9.5 ± 0.2	14.7 ± 0.8	2.36 ± 0.12	−0.04	0.08
$6_{2,4}-6_{1,5}$	5.9942	781	13	13	5.8	-12.3 ± 0.2	13.0 ± 0.5	3.77 ± 0.14	0.92	1.05
$6_{3,4}-5_{4,1}$	6.0191	878	33	39	0.7	-12.3 ± 0.4	13.9 ± 0.4	3.14 ± 0.18	0.42	0.53
$6_{4,3}-5_{5,0}$	6.0375	1067	33	39	0.3	-11.3 ± 0.3	13.7 ± 0.4	1.81 ± 0.10	−0.14	−0.04
$5_{2,3}-5_{1,4}$	6.0441	574	33	33	7.2	-15.5 ± 0.5	17.0 ± 0.4	5.02 ± 0.26	1.57	1.72
$5_{2,4}-4_{3,1}$	6.0964	552	9	11	0.7	-12.3 ± 0.2	15.7 ± 0.6	2.66 ± 0.10	0.14	0.29
$4_{1,4}-3_{2,1}$	6.2133	305	21	27	0.4	-12.7 ± 0.4	12.6 ± 0.5	3.61 ± 0.25	0.47	0.65
$3_{3,0}-4_{2,3}$	6.2218	432	27	21	0.3	-14.7 ± 0.4	16.5 ± 1.3	3.40 ± 0.32	0.14	0.30
$2_{2,0}-3_{1,3}$	6.2453	204	7	5	0.4	-14.2 ± 0.5	9.5 ± 1.4	0.93 ± 0.14	−0.21	−0.03
$3_{2,1}-4_{1,4}$	6.2716	323	27	21	0.3	-13.7 ± 0.5	10.8 ± 0.5	3.08 ± 0.27	0.28	0.45
$3_{3,1}-4_{2,2}$	6.2827	454	9	7	0.4	-12.0 ± 1.0	13.9 ± 1.1	1.69 ± 0.33	−0.25	−0.09
$2_{2,1}-3_{1,2}$	6.3737	249	21	15	1.1	-11.4 ± 0.5	15.8 ± 0.6	4.71 ± 0.31	0.73	0.91
$1_{1,1}-2_{0,2}$	6.3903	100	5	3	5.3	-13.3 ± 0.4	12.3 ± 1.4	2.76 ± 0.32	0.80	1.00
$4_{1,3}-4_{2,2}$	6.4115	454	9	9	11.5	-14.2 ± 0.4	14.1 ± 1.6	3.88 ± 0.45	1.37	1.53
$7_{2,5}-7_{3,4}$	6.4506	1212	45	45	12.5	-14.4 ± 0.4	18.8 ± 1.6	5.39 ± 0.55	1.59	1.67
$6_{2,4}-6_{3,3}$	6.4531	951	13	13	11.3	-15.0 ± 0.5	18.8 ± 1.7	5.16 ± 0.48	1.19	1.30
$12_{4,8}-12_{5,7}$	6.4820	3310	25	25	13.9	13.1 ± 0.7	14.0 ± 2.2	1.85 ± 0.29	−0.07	−0.22
$9_{2,7}-9_{3,6}$	6.5126	1846	57	57	12.2	-13.7 ± 0.5	18.7 ± 2.1	5.04 ± 0.68	1.25	1.27
$13_{5,8}-13_{6,7}$	6.5392	3966	81	81	12.5	-10.6 ± 1.0	12.8 ± 0.9	1.21 ± 0.19	−0.05	−0.27
$10_{4,6}-10_{5,5}$	6.5401	2482	21	21	11.1	-9.1 ± 8.0	18.8 ± 1.8	2.25 ± 0.50	0.34	0.29
$7_{4,4}-8_{3,5}$	6.5818	1511	17	15	0.9	-4.7 ± 3.9	17.0 ± 1.1	1.75 ± 0.27	−0.23	−0.18
$5_{3,3}-5_{4,2}$	6.5950	878	11	11	6.1	-14.4 ± 0.4	18.8 ± 0.2	3.73 ± 0.04	0.93	1.04
$6_{3,4}-6_{4,3}$	6.6007	1088	39	39	7.5	-15.7 ± 0.5	17.0 ± 0.5	4.46 ± 0.25	1.42	1.51
$10_{4,7}-10_{5,6}$	6.6409	2473	63	63	10.0	-10.9 ± 0.4	13.5 ± 1.1	2.68 ± 0.27	0.80	0.74
$9_{3,7}-9_{4,6}$	6.6642	1929	19	19	9.4	-11.9 ± 0.3	14.1 ± 0.9	2.61 ± 0.18	0.64	0.64
$10_{3,8}-10_{4,7}$	6.7052	2275	63	63	9.6	-11.9 ± 0.2	15.6 ± 0.5	3.47 ± 0.13	0.93	0.90
$6_{1,6}-6_{2,5}$	6.7121	795	39	39	4.9	-15.0 ± 0.3	12.1 ± 0.8	3.39 ± 0.26	1.46	1.59
$6_{3,4}-7_{2,5}$	6.7146	1125	45	39	2.0	-14.6 ± 0.5	16.0 ± 0.4	3.45 ± 0.17	0.83	0.92
$8_{2,7}-8_{3,6}$	6.7157	1447	51	51	7.7	-11.9 ± 0.3	15.6 ± 0.9	4.92 ± 0.35	1.32	1.38
$8_{2,7}-8_{3,6}$	6.7157	1447	51	51	7.7	-12.4 ± 0.5	17.6 ± 0.5	5.19 ± 0.35	1.32	1.38
$11_{3,9}-11_{4,8}$	6.7557	2652	23	23	9.6	-10.6 ± 0.3	12.7 ± 0.7	1.89 ± 0.11	0.24	0.17
$14_{4,11}-14_{5,10}$	6.7668	4199	87	87	11.3	-9.8 ± 0.6	11.4 ± 1.6	0.98 ± 0.17	−0.18	−0.43
$7_{0,7}-7_{1,6}$	6.7731	1013	45	45	4.7	-14.7 ± 0.3	14.7 ± 0.3	4.53 ± 0.15	1.37	1.47
$9_{2,8}-9_{3,7}$	6.7826	1750	19	19	7.5	-12.0 ± 0.3	12.4 ± 0.8	3.06 ± 0.20	0.69	0.71
$7_{1,7}-7_{2,6}$	6.7959	1021	15	15	4.6	-14.2 ± 0.5	16.5 ± 0.6	4.48 ± 0.35	0.88	0.98
$12_{3,10}-12_{4,9}$	6.8144	3058	75	75	9.6	-10.4 ± 0.3	11.7 ± 0.9	2.01 ± 0.19	0.48	0.36
$10_{1,9}-10_{2,8}$	6.8251	2069	21	21	7.6	-10.3 ± 0.3	10.4 ± 0.9	1.77 ± 0.15	0.52	0.50
$6_{2,5}-7_{1,6}$	6.8631	1013	45	39	5.3	-15.0 ± 0.5	18.2 ± 1.5	4.38 ± 0.44	1.37	1.47
$6_{0,6}-7_{1,7}$	6.8714	843	15	13	8.1	-16.3 ± 0.2	13.9 ± 1.2	3.20 ± 0.28	1.20	1.32
$8_{0,8}-8_{1,7}$	6.8749	1270	17	17	4.4	-14.9 ± 0.3	13.3 ± 0.9	2.88 ± 0.18	0.76	0.83
$8_{1,8}-8_{2,7}$	6.8867	1274	51	51	4.4	-15.0 ± 0.9	15.5 ± 1.5	3.30 ± 0.39	1.23	1.31
$5_{1,4}-6_{2,5}$	6.9063	795	39	33	5.8	-17.6 ± 0.3	15.2 ± 0.3	4.61 ± 0.19	1.50	1.62
$7_{1,7}-8_{0,8}$	6.9588	1070	17	15	7.8	-14.3 ± 0.3	17.5 ± 1.2	3.86 ± 0.27	1.10	1.20
$7_{2,6}-8_{1,7}$	6.9655	1270	17	15	5.7	-7.2 ± 1.6	18.8 ± 1.0	3.83 ± 0.49	0.83	0.90
$9_{0,9}-9_{1,8}$	6.9774	1552	57	57	4.2	-13.1 ± 0.2	14.8 ± 0.3	3.78 ± 0.11	1.09	1.13
$9_{1,9}-9_{2,8}$	6.9833	1554	19	19	4.2	-11.5 ± 0.3	16.9 ± 1.0	3.32 ± 0.20	0.61	0.65

Table 7
(Continued)

Transition	λ (μm)	E_l (K)	g_l	g_u	A_{ul} (s^{-1})	v_{LSR} (km s^{-1})	FWHM (km s^{-1})	W (10^8 Hz)	$\log_{10}(\eta_0)$	$\log_{10}(\tau_p)$
$3_{2,2}-4_{3,1}$	6.9933	552	9	7	8.6	-17.1 ± 0.2	13.2 ± 0.7	2.99 ± 0.16	1.18	1.33
$8_{3,6}-9_{2,7}$	7.0015	1729	57	51	3.4	-10.1 ± 0.5	10.9 ± 1.4	2.04 ± 0.33	0.83	0.85
$12_{1,11}-12_{2,10}$	7.0134	2820	25	25	7.1	-9.9 ± 0.4	11.8 ± 1.1	1.46 ± 0.13	0.08	−0.01
$7_{1,6}-8_{2,7}$	7.0218	1274	51	45	5.9	-12.4 ± 0.5	16.3 ± 0.6	4.54 ± 0.29	1.33	1.40
$12_{2,11}-12_{3,10}$	7.0231	2824	75	75	7.1	-10.2 ± 0.3	12.7 ± 1.0	2.00 ± 0.20	0.56	0.46
$4_{2,2}-5_{3,3}$	7.0475	725	11	9	6.8	-17.7 ± 0.4	13.1 ± 1.3	2.90 ± 0.28	1.08	1.21
$8_{1,8}-9_{0,9}$	7.0547	1324	57	51	7.4	-13.7 ± 0.3	13.6 ± 0.3	4.51 ± 0.23	1.46	1.52
$8_{2,7}-9_{1,8}$	7.0617	1552	57	51	5.8	-14.9 ± 0.2	14.3 ± 0.5	3.40 ± 0.14	1.19	1.24
$10_{0,10}-10_{1,9}$	7.0818	1860	21	21	4.1	-12.5 ± 0.2	10.3 ± 0.6	1.50 ± 0.09	0.45	0.46
$10_{1,10}-10_{2,9}$	7.0846	1861	63	63	4.1	-11.7 ± 0.2	12.9 ± 0.2	3.19 ± 0.12	0.92	0.93
$8_{1,7}-9_{2,8}$	7.0924	1554	19	17	5.9	-12.6 ± 0.2	14.8 ± 0.6	3.29 ± 0.14	0.73	0.77
$13_{1,12}-13_{2,11}$	7.1065	3233	81	81	7.0	-11.1 ± 0.4	13.7 ± 0.5	1.92 ± 0.12	0.32	0.18
$5_{2,3}-6_{3,4}$	7.1175	933	39	33	5.5	-17.4 ± 0.5	14.2 ± 0.3	3.63 ± 0.18	1.42	1.53
$9_{3,7}-10_{2,8}$	7.1252	2069	21	19	4.0	-12.4 ± 0.2	11.2 ± 0.6	1.83 ± 0.10	0.25	0.24
$4_{2,3}-5_{3,2}$	7.1469	732	33	27	5.6	-18.0 ± 0.2	12.8 ± 0.2	3.77 ± 0.13	1.49	1.62
$9_{0,9}-10_{1,10}$	7.1544	1603	63	57	7.1	-12.7 ± 0.3	12.9 ± 1.0	2.99 ± 0.28	1.31	1.35
$4_{3,1}-5_{4,2}$	7.1643	878	11	9	10.4	-17.8 ± 0.3	15.4 ± 0.9	3.91 ± 0.24	1.18	1.30
$11_{0,11}-11_{1,10}$	7.1889	2194	69	69	4.0	-12.3 ± 0.3	15.4 ± 0.7	3.13 ± 0.17	0.74	0.71
$11_{1,11}-11_{2,10}$	7.1903	2194	23	23	4.0	-11.6 ± 0.2	11.7 ± 0.2	1.74 ± 0.08	0.26	0.24
$14_{1,13}-14_{2,12}$	7.2001	3670	29	29	6.9	-8.7 ± 0.5	12.5 ± 1.3	0.85 ± 0.09	−0.42	−0.61
$7_{2,5}-8_{3,6}$	7.2125	1447	51	45	4.5	-14.5 ± 0.2	15.2 ± 0.6	3.36 ± 0.15	1.13	1.18
$11_{4,8}-12_{3,9}$	7.2383	3030	25	23	2.7	-9.1 ± 0.6	12.3 ± 1.5	0.70 ± 0.09	−0.48	−0.59
$7_{1,6}-7_{4,3}$	7.2543	1340	45	45	0.2	-12.9 ± 0.5	11.0 ± 1.2	1.04 ± 0.14	−0.14	−0.08
$4_{1,4}-5_{2,3}$	7.2723	642	33	27	1.2	-17.3 ± 0.2	14.3 ± 0.2	3.16 ± 0.09	0.91	1.05
$5_{3,2}-6_{4,3}$	7.2792	1088	39	33	8.0	-17.4 ± 0.3	15.3 ± 0.3	4.12 ± 0.14	1.51	1.60
$9_{2,7}-10_{3,8}$	7.2872	2081	63	57	4.5	-10.8 ± 0.2	12.8 ± 0.2	2.75 ± 0.10	0.80	0.78
$12_{1,12}-12_{2,11}$	7.3002	2554	75	75	3.9	-11.7 ± 0.2	10.8 ± 0.7	1.70 ± 0.13	0.54	0.47
$5_{2,4}-6_{3,3}$	7.3389	951	13	11	3.6	-14.7 ± 0.6	16.2 ± 0.6	3.06 ± 0.25	0.78	0.89
$11_{2,9}-12_{3,10}$	7.3945	2824	75	69	4.6	-9.4 ± 0.3	14.3 ± 1.0	2.44 ± 0.22	0.40	0.30
$12_{2,11}-13_{1,12}$	7.4401	2939	81	75	5.4	-9.6 ± 0.6	10.6 ± 1.6	1.70 ± 0.32	0.43	0.32
$12_{1,11}-13_{2,12}$	7.4423	2939	27	25	5.4	-11.1 ± 0.4	14.2 ± 1.4	1.82 ± 0.17	−0.05	−0.15
$7_{3,4}-8_{4,5}$	7.4618	1615	51	45	5.2	-12.0 ± 0.2	10.5 ± 0.8	2.53 ± 0.22	1.11	1.15
$6_{4,2}-7_{5,3}$	7.4654	1524	15	13	9.2	-11.5 ± 0.6	16.8 ± 1.8	3.78 ± 0.40	0.89	0.94
$6_{4,3}-7_{5,2}$	7.4708	1525	45	39	9.2	-12.9 ± 0.3	15.8 ± 0.3	3.84 ± 0.15	1.37	1.41
$12_{1,12}-13_{0,13}$	7.4744	2599	81	75	6.1	-9.3 ± 0.3	12.3 ± 0.8	2.01 ± 0.16	0.72	0.65
$8_{3,5}-9_{4,6}$	7.5193	1929	19	17	4.4	-10.6 ± 0.3	13.5 ± 0.3	2.14 ± 0.13	0.41	0.41
$14_{1,14}-14_{2,13}$	7.5326	3350	87	87	3.9	-10.7 ± 0.5	12.0 ± 1.4	1.57 ± 0.23	0.08	−0.07
$13_{2,12}-14_{1,13}$	7.5396	3350	29	27	5.1	-11.8 ± 0.8	13.9 ± 2.4	0.94 ± 0.16	−0.30	−0.45
$13_{2,11}-14_{3,12}$	7.5437	3671	87	81	4.5	-7.4 ± 0.3	9.7 ± 0.7	1.24 ± 0.11	−0.11	−0.29
$13_{2,11}-14_{3,12}$	7.5437	3671	87	81	4.5	-7.6 ± 0.3	11.7 ± 1.1	1.72 ± 0.16	−0.11	−0.29
$9_{3,6}-10_{4,7}$	7.5567	2275	63	57	3.9	-12.4 ± 0.9	18.7 ± 0.9	3.47 ± 0.22	0.65	0.62
$5_{1,5}-6_{2,4}$	7.5754	867	13	11	0.7	-14.0 ± 0.4	12.7 ± 1.0	1.63 ± 0.12	0.16	0.28
$10_{3,7}-11_{4,8}$	7.5802	2652	23	21	3.7	-10.0 ± 4.9	14.5 ± 1.8	1.26 ± 0.36	−0.07	−0.14
$6_{2,5}-7_{3,4}$	7.5819	1212	45	39	2.2	-11.4 ± 0.8	17.4 ± 0.7	3.78 ± 0.28	0.98	1.06
$7_{6,1}-8_{7,2}$	7.6060	2289	51	45	12.8	-12.6 ± 0.3	13.2 ± 0.3	3.37 ± 0.12	1.07	1.03
$14_{2,13}-15_{1,14}$	7.6420	3786	93	87	4.9	-10.1 ± 0.7	8.8 ± 1.7	0.60 ± 0.15	−0.10	−0.30
$8_{4,4}-9_{5,5}$	7.7118	2122	19	17	6.2	-5.7 ± 0.2	12.3 ± 0.2	2.97 ± 0.10	0.46	0.44
$8_{4,5}-9_{5,4}$	7.7676	2125	57	51	6.0	-11.7 ± 0.1	13.9 ± 0.1	3.16 ± 0.06	0.93	0.91
$9_{8,2}-10_{9,1}$	7.8054	3556	21	19	13.4	-10.7 ± 0.4	9.0 ± 1.0	0.84 ± 0.10	−0.14	−0.31
$9_{4,5}-10_{5,6}$	7.8122	2473	63	57	5.1	-8.3 ± 0.3	14.2 ± 0.8	1.88 ± 0.14	0.68	0.62
$9_{4,6}-10_{5,5}$	7.9452	2482	21	19	4.7	-9.8 ± 0.5	15.7 ± 1.4	1.31 ± 0.12	0.18	0.12

Note. E_l is the energy of the lower level of the transition, g_l and g_u are the statistical weights of the lower and upper levels respectively, A_{ul} is the Einstein A coefficient of the transition, v_{LSR} is the peak velocity of the line, FWHM is the full width at half maximum of the line, W is the equivalent width in units of Hz and τ_p is the peak optical depth of the transition. η_0 is the opacity in the lower level of the transition calculated for $\epsilon = 0.5$. Line data were taken from the HITRAN database (Gordon et al. 2017).

(This table is available in machine-readable form.)

AFGL 2136, and 541^{+1}_{-8} K and 625^{+27}_{-22} K, respectively, for AFGL 2591.

3. We find that some lines are optically thick, even though they saturate at 40% and 15% of the continuum for AFGL 2136 and AFGL 2591, respectively, resulting in a large scatter in the rotation diagram.
4. We find that, for a foreground origin for the absorption lines, the range of velocities observed overlaps with the

Table 8
Line Parameters for the $v = 2$–1 Transition of AFGL 2591

Transition	λ (μm)	E_l (K)	g_l	g_u	A_{ul} (s^{-1})	v_{LSR} (km s^{-1})	FWHM (km s^{-1})	W (10^8 Hz)	$\log_{10}(\eta_0)$	$\log_{10}(\tau_p)$
$10_{3,8}-9_{2,7}$	5.4015	4055	57	63.0	10.1	-8.6 ± 0.3	8.5 ± 0.9	0.81 ± 0.11	-0.62	-0.77
$4_{4,1}-3_{3,0}$	5.4373	2745	21	27.0	9.8	-9.5 ± 0.3	11.4 ± 0.8	1.36 ± 0.12	0.01	-0.18
$5_{3,2}-4_{2,3}$	5.5105	2745	27	33.0	6.2	-10.6 ± 0.3	10.6 ± 0.7	1.35 ± 0.11	-0.11	-0.30
$6_{3,4}-5_{2,3}$	5.5218	2955	33	39.0	6.9	-11.1 ± 0.3	8.2 ± 0.8	1.29 ± 0.16	-0.14	-0.32
$11_{0,11}-10_{1,10}$	5.6670	3892	63	69.0	27.6	-11.1 ± 0.3	10.1 ± 0.9	1.62 ± 0.18	0.02	-0.14
$10_{1,10}-9_{0,9}$	5.7202	3615	57	63.0	26.5	-11.9 ± 0.3	13.3 ± 0.9	2.08 ± 0.19	0.18	0.02
$8_{1,7}-7_{2,6}$	5.7330	3336	15	17.0	14.1	-10.1 ± 0.6	11.6 ± 1.7	0.90 ± 0.16	-0.43	-0.60
$6_{2,5}-5_{1,4}$	5.7627	2879	33	39.0	10.9	-10.0 ± 0.3	11.5 ± 0.8	1.92 ± 0.16	0.16	-0.02
$9_{1,9}-8_{0,8}$	5.7754	3363	17	19.0	25.2	-9.5 ± 0.4	14.1 ± 2.7	1.67 ± 0.53	-0.16	-0.32
$9_{0,9}-8_{1,8}$	5.7769	3364	51	57.0	25.2	-11.0 ± 0.3	14.1 ± 0.2	2.32 ± 0.13	0.32	0.15
$5_{2,4}-4_{1,3}$	5.8037	2698	9	11.0	9.7	-7.5 ± 0.5	9.8 ± 1.8	0.71 ± 0.16	-0.30	-0.49
$7_{1,6}-6_{2,5}$	5.8206	3110	39	45.0	11.8	-7.5 ± 0.2	12.2 ± 0.8	2.75 ± 0.22	0.11	-0.07
$8_{0,8}-7_{1,7}$	5.8353	3138	15	17.0	23.9	-7.0 ± 0.5	13.2 ± 1.2	2.28 ± 0.25	-0.04	-0.22
$3_{3,1}-3_{2,2}$	5.9287	2610	7	7.0	4.3	-11.6 ± 0.4	8.1 ± 1.5	0.41 ± 0.09	-0.74	-0.93
$3_{3,0}-3_{2,1}$	5.9478	2618	21	21.0	4.5	-9.2 ± 0.3	9.6 ± 0.8	0.83 ± 0.09	-0.24	-0.44
$6_{1,6}-5_{0,5}$	5.9485	2764	33	39.0	20.7	-9.7 ± 0.2	13.6 ± 0.5	2.94 ± 0.14	0.56	0.38
$6_{0,6}-5_{1,5}$	5.9622	2767	11	13.0	20.6	-10.1 ± 0.3	10.1 ± 0.7	1.25 ± 0.11	0.08	-0.10
$5_{3,2}-5_{2,3}$	5.9925	2955	33	33.0	8.7	-7.3 ± 0.3	11.3 ± 0.9	1.51 ± 0.15	-0.01	-0.19
$5_{1,5}-4_{0,4}$	6.0059	2615	9	11.0	18.8	-8.5 ± 0.4	11.1 ± 1.2	1.22 ± 0.17	0.09	-0.10
$7_{3,4}-7_{2,5}$	6.0232	3443	45	45.0	11.8	-10.6 ± 0.3	12.3 ± 0.8	1.63 ± 0.13	-0.10	-0.27
$7_{2,5}-7_{1,6}$	6.0322	3323	45	45.0	9.4	-10.8 ± 0.3	14.1 ± 1.0	1.38 ± 0.12	-0.11	-0.28
$2_{2,1}-2_{1,2}$	6.1010	2413	15	15.0	5.9	-9.7 ± 0.2	13.8 ± 0.6	1.68 ± 0.09	-0.10	-0.30
$3_{0,3}-2_{1,2}$	6.2028	2413	15	21.0	11.9	-9.8 ± 0.4	14.1 ± 0.1	3.18 ± 0.30	0.37	0.17
$2_{1,1}-2_{0,2}$	6.2878	2396	5	5.0	17.7	-9.7 ± 0.6	8.6 ± 1.5	1.40 ± 0.31	-0.05	-0.25
$1_{1,0}-1_{0,1}$	6.3157	2329	9	9.0	21.3	-14.5 ± 0.4	10.4 ± 1.0	2.43 ± 0.29	0.34	0.14
$1_{0,1}-1_{1,0}$	6.5149	2360	9	9.0	24.9	-9.9 ± 0.4	12.7 ± 1.7	2.08 ± 0.33	0.43	0.23
$7_{2,5}-7_{3,4}$	6.6462	3544	45	45.0	24.4	-10.7 ± 0.3	12.3 ± 0.9	1.84 ± 0.16	0.28	0.11
$4_{0,4}-4_{1,3}$	6.6674	2698	9	9.0	15.1	-8.3 ± 0.4	12.5 ± 1.1	1.75 ± 0.18	-0.01	-0.20
$9_{2,7}-9_{3,6}$	6.6895	4180	57	57.0	25.5	-9.6 ± 0.5	15.0 ± 1.7	1.20 ± 0.16	-0.06	-0.21
$7_{1,6}-7_{2,5}$	6.7261	3443	45	45.0	20.3	-11.9 ± 0.4	12.5 ± 1.0	1.63 ± 0.16	0.28	0.11
$3_{2,1}-3_{3,0}$	6.7334	2745	21	21.0	9.2	-13.3 ± 1.0	14.1 ± 2.9	1.45 ± 0.37	0.14	-0.05
$7_{3,4}-7_{4,3}$	6.7536	3701	45	45.0	18.0	-11.9 ± 0.4	12.4 ± 1.0	1.32 ± 0.14	0.07	-0.09
$5_{0,5}-5_{1,4}$	6.7653	2879	33	33.0	12.5	-12.2 ± 0.5	13.1 ± 1.2	1.71 ± 0.20	0.36	0.17
$4_{2,3}-4_{3,2}$	6.7693	2885	27	27.0	12.6	-12.1 ± 0.4	13.2 ± 1.0	1.44 ± 0.14	0.29	0.11
$5_{3,2}-5_{4,1}$	6.7987	3240	33	33.0	12.1	-11.2 ± 0.4	11.8 ± 0.9	1.50 ± 0.15	0.12	-0.05
$4_{3,2}-4_{4,1}$	6.8108	3064	27	27.0	7.7	-9.5 ± 0.7	13.5 ± 1.9	1.16 ± 0.21	-0.03	-0.21
$3_{0,3}-4_{1,4}$	6.8136	2621	27	21.0	17.1	-11.9 ± 0.4	13.5 ± 1.2	2.12 ± 0.23	0.49	0.30
$8_{1,7}-8_{2,6}$	6.8165	3735	17	17.0	18.4	-9.8 ± 0.5	10.9 ± 1.7	1.11 ± 0.21	-0.38	-0.54
$4_{1,4}-5_{0,5}$	6.8449	2764	33	27.0	16.0	-10.1 ± 0.5	11.6 ± 0.5	2.00 ± 0.20	0.47	0.29
$1_{1,0}-2_{2,1}$	6.8512	2507	15	9.0	26.0	-10.5 ± 0.3	13.0 ± 0.8	2.01 ± 0.16	0.41	0.22
$5_{1,5}-6_{0,6}$	6.9411	2938	13	11.0	16.0	-11.9 ± 0.6	9.0 ± 1.5	0.90 ± 0.19	-0.03	-0.21
$7_{0,7}-7_{1,6}$	6.9985	3323	45	45.0	10.0	-8.0 ± 0.4	13.8 ± 1.7	1.82 ± 0.27	0.11	-0.06
$6_{1,6}-7_{0,7}$	7.0362	3138	45	39.0	15.7	-10.4 ± 0.4	15.1 ± 1.3	2.00 ± 0.20	0.38	0.20
$2_{2,0}-3_{3,1}$	7.0934	2744	7	5.0	26.9	-10.6 ± 0.3	9.7 ± 0.9	1.07 ± 0.12	0.06	-0.13
$2_{2,1}-3_{3,0}$	7.0996	2745	21	15.0	26.7	-11.3 ± 0.3	15.8 ± 0.9	2.39 ± 0.18	0.53	0.34
$5_{1,4}-6_{2,5}$	7.1217	3110	39	33.0	11.1	-9.8 ± 0.2	9.8 ± 0.6	1.23 ± 0.10	0.21	0.03
$7_{0,7}-8_{1,8}$	7.1381	3364	51	45.0	15.1	-11.3 ± 0.4	13.1 ± 1.4	1.72 ± 0.22	0.27	0.10
$8_{1,8}-8_{2,7}$	7.1424	3590	51	51.0	9.2	-10.2 ± 0.6	9.5 ± 1.4	0.78 ± 0.15	-0.04	-0.20
$7_{1,6}-8_{2,7}$	7.2245	3590	51	45.0	11.1	-11.8 ± 0.2	10.0 ± 0.6	0.87 ± 0.07	0.01	-0.16
$8_{2,7}-9_{1,8}$	7.2272	3868	57	51.0	10.9	-12.1 ± 0.3	10.3 ± 0.7	0.85 ± 0.08	-0.16	-0.31
$3_{2,2}-4_{3,1}$	7.2371	2886	9	7.0	17.5	-11.4 ± 0.8	13.5 ± 2.1	1.01 ± 0.20	-0.07	-0.25
$9_{0,9}-9_{1,8}$	7.2431	3868	57	57.0	8.9	-11.6 ± 0.3	10.2 ± 1.0	0.72 ± 0.09	-0.19	-0.35
$3_{3,0}-4_{4,1}$	7.2937	3064	27	21.0	28.4	-11.6 ± 0.2	11.0 ± 0.5	1.54 ± 0.08	0.52	0.34
$4_{2,2}-5_{3,3}$	7.3018	3060	11	9.0	13.7	-13.4 ± 0.2	8.2 ± 0.6	1.05 ± 0.10	-0.18	-0.36
$9_{2,8}-10_{1,9}$	7.3255	4177	21	19.0	11.0	-14.5 ± 0.5	7.7 ± 1.2	0.49 ± 0.10	-0.80	-0.94
$9_{1,9}-10_{0,10}$	7.3323	3892	21	19.0	13.8	-10.7 ± 0.4	9.7 ± 1.1	0.69 ± 0.10	-0.50	-0.66
$9_{0,9}-10_{1,10}$	7.3337	3892	63	57.0	13.8	-9.5 ± 0.3	10.2 ± 0.3	1.22 ± 0.07	-0.03	-0.18
$4_{3,2}-5_{4,1}$	7.4294	3240	33	27.0	20.9	-10.1 ± 0.4	10.9 ± 1.0	1.70 ± 0.19	0.39	0.21
$5_{3,2}-6_{4,3}$	7.5509	3451	39	33.0	16.2	-11.5 ± 0.4	11.4 ± 1.0	1.25 ± 0.14	0.23	0.06
$5_{3,3}-6_{4,2}$	7.5739	3452	13	11.0	16.0	-7.0 ± 0.1	10.0 ± 1.7	0.85 ± 0.18	-0.25	-0.42
$5_{5,0}-6_{6,1}$	7.5956	3934	39	33.0	29.8	-9.2 ± 0.5	10.3 ± 1.6	0.99 ± 0.18	0.19	0.03
$6_{3,4}-7_{4,3}$	7.7350	3701	45	39.0	12.3	-7.0 ± 0.4	10.7 ± 1.0	0.88 ± 0.10	0.03	-0.14
$6_{5,2}-7_{6,1}$	7.7405	4181	45	39.0	24.2	-12.8 ± 0.3	13.0 ± 0.9	0.88 ± 0.08	0.01	-0.14

Note. E_l is the energy of the lower level of the transition, g_l and g_u are the statistical weights of the lower and upper levels respectively, A_{ul} is the Einstein A coefficient of the transition, v_{LSR} is the peak velocity of the line, FWHM is the full width at half maximum of the line, W is the equivalent width in units of Hz and τ_p is the peak optical depth of the transition. η_0 is the opacity in the lower level of the transition calculated for $\epsilon = 0.5$. Line data were taken from the HITRAN database (Gordon et al. 2017).

(This table is available in machine-readable form.)

observed range of maser velocities in each source. However, to explain the saturation of the lines at nonzero flux, a partial covering factor must be invoked in this case. Such a covering factor must vary with wavelength by up to a factor of 10 in order to account for column density variations observed in HCN and C_2H_2 at 7 and 13 μm. Furthermore, H_2O must cover the source less than HCN and C_2H_2 (Barr et al. 2022). It is difficult to understand the lack of 3 μm absorption lines in AFGL 2591, considering a foreground absorbing slab that absorbs at 7 and 13 μm.

5. A disk photosphere origin of the absorption lines explains in a natural way the presence of absorption lines that saturate at nonzero flux. A disk origin can also account for the column density variations of HCN and C_2H_2. However, the presence of absorption lines requires a decreasing temperature gradient with height in the disk, implying that the disk is not heated externally by the protostar. The absence of external illumination on the disk is consistent with the flashlight effect created by the outflow cavity and the observed thermal radio morphology. However, the midplane heating mechanism is unclear. Finally, the peak velocities of the absorption lines are offset from the systemic velocity of the sources, and the line widths are narrower than would be expected from a disk origin, requiring a specific disk structure, which is another major challenge to the model.

Based [in part] on observations made with the NASA/DLR Stratospheric Observatory for Infrared Astronomy (SOFIA). SOFIA is jointly operated by the Universities Space Research Association, Inc. (USRA), under NASA contract NNA17BF53C, and the Deutsches SOFIA Institut (DSI) under DLR contract 50 OK 0901 to the University of Stuttgart. The authors thank the anonymous referee for their very helpful and constructive input. A.G.G.M.T thanks the Spinoza premie of the NWO.

Appendix
Externally Heated Disks

Here we expand on the discussion on the formation of absorption lines in the foreground of an externally heated disk.

The model based upon foreground absorption of a disk externally heated by the protostar and radiating a continuum at mid-IR wavelength is expected to give emission rather than absorption lines. Specifically, consider a simplified model of two layers: a background layer responsible for the continuum emission and absorbed by a foreground molecular layer. The continuum intensity, I_c, is given by

$$I_c = B(T_d)(1 - \exp[-\tau_d]) \tag{A1}$$

with B the Planck function at the dust temperature T_d, and τ_d the dust emission optical depth. The line intensity is

$$I_L = B(T_d)(1 - \exp[-\tau_d])\exp[-\tau_L] + B(T_L)(1 - \exp[-\tau_L]) \tag{A2}$$

with T_L and τ_L the molecular excitation temperature and optical depth. The line-to-continuum ratio is then given by

$$\frac{I_L}{I_c} = \exp[-\tau_L] + \left(\frac{B(T_L)}{B(T_d)}\right) \times \left(\frac{1 - \exp[-\tau_L]}{1 - \exp[-\tau_d]}\right). \tag{A3}$$

We see that If $T_L \ll T_d$, then the second term is of no consequence and the line is in absorption ($I_L/I_c < 1$). If $T_L \gg T_d$, then the second term dominates and the line is (typically) in emission ($I_L/I_c > 1$) (depending slightly on τ_L and τ_d) as, if $\tau_d \ll 1$, then lines go into emission more easily).

The result of this is that the background emission layer will have to be warmer than the observed molecular excitation temperature ($\simeq$600 K) and be optically thickish, $\tau_d \gtrsim 1$. As the stellar radiation is deposited in an (absorption) optical depth of $\simeq$1, that implies that absorption and emission efficiency have to be equal.

Quantitatively, in radiative equilibrium, the dust temperature is given by

$$T_d = \left(\left(\frac{\overline{Q}_{\rm abs}}{\overline{Q}_{\rm em}}\right)\frac{L_{\rm star}}{(4\pi r^2)\sigma_{\rm sb}}\right)^{1/4} \tag{A4}$$

with $\overline{Q}_i$ the Planck averaged absorption and emission efficiencies of the dust, $L_{\rm star}$ the stellar luminosity (10^5 $L_\odot$), r the size of the disk (125 au), and $\sigma_{\rm SB}$ the Stefan–Boltzmann constant. The Planck averaged emission efficiency is given by $\overline{Q}_{\rm em} = 0.25(a/1\mu{\rm m})$ (Draine & Lee 1984) valid for $a < 4$ μm and 1 for larger sizes. We will set the absorption efficiency of the dust equal to 1. This results in $T_d = 1120$ (620) K for 0.1 (1) μm grains. We note that blackbodies would be 440 K for these conditions. Considering that the heating radiation will be deposited in a layer with a thickness of $\tau_{\rm abs} \simeq 1$, we have that the IR emission optical depth of this layer is $\tau_d = (\overline{Q}_{\rm em}/\overline{Q}_{\rm abs})\,\tau_{\rm abs} = 0.025$ (0.1 μm) and 0.25 (1 μm). The resulting line-to-continuum intensity is shown in Figure 21. In all cases, the lines are in emission as the continuum is not optically thick and/or the temperature is too low compared to the molecular excitation temperature. This is a very general result for externally heated disks.

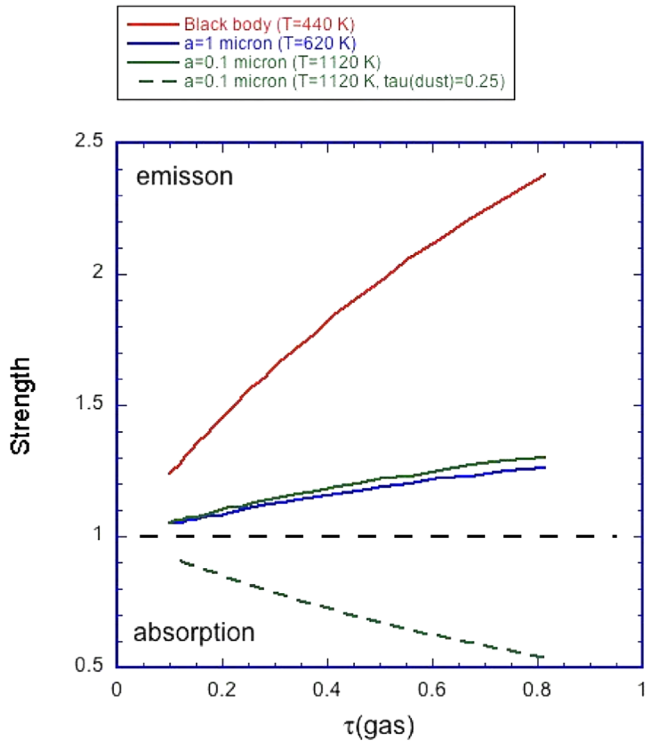

Figure 21. The expected line strengths relative to the continuum for a range of line optical depths are plotted for different dust properties. The horizontal black dashed line represents the boundary between the formation of absorption lines (<1) and emission lines (>1). The solid red curve represents the line strengths for blackbody emission, and the blue and green curves the line strengths for 1 and 0.1 μm grains, respectively. The blackbody grains produce emission lines as the foreground gas is observed to be warmer than the expected dust temperature. The 1 and 0.1 μm grains are warmer than the foreground gas but the continuum emitting layer is optically thin and hence the foreground gas would produce excess emission in the lines. The dashed green curve represents a model where the mid-IR optical depth of the disk has been arbitrarily increased by an order of magnitude. In this model, the high dust temperature coupled with this high optical depth results in absorption lines.

ORCID iDs

Andrew G. Barr https://orcid.org/0000-0003-4909-2770
Adwin Boogert https://orcid.org/0000-0001-9344-0096
Jialu Li https://orcid.org/0000-0003-0665-6505
Curtis N. DeWitt https://orcid.org/0000-0002-6528-3836
Edward Montiel https://orcid.org/0000-0003-2553-4474
Matthew J. Richter https://orcid.org/0000-0002-8594-2122
Nick Indriolo https://orcid.org/0000-0001-8533-6440
Yvonne Pendleton https://orcid.org/0000-0001-8102-2903
Jean Chiar https://orcid.org/0000-0003-2029-1549
Alexander G. G. M. Tielens https://orcid.org/0000-0003-0306-0028

References

Adams, S. C., Adámkovics, M., Carr, J. S., et al. 2019, ApJ, 871, 173
Agúndez, M., Roueff, E., LePetit, F., & Le Bourlot, J. 2018, A&A, 616, A19
Barentine, J., & Lacy, J. 2012, ApJ, 757, 111
Barr, A. G., Boogert, A., DeWitt, C. N., Montiel, E., et al. 2018, ApJL, 868, L2
Barr, A. G., Boogert, A., DeWitt, C. N., Montiel, E., et al. 2020, ApJ, 900, 104
Barr, A. G., Boogert, A., Li, J., Lee, A., & Tielens, A. G. G. M. 2020, A&A, in press
Beuther, H., Churchwell, E. B., McKee, C. F., & Tan, C. J. 2007, in Protostars and Planets V, ed. B. Reipurth, D. Jewitt, & K. Keil, Vol. 951 (Tucson, AZ: Univ. Arizona Press)
Blake, G. A., & Boogert, A. C. A. 2004, ApJ, 606, L73
Boley, P. A., Linz, H., van Boekel, R., et al. 2013, A&A, 558, A24
Boonman, A. M. S., Doty, S. D., van Dishoeck, E. F., et al. 2003, A&A, 406, 937
Boonman, A. M. S., & van Dishoeck, E. F. 2003, A&A, 403, 1003
Burkhardt, A. M., Dollhopf, N. M., Corby, J. F., et al. 2016, ApJ, 827, 21
Caratti o Garatti, A., Stecklum, B., Garcia Lopez, R., et al. 2017, NatPh, 13, 276
Carr, J. S., & Najita, J. R. 2008, Sci, 319, 1504
Cernicharo, J., & Crovisier, J. 2005, SSRv, 119, 29
Cernicharo, J., Lim, T., Cox, P., et al. 1997, A&A, 323, L25
Charnley, S. B., Tielens, A. G. G. M., & Millar, T. J. 1992, ApJL, 399, L71
Clarke, M., Vacca, W. D., & Shuping, R. Y. 2015, ASP Conf. Ser. 495, Astronomical Data Analysis Software and Systems XXIV (ADASS XXIV), ed. A. R. Taylor & E. Taylor, (San Francisco, CA: ASP), 355
Cuzzi, J. N., Hogan, R. C., & Shariff, K. 2008, ApJ, 687, 1432
D'Alessio, P., Cantó, J., Calvet, N., & Lizano, S. 1998, ApJ, 500, 411
de Wit, W. J., Hoare, M. G., Oudmaijer, R. D., et al. 2011, A&A, 526, L5
Doty, S. D., van Dishoeck, E. F., van der Tak, F. F. S., & Boonman, A. M. S. 2002, A&A, 389, 446
Draine, B. T., & Lee, H. M. 1984, ApJ, 285, 89
Dullemond, C. P., & Dominik, C. 2008, A&A, 487, 205
Dullemond, C. P., Hollenbach, D., Kamp, I., & D'Alessio, P. 2007, in Protostars and Planets V, Vol. 555 ed. B. Reipurth, D. Jewitt, & K. Keil (Tucson, AZ: Univ. Arizona Press)
Egan, M. P., Shipman, R. F., Price, S. D., et al. 1998, ApJ, 494, L199
Evans, N. J., Lacy, J. H., & Carr, J. S. 1991, ApJ, 383, 674
Faure, A., & Josselin, E. 2008, A&A, 492, 257
Frost, A. J., Oudmaijer, R. D., de Wit, W. J., & Lumsden, S. L. 2021, A&A, 648, A62
Furuya, R. S., Cesaroni, R., Takahashi, S., et al. 2005, ApJ, 624, 827
Gieser, C., Semenov, D., Beuther, H., et al. 2019, A&A, 631, A142
Goicoechea, J. R., Chavarría, L., Cernicharo, J., et al. 2015, ApJ, 799, 102
González-Alfonso, E., Cernicharo, J., van Dishoeck, E. F., et al. 1998, ApJ, 502, L169
Gordon, I. E., Rothman, L. S., Hill, C., et al. 2017, JQSRT, 203, 3
Goto, M., Geballe, T. R., Harju, J., et al. 2019, A&A, 632, A29
Hollenbach, D., Elitzur, M., & McKee, C. 2013, ApJ, 773, 70
Hosokawa, T., Yorke, H. W., & Omukai, K. 2010, ApJ, 721, 478
Ilee, J. D., Cyganowski, C. J., Brogan, C. L., et al. 2018, ApJ, 869, L24
Indriolo, N., Neufeld, D. A., Barr, A. G., et al. 2020, ApJ, 894, 107
Indriolo, N., Neufeld, D. A., DeWitt, C. N., Richter, M. J., et al. 2015, ApJL, 802, L14
Jiménez-Serra, I., Zhang, Q., Viti, S., Martín-Pintado, J., & De-Wit, W.-J. 2012, ApJ, 753, 34
Johnston, K. G., Hoare, M. G., Beuther, H., Linz, H., et al. 2020, ApJ, 896, 35
Kaufman, M. J., & Neufeld, D. A. 1996, ApJ, 456, 250
Kaźmierczak-Barthel, M., van der Tak, F. F. S., Helmich, F. P., et al. 2014, A&A, 567, A53
Knez, C., Lacy, J. H., Evans, N. J., van Dishoeck, E. F., & Richter, M. J. 2009, ApJ, 696, 471
Kristensen, L. E., van Dishoeck, E. F., Mottram, J. C., Karska, A., et al. 2017, A&A, 605, A93
Kuiper, R., Klahr, H., Beuther, H., & Henning, T. 2010, ApJ, 722, 1556
Kuiper, R., Klahr, H., Beuther, H., & Henning, T. 2011, ApJ, 732, 20
Kuiper, R., Turner, N. J., & Yorke, H. W. 2016, ApJ, 832, 40
Lacy, J. H., Richter, M. J., Greathouse, T., et al. 2003, Proc. SPIE, 4841, 1572
Maud, L. T., Cesaroni, R., Kumar, M. S. N., Rivilla, V. M., et al. 2019, A&A, 627, L6
Maud, L. T., Cesaroni, R., Kumar, M. S. N., van der Tak, F. F. S., et al. 2018, A&A, 620, A31
McKee, C. F., & Tan, J. C. 2003, ApJ, 585, 850
Melnick, G. J., Tolls, V., Neufeld, D. A., et al. 2010, A&A, 521, L27
Menten, K. M., & van der Tak, F. F. S. 2004, A&A, 414, 289
Mihalas, D. 1978, Stellar Atmospheres (2nd ed.; San Francisco, CA: Freeman), 211
Mitchell, G. F., Maillard, J., & Allen, M. 1990, ApJ, 363, 554
Monnier, J. D., Tuthill, P. G., Ireland, M., et al. 2009, ApJ, 700, 491
Moreno, R., Lellouch, E., Luisa, L. M., et al. 2012, Icar, 221, 753
Nakano, T. 1989, ApJ, 345, 464
Neufeld, D. A., González-Alfonso, E., Melnick, G. J., et al. 2011, ApJL, 727, L28
Ormel, C. W., Min, M., Tielens, A. G. G. M., et al. 2011, A&A, 532, A43
Pontoppidan, K. M., Salyk, C., Banzatti, A., Blake, G. A., et al. 2019, ApJ, 874, 92
Preibisch, T., Balega, Y. Y., Schertl, D., & Weigelt, G. 2003, A&A, 412, 735

Rangwala, N., Colgan, S. W. J., Le Gal, R., Acharyya, K., et al. 2018, ApJ, 856, 9
Richter, M., Dewitt, C. N., McKelvey, M., et al. 2018, JAI, 7, 1840013
Rothman, L. S., Gordon, I. E., Babikov, Y., et al. 2013, JQRST, 130, 4
Salyk, C., Lacy, J., Richter, M., et al. 2019, ApJ, 874, 24
Salyk, C., Pontoppidan, K. M., Blake, G. A., et al. 2011, ApJ, 731, 130
Sanna, A., Reid, M. J., Carrasco-González, C., et al. 2012, ApJ, 745, 191
Suri, S., Beuther, H., Gieser, C., Ahmadi, A., et al. 2021, A&A, 655, A84
Tafalla, M., Santiago-García, J., Hacar, A., et al. 2010, A&A, 522, A91
Tan, J. C. 2008, in ASP Conf. Ser. 387, Massive Star Formation: Observations Confront Theory, ed. H. Beuther, H. Linz, & Th. Henning (San Francisco, CA: ASP), 346
Tan, J. C., & McKee, C. F. 2003, in IAU Symp. 221, Star Formation at High Angular Resolution, ed. J. Burton, R. Jayawardhana, & T. Bourke (Cambridge: Cambridge Univ. Press), 221
Tanaka, K. E. E., Tan, J. C., Staff, J. E., & Zhang, Y. 2017, ApJ, 849, 133
Tanaka, K. E. I., Tan, J. C., & Zhang, Y. 2016, ApJ, 8181, 52
Tielens, A. G. G. M. 2021, Molecular Astrophysics (1st edn.; Cambridge: Cambridge Univ. Press), 132
Torrelles, J. M., Trinidad, M. A., Curiel, S., et al. 2014, MNRAS, 437, 3803
Trinidad, M. A., Curiel, S., Cantó, J., et al. 2003, ApJ, 589, 386
van der Tak, F. F. S., Chavarría, L., Herpin, F., et al. 2013, A&A, 554, A83
van der Tak, F. F. S., van Dishoeck, E. F., Evans, N. J., & Bakker, E. J. 1999, ApJ, 522, 991
van Dishoeck, E. F. 1998, FaDi, 109, 31
van Dishoeck, E. F., & Helmich, F. P. 1996, A&A, 315, L177
van Dishoeck, E. F., Herbst, E., & Neufeld, D. 2013, ChRv, 113, 9043
van Dishoeck, E. F., Kristensen, L. E., Mottram, J. C., et al. 2021, A&A, 648, A24
Walsh, C., Nomura, H., & van Dishoeck, E. F. 2015, A&A, 582, A88
Wang, K. S., van der Tak, F. F. S., & Hogerheijde, M. R. 2012, A&A, 543, A22
Wilner, D. J., De Pree, C. G., Welch, W. J., et al. 2001, ApJL, 550, L81
Wilson, T. L., & Rood, R. T. 1994, ARA&A, 32, 191
Wright, C. M., van Dishoeck, E. F., Black, J. H., et al. 2000, A&A, 358, 689
Yorke, H. W., & Bodenheimer, P. 1999, ApJ, 525, 330
Young, E. T., Becklin, E. E., Marcum, P. M., et al. 2012, ApJL, 749, L17
Zinnecker, H., & Yorke, H. W. 2007, ARA&A, 45, 481